Per Håkon Pedersen Finne

Pursuing Sustainable Cathodes with High Rate Capability

Master's thesis in Materials Science and Engineering
Supervisor: Espen Sandnes
Co-supervisor: Odne Stokke Burheim and Silje Nornes Bryntesen
June 2022

Master's thesis

NTNU
Norwegian University of Science and Technology
Faculty of Natural Sciences
Department of Materials Science and Engineering

NTNU
Kunnskap for en bedre verden

Per Håkon Pedersen Finne

Pursuing Sustainable Cathodes with High Rate Capability

Master’s thesis in Materials Science and Engineering
Supervisor: Espen Sandnes
Co-supervisor: Odne Stokke Burheim and Silje Nornes Bryntesen
June 2022

Norwegian University of Science and Technology
Faculty of Natural Sciences
Department of Materials Science and Engineering

NTNU
Norwegian University of
Science and Technology

Preface

This thesis has been completed as a partial fulfillment of the requirements for the degree Master of Science in Materials Science and Engineering at NTNU. It has been a project under the Department of Materials Science and Engineering during the spring semester of 2022. All experiments in this thesis are developed and performed by the author.

I would like express my sincerest gratitude to all contributors at the Department of Materials Science and Engineering and the Department of Energy and Process Engineering. I would like to thank my supervisors Odne Stokke Burheim and Espen Sandnes for their guidance. I am truly grateful of their expertise and and the time they devoted to me throughout the project.

I am also utterly grateful for all the help received from Ph.D. Candidate Silje Nornes Bryntesen. Her incredible knowledge of the theoretical background of Li-ion batteries and lab experience have been invaluable. In addition, her enthusiasm and positive energy have been contagious, sparking my passion for the project.

On a personal level, I would like to thank my friends and colleagues for supporting me and making my time as a student truly memorable. A special thanks is also devoted to my family, who have been especially supportive in the final stages of this thesis, and particularly to my grandpa, who has been my inspiration through five years of studying.

Per Håkon Pedersen Finne
11th of June 2022

Abstract

Lithium-ion batteries (LiBs) are expected to be one of the main energy storage systems of the future, as it is able to store and produce energy without producing greenhouse gases. The overall CO_2 footprint of a LiB is however to a large degree determined by its energy intensive manufacturing process. A large part of the energy is used during electrode drying, where the toxic organic solvent N-Methyl-2-pyrrolidone (NMP) needs to be fully recovered to avoid polluting the environment. NMP is required to dissolve the state-of-the-art polyvinylidene fluoride (PVDF) binder used in commercial cathodes. This work has focused on replacing the NMP and PVDF with water and lignin, respectively, with the goal to reduce energy consumption in LiB manufacturing. Another important task has been to improve the performance of the cathode in LiBs during operation, where the approach has been to structure the cathodes mechanically.

Cathodes with lithium-nickel-manganese-cobalt-oxide (NMC111) as active material were produced with an aqueous manufacturing route using lignin as binder. To enhance the wetting properties and rate performance of the cathodes, two different structuring tools were used to make five different structures. Three of these were line structures, ceramic blade perforations (Perf), small lines (SL) and large lines (LL), while two were hole structures, small pillars (SP) and large pillars (LP). The structures were investigated and their dimensions determined using Scanning Electron Microscopy (SEM). Their effect on diffusion paths in the cathodes were examined using Potential Step Chronoamperometry (PSCA) and a model for diffusion in planar sheets. The unstructured and structured cathodes were tested and compared electrochemically in coin cells with Li-metal anodes, using galvanostatic cycling and Electrochemical Impedance Spectroscopy (EIS). Chemical degradation as a result of cycling was investigated using Energy Dispersive X-ray Spectroscopy (EDS). Finally, the lignin cathodes were compared to cathodes with PVDF binder.

The unstructured lignin cathodes performed adequately, with a close correlation between performance and thickness. Cathodes with low thickness (31 μm) were found to have close to 60 mAh/g capacity at 5 C, which was reduced quickly with increasing thicknesses. Ohmic and SEI layer resistances were found to increase significantly with thickness, indicating an electrolyte degradation during cycling. The cathodes were found to otherwise be chemically stable, with only some CEI layer formation taking place and no transition metal leaching during cycling. Structuring of the cathodes improved their properties, both rate capability and wetting. Perf, SL, LL and SP all had higher capacity retention up to 5 C than unstructured cathodes, for thicknesses of $\approx$ 100 μm.

LP, however, was wound to impair the performance of the cathode, likely due to compressing too much of the active material, reducing the porosity and hindering ionic transport. The Perf, SL, LL and SP structures resulted in lower ohmic and SEI layer resistances compared to unstructured cathodes of similar thickness, indicating better cathode wetting and low electrolyte degradation. The structures were found to contain their dimensions during cycling to a large extent, with only limited degradation taking place. The Perf line structure yielded the best rate performance for cathodes with $\approx$ 100 μm thickness, where a capacity of about 60 mAh/g was found for 2 C and 20 mAh/g for 5 C, which was over twice as high as the unstructured cathode. This cathode was compared to line structured cathodes with PVDF binder of twice the spacing between the structures, in the thickness range 50-150 μm. The PVDF cathodes were found to perform equally or better than the cathodes with lignin for all thicknesses, with the closest performance seen for the thickest cathodes. At $\approx$ 150 μm thickness, their capacities were found to be $\approx$ 20 mAh/g for 2.5 C. Therefore, it is suggested that PVDF cathodes out-perform lignin cathodes at low thicknesses, where the ionic transport appears to be adequate regardless of the structures, but with the use of structuring, their performance becomes equal for thicker cathodes. The use of lignin as binder in cathodes with NMC111 seems promising, but requires further development of structuring techniques to reach the performance of PVDF.

The diffusion model was found to be able to model the behaviour of cathodes, as it managed to find theoretical time constants that were close to the experimental values, independent of cathode thickness. The calculated effective diffusion coefficients of the unstructured and structured cathodes were found to be close in value, in the range 1.34 to $3.73 \cdot 10^{-9}$ m^2/s, indicating diffusion in the electrolyte. By calculating the diffusion length from the effective diffusion coefficient and experimental time constant, it was found to be close to the size of the diffuse layer at particle surfaces (10.1 to 33.9 μm). Thus, the PSCA measurements were found to measure diffusion through the diffuse layer, and the technique could not be used to detect changes in diffusion paths as a result of cathode structuring.

Sammendrag

Litium-ionebatterier (LiBer) er forventet å bli en av fremtidens viktigste energilagringskilder, da de gir mulighet for å lagre og bruke energi uten å produsere drivhusgasser. CO_2-fotavtrykket til LiBer er derimot i stor grad bestemt av fremstillingsprosessen, som krever store mengder energi. En betydelig andel av denne energien brukes for å tørke elektrodene, der det giftige organiske løsemiddelet N-Metyl-2-pyrrolidon (NMP) må samles opp etter bruk for å unngå utslipp til miljøet. NMP må brukes for å løse det kommersielt brukte bindemiddelet polyvinyldifluorid (PVDF). Denne oppgaven har fokusert på å bytte ut NMP og PVDF med vann og lignin, henholdsvis, med formål om å redusere energiforbruket i LiB produksjon. En annen viktig oppgave har vært å forbedre ytelsen til katodene i LiBer under bruk, hvor fremgangsmåten her har vært å strukturere katodene mekanisk.

Katoder med litium-nikkel-mangan-cobolt-oksid (NMC111) som aktivt materiale ble produsert ved hjelp av en vannbasert produksjonsrute med lignin som bindemiddel. For å forbedre fukte-egenskapene og utladningskapasiteten til katodene ble to ulike struktureringsmetoder brukt, og fem ulike strukturer. Tre av disse var linjestrukturer, keramisk blad-perforering (Perf), små linjer (SL) og store linjer (LL), mens to var hullstrukturer, små pillarer (SP) og store pillarer (LP). Strukturene ble undersøkt og dimensjonene målt ved hjep av skanning elektronmikroskop (SEM). Effekten av strukturene på diffusjonslengdene i katodene ble undersøkt med potensialsteg kronoamperometri (PSCA) og en modell for diffusjon mellom plane overflater. De ustrukturerte og strukturerte katodene ble testet og sammenliknet elektrokjemisk ved galvanostatisk inn- og utladning, i knappeceller med Li-metal som anoder. I tillegg ble motstanden målt ved å bruke elektrokjemisk impedans spektroskopi (EIS). Kjemisk dekomponering som et resultat av inn- og utladning ble undersøkt med energidispersiv røntgendetektor (EDS). Til slutt ble katodene sammenliknet med katoder med PVDF som bindemiddel.

De ustrukturerte lignin katodene presterte tilstrekkelig, med en nær sammenheng mellom kapasitet og tykkelse. Katodene med lav tykkelse (31 μm) ble målt til å ha en kapasitet rundt 60 mAh/g ved 5 C, som raskt ble redusert for katodene med høyere tykkelse. Den ohmske og SEI-lag motstanden ble målt til å øke betydelig med tykkelse, som indikerer en dekomponering av elektrolytten under testing. Katodene var ellers kjemisk stabile, med en begrenset formasjon av CEI-lag og ingen lekking av overgangsmetaller fra det aktive materialet under galvanostatisk inn- og utladning. Strukturering av katodene forbedret egenskapene, både høyhastighetsutladningen og fuktingen.

Perf, SL, LL og SP hadde alle høyere kapasitet opp til 5 C enn de ustrukturerte katodene for tykkelser rundt 100 μm. LP viste seg å hemme egenskapene til katoden, sannsynligvis som følge av at for store mengder av det aktive materialet har blitt sammenpresset, som har ført til redusert porøsitet og lavere ionisk ledningsevne. Perf, SL, LL og SP strukturene ga lavere ohmsk og SEI-lag motstand, sammenliknet med de ustrukturerte katodene med lik tykkelse, som tyder på økt fukting og lite dekomponering av elektrolytten. Strukturene endres i liten grad under testing. Linjestrukturen Perf ga den beste kapasiteten for samtlige strømmer for katodene med $\approx$ 100 μm tykkelse, hvor en kapasitet på 60 mAh/g ble målt ved 2 C og 20 mAh/g ble målt ved 5 C, som var dobbelt så høyt som den ustrukturerte katoden. Denne katodestrukturen ble sammenliknet med linjestrukturerte PVDF katoder med dobbelt så stor avstand mellom linjene, for tykkelser mellom 50 og 150 μm. PVDF katodene presterte like bra eller bedre enn samtlige av katodene med lignin, hvor de likeste kapasitene ble målt for katodene på $\approx$ 150 μm ($\approx$ 20 mAh/g ved 2.5 C). Resultatene indikerer dermed at PVDF katodene har bedre egenskaper for de laveste tykkelsene, hvor ionetransport ikke er en begrensende faktor, men ved å strukturere, kan ytelsen deres bli lik for de tykke katodene. Bruk av lignin i katoder med NMC111 virker dermed lovende, men krever videreutvikling av struktureringsteknikker for å oppnå samme ytelse som PVDF.

Diffusjonsmodellen klarte å modellere strømresponsen fra PSCA, hvor den beregnet teoretiske tidskonstanter som var like de eksperimentelle verdiene, uavhengig av katodetykkelse. De beregnede effektive diffusjonskoeffisientene til de ustrukturerte og strukturerte katodene ble funnet til å være svært like, fra 1.34 til $3.73 \cdot 10^{-9}$ m^2/s, som indikerer at det er diffusjon i elektrolytten som undersøkes. Ved å finne diffusjonslengden fra den effektive diffusjonskoeffisienten og den eksperimentelle tidskonstanten, ble det fastslått at diffusjon fant sted i diffusjonslaget på NMC partiklene, da verdiene var mellom 10.1 og 33.9 μm. Dermed måler PSCA diffusjon gjennom diffusjonslaget på partikkeloverflatene, og teknikken kan ikke brukes til å undersøke endringer i diffusjon som følge av strukturering av katodeoverflaten.

List of Figures

2.1 The structures of the three different classes of cathode oxides, layered, spinel and polyanion[10]. . . . 4

2.2 Illustrations of the three most common electrode structures, from the left: grid structure, line structure and hole structure[5]. . . . 10

2.3 Schematic illustration of ionic conduction in a) an unstructured and b) a structured cathode. . . . 11

2.4 Schematic illustration of the theoretical maximum distance between indentations needed to improve ionic conduction to all NMC particles. 12

2.5 Shows the effect on Li-ion diffusion by the depth of indentations and spacing between them[19]. . . . 12

2.6 Illustration of the increased density of electrode material compressed by mechanical structuring. . . . 13

2.7 Shows two ways of presenting the results of galvanostatic cycling: a) Charge-discharge curve of a battery with a NMC cathode, with C-rates from C/20 to 1 C[32]. b) Rate-performance plot of an NMC cathode, which shows how the capacity fades with increasing C-rates[4]. . . . 14

2.8 Nyquist diagram with its corresponding equivalent circuit. a) Overview of the electrochemical processes which are dominating at the different frequency ranges. b) Equivalent circuit for the Nyquist diagram in (a)[33]. 15

2.9 An equivalent circuit which models the behavior of a realistic cathode and anode, with constant phase elements (Q) and resistances (R)[35]. 16

3.1 Schematic of the different steps in the production of a lithium-ion coin cell, from precursors to finished cell. . . . 20

3.2 Ceramic blades used to create line structures with 200 μm spacing in cathodes. . . . 21

3.3 Silica wafer used to create four different structures in cathodes. . . . 22

3.4 Schematic illustration of the ordering and configuration of the CR2032 coin cell[42]. . . . 23

4.1 Two cathodes perforated with the ceramic blades. a) Overview of several indentations made. b) Measurements of two indentations and the channel between them. . . . 27

4.2 Shows the cross-section of two perforated cathodes. a) 60 μm thick cathode with $\approx$ 30 μm indentations. b) 75 μm thick cathode with $\approx$ 35 μm indentations. . . . 27

4.3 Post mortem analysis of blade perforated (perf) cathodes after 54 cycles. a) Surface view of structures that have not changed by cycling. b) Surface view of damaged structures 28
4.4 Small line (SL) structure in a pristine, uncycled cathode. a) At 200 magnification and b) at 1k magnification. 29
4.5 Cross-section of two cathodes with small line (SL) structures, the depth of the indentations was found to be one third of the total thickness. . . 29
4.6 Post mortem analysis of a cathode with small line (SL) structures after 54 cycles. 30
4.7 Two pristine cathodes with LL structures. a) Surface view and b) Cross-section. 31
4.8 Post mortem analysis of large line (LL) structured cathodes after 54 cycles. The structures seem unharmed, but the figure shows chromium impurities in the indentations. 32
4.9 Shows pristine cathodes with small pillar (SP) structures from a) Surface and b) Cross-sectional view. 33
4.10 Post mortem analysis of a cathode with small pillars (SP) after 54 cycles. 33
4.11 Shows two pristine cathodes structured with large pillars (LP). a) Surface view and (b) Cross-section view. 34
4.12 Post mortem analysis of a large pillar (LP) structured cathode, showing twice the amount of structures as wanted. 35
4.13 Post mortem EDS mapping of two cathodes, a) with LL structures and b) with LP structures. 38
4.14 Potential vs. specific capacity plot for two cathodes with thickness and porosity: a) 28 μm and 44.4 %, b) 100 μm and 41.3 %. 41
4.15 Rate performance of four unstructured cathodes, Un-LT2, Un-MT1, Un-HT2 and Un-UT1, which thicknesses of 31, 78, 155 and 209 μm, respectively. 42
4.16 Rate performance of the line structured cathodes, each with 3-4 different thicknesses. a) Blade perforated (Perf), b) Small lines (SL) and c) Large lines (LL). 43
4.17 Rate performance of the hole structured cathodes with thicknesses from 100 to 200 μm. a) Small pillar (SP) and b) Large pillar LP. 45
4.18 Average rate performance of the medium thickness a) unstructured (Un) and b) blade perforated (Perf) cathodes. 46
4.19 Average rate performance of the medium thickness a) small lines (SL) and b) large lines (LL) cathodes. 46
4.20 Average rate performance of the medium thickness a) small pillar (SP) and b) large pillar (LP) cathodes. 47
4.21 Nyquist diagram of two unstructured cathodes of low (Un-LT) and high (Un-HT) thickness, with experimental values and curves fitted to the equivalent circuit seen in Figure 2.9. 48

4.22 Nyquist diagram of a high thickness large line cathode (LL-HT), with experimental values and curves fitted to the equivalent circuit seen in Figure 2.9 after each cycling program, Formation (Form), Soaking (Soak) and Rate-testing (Rate). 49
4.23 Nyquist diagram and the fitted curves of five structured cathodes with medium thickness after rate testing. a) Perf, SL and LL, b) SP and LP. . 50
4.24 Current vs. time graphs from potential step chronoamperometry measurements. Shows the current response of a) NMC/Li-metal coin cell (LL-LT1), b) NMC/NMC coin cell and c) Li-metal/Li-metal coin cell. . . 53
4.25 a) Shows the theoretical and experimental charge vs. time curve resulting from the diffusion model of and a PSCA measurement of an unstructured cathode. b) Shows a time constant vs. thickness plot of unstructured cathodes. 54
4.26 Shows the experimental and theoretical time constants of blade Perf, SL, LL and SP structured cathodes with corresponding thicknesses, divided into two categories based on porosity. a) Over 45 % and b) Below 45 % porosity. 54
4.27 Average rate performance plots of low thickness line structured cathodes with a) lignin (Perf-LT) and b) PVDF binder (VLL-LT). 57
4.28 Average rate performance plots of medium thickness line structured cathodes with a) lignin (Perf-MT) and b) PVDF (VLL-MT) binder. . . . 57
4.29 Average rate performance plots of high thickness line structured cathodes with a) lignin (Perf-HT) and b) PVDF binder (VLL-HT). 58

A.1 Measurements of the dimensions for two of the blade perforated (Perf) cathodes. a) Surface view and b) Cross-section. VII
A.2 Measurements of the dimensions for two of the small line (SL) cathodes. a) Surface view and b) Cross-section. VIII
A.3 Measurements of the dimensions for two of the large line (LL) cathodes. a) Surface view and b) Cross-section. VIII
A.4 Measurements of the dimensions of two of the small pillar (SP) cathodes. a) Surface view and b) Cross-section. IX
A.5 SEM images of a cathode with large pillar (LP) structures. a) Cross section with measurements of the depth of the structure. b) Example of the effect poor structuring has on the cathode film. IX

List of Tables

2.1 The properties of an ideal electrolyte[12]. 6
2.2 Diffusion coefficients of the Li-containing salt $LiPF_6$ and its ions, in the liquid electrolyte (D_{liq}) and in the solid NMC particles (D_{SS})[39–41]. . . 18

3.1 The four precursors used to make the cathode slurry. 19
3.2 The apparatuses used in the manufacturing of NMC cathodes and coin-cell assembly. 19
3.3 The parts of the battery pack. 22
3.4 The three programs the cells were subsequently cycled through, Formation (Form), Soaking (Soak) and Rate-testing (Rate), ending at a total of 54 cycles. EIS measurements was measured after each program. . . 24

4.1 The different structures which were made in the cathodes with the expected dimensions from the structuring tool. 25
4.2 Measured dimensions of the structured cathodes in pristine condition (N) and post mortem (PM). 26
4.3 Composition of two unstructured cathodes, pristine and post mortem. Shows the Co, Ni, Mn and P content. 36
4.4 Chemical analysis post mortem of the structured cathodes, showing the composition of Co, Ni, Mn and P. 37
4.5 Explanations of the four thicknesses the cathodes have been grouped into. 39
4.6 Overview of the tested cathodes, with the number of cathodes in each group, and the ranges in thickness, porosity and intial specific capacity. 40
4.7 Fitting parameters from the equivalent circuit seen in Figure 2.9 for two unstructured cathodes of low (Un-LT) and high (Un-HT) thickness. . . 49
4.8 Fitting parameters of the Nyquist diagram of LL-HT, seen in Figure 4.22, after each cycling program. 50
4.9 Fitting parameters from the equivalent circuit seen in Figure 2.9 for five structured cathodes with varying thicknesses. 51
4.10 The experimentally determined time constant (τ_{exp}), modelled effective diffusion coefficient (D_{eff}) and calculated diffusion length (l) of cathodes with medium thickness. 55
4.11 Overview of the cathodes with PVDF, with the number of cathodes in each group and the range in thickness, porosity and initial specific capacity. 56

Contents

Preface . . . iii
Abstract . . . iv
Sammendrag . . . vi
List of Figures . . . viii
List of Tables . . . xi
Contents . . . xiii
1 Background . . . 1
  1.1 Motivation . . . 1
  1.2 Aim of work . . . 2
2 Introduction . . . 3
  2.1 Lithium-ion battery components . . . 3
    2.1.1 Electrodes . . . 3
    2.1.2 Electrolyte . . . 5
    2.1.3 Separator . . . 6
    2.1.4 Current collector . . . 7
  2.2 Electrode design . . . 7
  2.3 Electrode manufacturing . . . 8
    2.3.1 Wet-slurry processing . . . 9
    2.3.2 Structuring . . . 10
  2.4 Characterization techniques . . . 13
    2.4.1 Scanning Electron Microscopy . . . 13
    2.4.2 Galvanostatic cycling . . . 14
    2.4.3 Electrochemical Impedance Spectroscopy . . . 15
    2.4.4 Potential Step Chronoamperometry . . . 16
  2.5 Modelling diffusion behavior . . . 17
3 Experimental Work . . . 19
  3.1 Chemicals and apparatus . . . 19
  3.2 Battery production . . . 20
    3.2.1 Cathode manufacturing . . . 20
    3.2.2 Perforation . . . 20
    3.2.3 Cell assembly . . . 22
  3.3 Characterization Techniques . . . 23
    3.3.1 Scanning Electron Microscopy . . . 23
    3.3.2 Galvanostatic cycling . . . 23
    3.3.3 Electrochemical Impedance Spectroscopy . . . 24
    3.3.4 Potential Step Chronoamperometry . . . 24

4 Results and Discussion **25**
4.1 Structural analysis of structured lignin binder cathodes 25
4.1.1 Perforated with ceramic blades 26
4.1.2 Small line structures 28
4.1.3 Large line structures 30
4.1.4 Small pillar structures 32
4.1.5 Large pillar structures 33
4.2 Chemical analysis of lignin binder cathodes 36
4.2.1 Transition metal leaching 36
4.2.2 Cathode electrolyte interphase formation 37
4.2.3 Contamination from structuring 37
4.3 Electrochemical analysis of cathodes with lignin binder 39
4.3.1 Cycling performance 40
4.3.2 Rate performance 41
4.3.3 Comparison of the rate performance of the structures 45
4.3.4 EIS analysis 47
4.3.5 Diffusion behaviour 52
4.4 Comparison between cathodes with polyvinylidene fluoride and lignin binder 56
5 Conclusion **59**
6 Further Work **61**
Bibliography . . . . **I**
A Appendices . . . . **VII**
A.1 SEM structuring dimensions VII

Chapter 1

Background

1.1 Motivation

Our renewable energy supply is to a large extent discontinuous and dependent on external factors, therefore intermediate power storage is required to meet the continuous need for energy. Rechargeable batteries are the main tool for meeting the demands of both the present and the future, while offering the opportunity to reduce CO_2 emissions in multiple sectors. Batteries can be engineered to fit most applications, and therefore makes it possible to become more sustainable, without compromising on performance. Hence, rechargeable batteries are one of our main ways of fighting climate change, by making the shift from a fossil-fueled to a green society possible [1, 2].

The use of batteries makes it possible to store and use energy without producing CO_2, but the commercial manufacturing process is highly energy intensive. A large fraction of the energy consumption is used to dry-off and recover the toxic organic compound n-methyl-2-pyrrolidone (NMP) which is required to dissolve polyvinylidene fluoride (PVDF), the material binding the electrode together. By substituting the organic solvent with water and finding an alternative to PVDF which gives the battery the same properties, vast amounts of energy can be saved in the drying process and yield a more sustainable manufacturing process[3].

To further improve the properties of batteries and to avoid the compromise between energy density and power density, electrode structuring is a technique that has shown positive results. Structuring has to a large extent been done using lasers to create indentations in the electrode to improve the ionic transport, but it is an expensive and subtractive technique, which removes excess material. To be able to scale up structuring to an industrial scale, it has to be cheap, fast, reproducible and additive or generative, therefore, mechanical structuring of electrodes needs to be explored further[4, 5].

1.2 Aim of work

The goal of this thesis is to replace the commercial PVDF binder with a bio-derived binder which enables an aqueous cathode manufacturing process. Thereafter, the goal is to improve lithium transport in porous electrodes by applying mechanical, lateral, perforations. Two mechanical structuring methods with five different structures will be tested to optimize diffusion in an electrode by using engineered macro-pores.

Chapter 2

Introduction

For most energy storage applications, the lithium-ion battery (LiB) has been the easy choice since it was commercialized by Sony Corporation in 1991[1]. This is due the LiBs well rounded properties in being able to store large amounts of energy and deliver high power if needed, while operating safely[6]. The reason for Li being an important part of this energy storage system is two-sided, it is the lightest metal in the periodic table and has the lowest reduction potential of any element. By using Li-ions, we are able to take advantage of high-energy electrochemical processes in our batteries[7].

2.1 Lithium-ion battery components

A battery is a type of energy storage system which stores energy chemically and is able to convert it into electricity through electrochemical reactions. It consists of a current collector (CC), a separator, an electrolyte and two electrodes. The CC acts as the external circuitry and leads the produced electrons out of the cell to be used, the electrolyte acts as an ionic conductor and electrical resistor, to avoid currents from passing through the cell. The separator acts as a physical layer between the two electrodes to hinder short circuiting the battery, while allowing Li-ion transport to take place between the electrodes. LiBs utilize electrochemical reactions where these ions intercalate between the cathode and anode during charge and discharge. The names of the electrodes are given by at which electrode reduction (cathode) and oxidation (anode) reactions take place during discharge. The cathode and anode are generally made of a lithium-metal-oxide and graphite, respectively, where Li-ions are able to move reversibly through their crystal structures[6–8].

2.1.1 Electrodes

The first commercial battery had a lithium-cobalt-oxide ($LiCoO_2$, LCO) cathode and a graphite anode, and was called a *rocking-chair battery*, due to the Li-ions intercalating into the $LiCoO_2$ during discharge and into the graphite during charge[9]. Equation 2.1 and 2.2 shows the reactions at the two electrodes, while Equation 2.3 shows the total reaction during discharge[8]:

$$\text{Anode: } Li_xC \longrightarrow C + xLi_{dis} + xe^- \tag{2.1}$$

$$\text{Cathode: } Li_{(1-x)}CoO_2 + xLi^+_{dis} + e^- \longrightarrow LiCoO_2 \tag{2.2}$$

$$\text{Total: } Li_{(1-x)}CoO_2 + Li_xC \longrightarrow LiCoO_2 \tag{2.3}$$

LCO is still the most used cathode material commercially, but there is an incentive in the industry to move towards chemistries with lower cobalt (Co) content, due to its high price, low abundance, toxicity and human-rights issues regarding the extraction. Nickel-manganese-cobalt-oxide (NMC) is one of these chemistries, with varying amounts of nickel (Ni), manganese (Mn) and Co[9].

There are two additional classes of cathodes to the layered oxide structure, the spinel oxides and the polyanion oxides[10]. These structures can be seen in Figure 2.1.

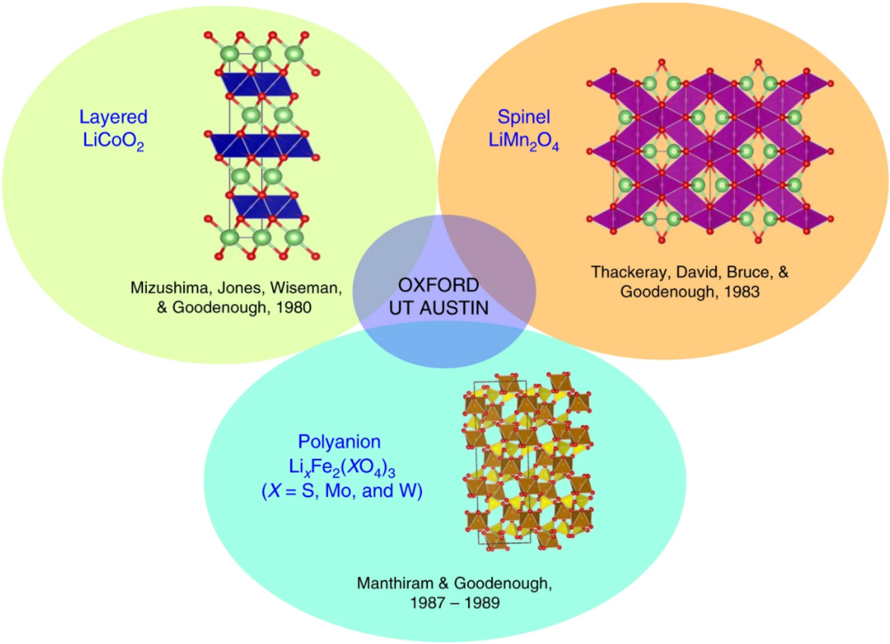

Figure 2.1: The structures of the three different classes of cathode oxides, layered, spinel and polyanion[10].

Cathode

The cathode is the positive electrode during discharge and where reduction reactions takes place. NMC111 is one of the most commonly used materials in cathodes due to its high safety, low cost and high specific capacity. This particular chemistry has equal amounts of the three transition metals, Li, Co and Mn, where each yields the cathode a key property. Ni is the electro-active species and gives the cathode material a theoretical specific capacity of 160 mAh/g. Increasing the amount of Ni yields higher capacity, and is thus a main area of research today. Mn ensures chemical stability by not being susceptible to oxygen depletion of the lattice structure, which would result in capacity decline and voltage fade. The Co gives the material its mechanical stability and increases the electrical conductivity, due to having a significant octahedral-site stabilization energy. This avoids it from migrating through the structure, and becoming metallic during charging[10]. Their overall properties gives the material all the necessary properties to be a well functioning cathode.

Anode

The anode is the negative electrode during discharge and is most commonly made out of a graphite based material. The working principle is the same as layered oxides, where Li-ions intercalate into and deintercalate out of the structure to store and produce energy. Graphite satisfies most of the requirements of an anode material. Only a small amount of energy is lost during charge and discharge, as the intercalation and deintercalation require low potential differences to take place. Graphite also has good electronic and ionic conductivites, is cheap and environmentally sustainable. Some of the issues with the material is the high reactivity with many electrolytes, where unwanted side-reactions, degradation and Li-metal deposition can be promoted. The formation of the solid electrolyte interphase (SEI) is one of these, where the graphite reacts with the electrolyte during the first few cycles of the cell. The SEI does however also passivate the surface and hinders further degradation, while being permeable to Li-ions[11]. Additionally, graphite has a low theoretical specific capacity of 372 mAh/g, it is however significantly higher than that of NMC111, thus the overall battery capacity is limited by the cathode[12].

2.1.2 Electrolyte

For the Li-ion batteries to be able to function, an electrolyte containing Li-ions and that allows them to be transported between the electrodes is necessary. Most electrolytes consists of two or more organic solvents and one or more salts containing lithium, e.g. lithium hexafluorophosphate ($LiPF_6$) and lithium tris(pentafluoroethane)-trifluorophosphate (LiFAP). The mixture of several solvents and salts are often needed for the electrolyte to have all the required properties for use in batteries, listed in Table 2.1. To be able to meet all the requirements, other additives may be added to the electrolyte to e.g. make it non-flammable and hinder it from overcharging[12].

Properties that directly influence the performance of the battery, like high ionic conductivity, large window of electrochemical stability and low electrical conductivity are the most important. The high ionic conductivity yields easy transport between and through the electrodes for the Li-ions, it also avoids polarization and high overpotentials[13]. The large stability window ensures that the electrolyte does not degrade or otherwise react with components of the electrodes, even if it is cycled at a wide voltage window. A low electrical conductivity minimizes the self-discharge rate of the battery and yields a higher capacity[12].

Table 2.1: The properties of an ideal electrolyte[12].

Nr.	Property
1.	High ionic conductivity
2.	Low electrical conductivity
3.	Large window of phase stability
4.	Non-flammability
5.	Large window of electrochemical stability
6.	Non-toxicity
7.	Abundant availability
8.	Inert with battery components
9.	Environmentally friendly
10.	Robust against abuse
11.	Good wettability with electrodes and separator

Electrolyte degradation

The solid electrolyte interphase (SEI) and the cathode electrolyte interphase (CEI) are the result of electrolyte degradation, where it reacts with the electrode material and creates an interface on the anode and cathode, respectively. The formation of the SEI and CEI consumes parts of the electrolye and results in capacity fade of the battery, as less Li-ions are available to intercalate into the electrodes[14]. Formation of the SEI is unavoidable in Li-ion batteries, as it is a result of using voltages outside the stability window of the electrolyte, but the SEI hinders further degradation[12]. Additionally, it impedes Li plating formation, which can be harmful for the performance of the battery. Some of the disadvantages of its formation includes irreversible capacity loss and increased impedance of the battery over time, as it grows thicker. This results in power fade and can lead to heat evolution within the cell, which could be a safety hazard[11].

Transition metals are particularly susceptible to leaching out of the cathode material and into the electrolyte to be incorporated into the SEI. This process causes capacity fading and overall aging of the battery, like the loss of Li-ions presented above. The three transition metals of NMC cathodes (Mn, Ni and Co) are all susceptible to reacting with the electrolyte, which can be seen in a chemical analysis of a cathode post mortem, as the ratio between the three will have changed. Co is the most stable of the three elements and can be used as a reference to Mn and Ni[15, 16].

2.1.3 Separator

As previously mentioned, the separator acts as a physical layer between the cathode and anode and hinders direct contact between them. It must also allow Li-ions to flow through its porous structure and be electronically insulating to hinder self-discharge of the battery. Another important property of the separator is chemical and mechanical stability, in addition to being a safety measure to avoid thermal runaway. Polyethylene (PE), polypropylene (PP) and a combination of the two are common separator materials which have all these properties. Commercial separators are made out of PP-PE-PP trilayers, where the low melting point of PE makes it fill the electrode pores, which increases the resistance of the battery and hinders further operation. The PP is stable at higher temperatures than PE and prevents the battery from short circuiting if the temperature increases uncontrollably[12].

2.1.4 Current collector

The current collectors (CCs) acts as an external pathway for the current produced within the cell, to make use of the energy produced by the electrochemical reactions. Some of the properties that are wanted in a CC is high degree of sustainability, low cost, high electrical conductivity, high electrochemical stability, high strength and low density. There are many materials that can be used as CCs, both for the cathode and anode, like aluminium, titanium, copper, nickel, stainless steel and carbonaceous materials. To get the required stability and conductivity for each application, the materials can have varying structures and designs, e.g. foil, mesh, foam, etching or coating[6].

Aluminium

Aluminium (Al) is the most used material for current collectors in cathodes, at its properties align with the ones explained above. Al almost has as high conductivity as the noble metals, is of low cost and has high stability due to the passive Al_2O_3 layer that forms in air. In addition, it has a high strength and low density[6]. One of its limitations is the low melting point, which hinders high temperature heat treatments of the cathode.

Carbon coated aluminium

Carbon coating is an effective method of improving the conductivity of the CC material. For Al the carbon coating improves the conductivity of the CC, thus achieving a better performing electrode. The coating reduces the contact resistance of the Al and contributes to a larger capacity retention at high currents. It also improves the corrosion resistance of the Al, as it acts as a physical boundary between the coated electrode layer when solved in water [6].

2.2 Electrode design

The three main parameters that decides the microstructure of an electrode is the porosity, the tortuosity and the loading. These are key to control and characterize to get a well functioning electrode with the wanted properties.

The porosity is defined as the ratio between the volume of the pores in the electrode and the total volume of the electrode, and can be found by using Equation 2.4, where V is the total volume of the electrode, C is the ratio of each material in the electrode, W is the weight per area (loading) and ρ is the density of each material[17]. The porosity of an electrode is controlled during calendaring, where the electrode is pressed to the wanted thickness, and influences the ionic transport and the electrical conductivity within the electrode. High porosity allows for easy Li-ion transport and therefore high ionic conductivity, but limits the electrical conductivity, as particle-particle contact is required to get the electrons transported out of the electrode. High porosity yields low energy density, as there is less active material per volume unit. Low porosity enhances the electrical conductivity and reduces the ionic conductivity. The best overall properties are achieved at 30-40 % porosity for NMC cathodes[5].

$$\epsilon[\%] = \frac{V - W\left(\frac{c_{\text{NMC}}}{\rho_{\text{NMC}}} + \frac{c_{\text{Binder}}}{\rho_{\text{Binder}}} + \frac{c_{\text{Conductive additive}}}{\rho_{\text{Conductive additive}}}\right)}{V} \cdot \mathit{100} \tag{2.4}$$

An electrode's tortuosity is a measure of the complexity of the ion transport paths through the electrode. One way of estimating the tortuosity is relating it to the porosity, the diffusion coefficient of Li-ions in bulk electrolyte (D_0) and the effective and diffusion coefficient of Li-ions in the electrode material (D_{eff}), shown in Equation 2.5[18]. High tortuosity inhibits ionic transport and hence the rate capability of the electrode, thus reducing the tortuosity is necessary for thick, high energy density, electrodes[19]. Since the tortuosity is decided by the electrode structure and how the particles are ordered, it is an anisotropic property, where in-plane and out-of-plane ion transport can be different. Particularly for graphite anodes is this apparent, where the in-plane ionic conductivity is three times larger than the out-of-plane conductivity[20].

$$\tau[\%] = \epsilon \frac{D_0}{D_{\text{eff}}} \tag{2.5}$$

Electrode loading is the ratio between the mass of active material (m_{NMC}) and surface area (A) of the electrode, as seen in Equation 2.6. Electrode loading is closely related to the overall energy density of the electrode, where higher loading yields a higher ratio between active material and components that do not contribute electrochemically. A high mass loading results in a thick electrode with high energy density. When the thickness increases, the power density limits the batteries from being used in applications that need high currents[5].

$$\mathrm{W}[\mathrm{g/cm}^2] = \frac{m_{\text{NMC}}}{\mathrm{A}} \tag{2.6}$$

2.3 Electrode manufacturing

The electrode manufacturing process and the precursors used are imperative for the overall quality of the resulting battery cell. Choosing the correct active material, conductive additive, binder and solvent to meet the requirements of an application can be challenging. Several considerations regarding capacity, electronic conductivity, mechanical integrity, cost and sustainability needs to be made before production is started. The processing itself is also important, as it is time-consuming and expensive, where introducing defects into the microstructure of the electrode could be detrimental for its performance[21].

2.3.1 Wet-slurry processing

Producing a high performance electrode requires three main classes of materials, as mentioned previously, an active material, a conductive additive and a binder. Each gives the electrode a necessary property to function. The active material stores Li reversibly and facilitates energy storage, NMC and graphite are two materials that are used for cathodes and anodes, respectively, as introduced in subsection 2.1.1. The conductive additive facilitates electron transport through the electrode and thus needs to be a non reactive, high conductivity material, and are typically carbonaceous materials like carbon black (CB). The binder secures adhesion between the current collector and the active material, while providing cohesion between the components of the electrode. Polyvinylidene fluoride (PVDF) is currently the state-of-the-art binder. It is electrochemically stable between 0 and 5 V, shows great stability over time with several active materials and has good adhesion to both aluminium and copper current collectors, making it suitable for use in both cathodes and anodes[22].

The constituents of the electrode are dissolved in a solvent and thoroughly mixed into a homogeneous electrode slurry before further processing. The choice of solvent is often decided based on the binder used, where e.g. PVDF requires the use of an organic solvent, usually N-methyl-2-pyrrolidone (NMP). NMP is however costly and toxic for both humans and the environment, which complicates the drying process of the slurry, since all the NMP needs to be recovered after use. This results in a desire for binders which can use cheap, non-toxic and green solvents, like water[22].

Lignin is one of the options for use as a green binder in LiB electrodes, as it is soluble in water, a by-product which exists in large amounts from paper and pulp industry, cheap and non-toxic. It has shown promising results with regards to overall electrode performance for both anodes and cathodes, with initial capacity, cyclability and capacity retention being comparable to the non-sustainable PVDF. Aqueous based processing does however also introduce new challenges to the manufacturing process. Li-metal leaching, corrosion of Al current collector, reactions with Ni, poor wetting of hydrophobic carbon and agglomerations[23]. Additionally, in cathodes with NMC as active material, the NMC will react with water and alkalize the solution, resulting in corrosion of the Al current collector foil. Regardless of the challenges of the water based processing, lignin is still a promising alternative as binder to PVDF in LiBs[24, 25].

The electrode slurry is deposited onto the current collector, commercially this is done with a slot-die coater and in lab scale it is done with a doctor blade. Then, the electrodes are dried and the solvent evaporated. This is an energy-intensive step in the manufacturing process and uses up to 20 % of the total energy consumption of electrode manufacturing. During drying the solvent molecules closest to the surface evaporates first, then the following molecules needs to diffuse through the thickness of the coating to get to the surface. During this transport it drags binders and conductive additives towards the surface, resulting in binder migration and yields reduced adhesion between electrode and current collector, increased internal resistance and reduced electronic conductivity near the current collector. Thus, the drying step is important and is further complicated by the use of toxic solvents, like NMP, as it needs to be recovered[22, 23].

After the electrodes have been dried, they are calendared (cold-pressed) to the wanted thickness, which typically is around 35 μm for commercial use[3]. The calendaring process reduces pore volume, optimizes electron transport by pressing more particles into physical contact, improves energy density and optimizes the ion transport through the electrolyte-filled pores. It does however also increase the tortuosity of the electrode, as there are fewer pores in a dense electrode, complicating and elongating the diffusion path of Li-ions in the electrolyte. The optimal properties of an electrode is found at 30-35 % porosity, but at 20 % for anodes and 25 % for cathodes the volumetric energy density is higher which is a more important property for use in e.g. electrical vehicles [22].

The final step of electrode manufacturing is shaping the electrodes into the shapes required by the format of the battery. For prismatic and cylindrical cells long strips of electrodes are used, for pouch cells the electrode is cut or punched into a fixed geometry and for coin-cells which are used for experimental purposes, the electrodes are cut into small circular disks of approximately 15-20 mm diameter[22].

2.3.2 Structuring

Structuring of an electrode alters its morphology and makes it possible to avoid having to compromise between energy and power density, thus optimizing the properties of the electrode. The structures can have different shapes and sizes, and can vary in complexity, but they all function as *macro-pores* which increase the surface area between the solid electrode and the liquid electrolyte. Three of the most common structures are grids, lines and holes, as seen in Figure 2.2.

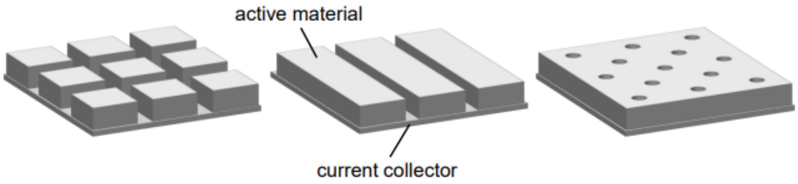

Figure 2.2: Illustrations of the three most common electrode structures, from the left: grid structure, line structure and hole structure[5].

A 2D schematic overview of the electrode structure and how the macro-pores changes it can be seen in Figure 2.3, together with a visualization of how the ionic path is simplified and shortened by structuring the electrode.

Structured electrodes enables new combinations of electrode properties, as introduced in section 2.2, which would be conflicting in unstructured ones. One example is having both a thick and dense electrode, which results in high electrode loading, energy density and electrical conductivity. Simultaneously, the electrolyte is able to wet a larger area of the electrode, yielding a deeper penetration and better wetting of the solid material. This results in a larger fraction of the NMC particles being electrochemically active, as electrolyte contact is necessary for Li-ion transport to and from the particle. The additional macro-pores creates shorter and simpler transport paths for the Li-ions during charge and discharge, thus reducing the tortuosity and increas-

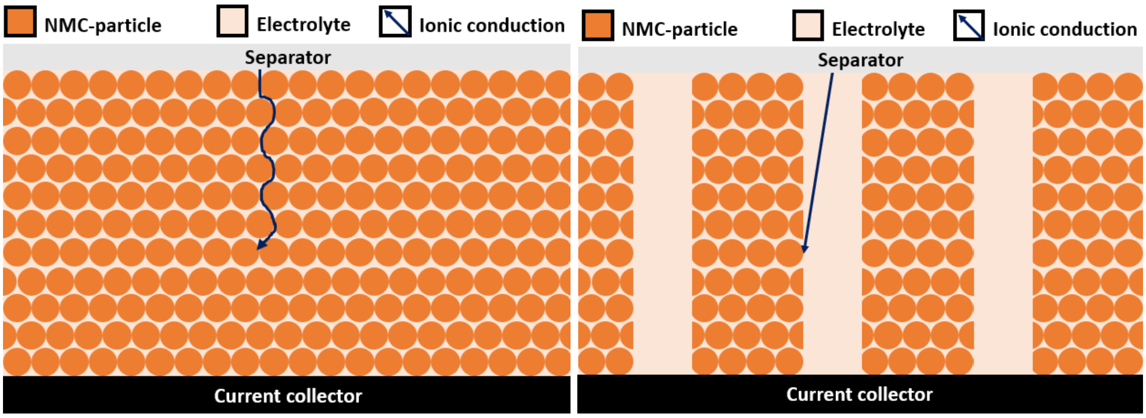

(a) **(b)**

Figure 2.3: Schematic illustration of ionic conduction in a) an unstructured and b) a structured cathode.

ing the ionic conductivity, which facilitates the use of high C-rates and gives a high power density[5].

The majority of research on electrode structuring up until now has been focused on using lasers to structure electrodes of LiBs, whereas some have investigates the use of mechanical methods [26, 27]. Lasers enables the use of precisely engineered structures with limited thermal effects, which have been found to enhance the rate capability of electrodes[5, 19, 28]. Laser structuring does however have some disadvantages, as it is a subtractive technique where material is removed, resulting in excessive waste material. This, in combination with a high price, would make laser-structuring problematic for large-scale production. Hence, exploring alternative methods of creating engineered electrodes, which are additive or generative, would make upscaling simpler[5]. Promising results have been found for introducing structures into electrodes mechanically, but there is some uncertainty to whether or not it is possible to get the desired effects through mechanical methods. If material is displaced and densified during the structuring process, and not removed, it might fill the Li-ion transport routes, and thus no change to the tortuosity is made[5, 26].

Parameters of structuring

The parameters of the structures are another aspect of the structuring of electrodes, where indentation width, indentation depth and spacing between each indentation needs to be optimized for each use. There is a theoretical limitation of the spacing between each structure, as the engineered macro-pores are required to be closer together than the thickness of the electrode for the ion transport to be improved for every active material particle. This is shown in Figure 2.4, where the indentations are too far apart for the ionic transport to be improved for the inner particles. The overall ionic transport for the particles close to the structure is however improved in the scenario seen in Figure 2.4, compared to an unstructured reference. The optimal depth and size of the indentations is dependent on the structuring method and intended use.

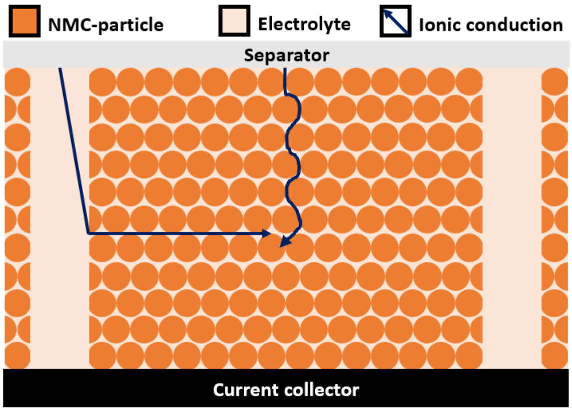

Figure 2.4: Schematic illustration of the theoretical maximum distance between indentations needed to improve ionic conduction to all NMC particles.

For a subtractive technique (like laser structuring) material is removed, thus the width and depth of the indentation can be chosen based on a compromise between enhancing the ionic transport and removing active material. Generally, the ionic transport of Li-ions is greatly improved, even though the spacing between structures is larger than the theoretical limitation and the indentations do not reach the current collector. This can be seen in Figure 2.5, where the Li-ion concentration is greatly improved for all the structured electrodes, independent of spacing between indentations and their depth[19].

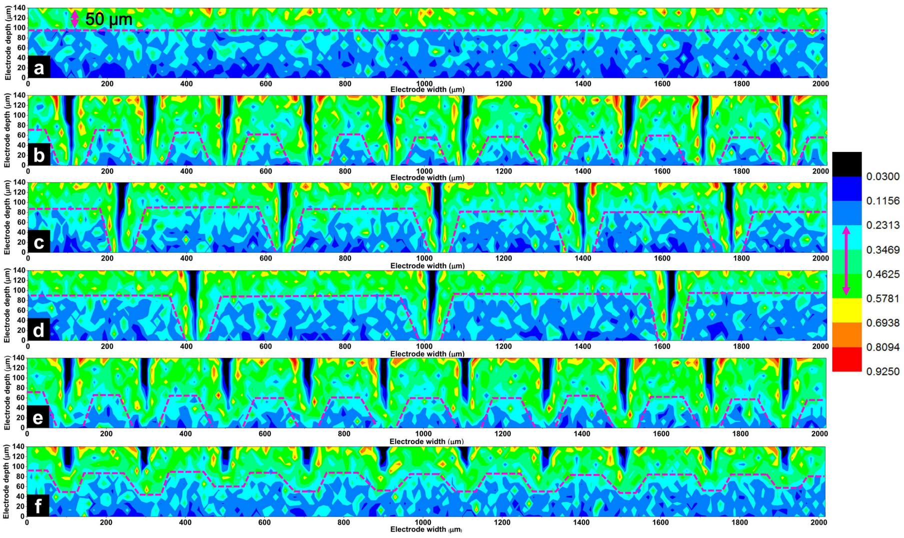

Figure 2.5: Shows the effect on Li-ion diffusion by the depth of indentations and spacing between them[19].

For mechanical structuring, however, the displacement of material causes a change in density for the surrounding areas. If the indentation depth equals half the electrode thickness, the mass of the area under the indentation doubles, resulting in an equal increase of density, illustrated in Figure 2.6. This results in a local tortuosity increase, where the ionic transport is impaired, while it improves in the areas around the indentation. Thus, the spacing, width and depth needs to be considered carefully, to avoid increasing the density in excessive amounts of electrode material, but as shown in Figure 2.5, large spacing and limited indentation depths also have a positive effect on Li-ion transport[5, 19].

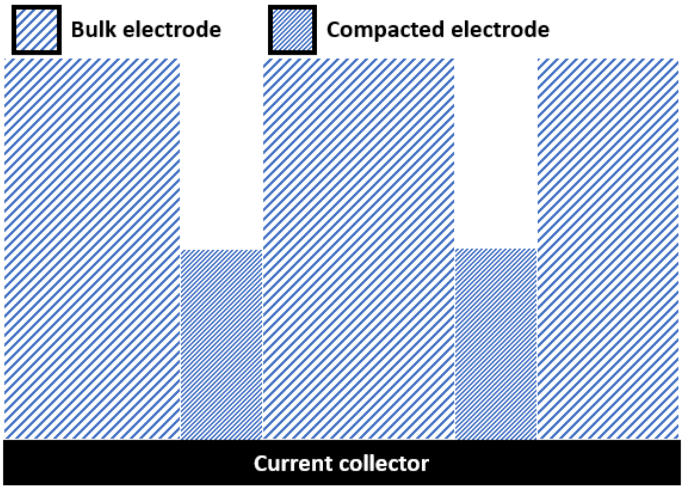

Figure 2.6: Illustration of the increased density of electrode material compressed by mechanical structuring.

2.4 Characterization techniques

Characterizing the quality of an electrode is important for understanding how the precursors, manufacturing processe and structuring influence the performance of the battery cell. Some standard characterization techniques are scanning electron microscopy (SEM), energy dispersive X-ray spectroscopy (EDS), galvanostatic cycling, electrochemical impedance spectroscopy (EIS) and potential step chronoamperometry (PSCA).

2.4.1 Scanning Electron Microscopy

SEM acquires various information from a sample by using a focused electron beam. The electron beam produced several products which contain information about the material being analyzed. Some of these are secondary electrons (SE), Auger electrons (AE), backscattered electrons (BSE) and characteristic X-rays. SE are a result of inelastic interactions between the incident electrons and the sample. These are primarily used to take images of the surface and topography of the sample[29]. All samples that are imaged in SEM need to be conductive, but a thin conductive coating of gold or carbon can be applied to non-conductive species[30].

EDS is a technique which is done in combination with SEM to gain information about the chemical composition of the sample. The characteristic X-rays are used to get a quantitative and qualitative analysis of the material, through software processing of the energy spectrum and the measured intensities. As with SEM, there is little sample preparation needed, where the only requirements are that it is electrically conductive and dry[30].

2.4.2 Galvanostatic cycling

Electrochemical testing is essential to analyze how a battery performs, particularly when a new electrode active material is introduced, the electrolyte is changed or some other aspect of the cell is modified. The most used electrochemical testing technique is galvanostatic cycling, where one *cycle* represents one full charge and discharge of the electrode, with a constant current (C-rate). The charge and discharge process is terminated when a certain charge has been passed, or a given voltage is reached. A typical cycle starts at 3 V, where the battery is charged to 4.3 V, then discharged back down to 3 V. These limitations are used to avoid overcharging and over-discharging the battery, where other components of the cell than the active material breaks down to provide or absorb electrons, thus degrading the battery[31].

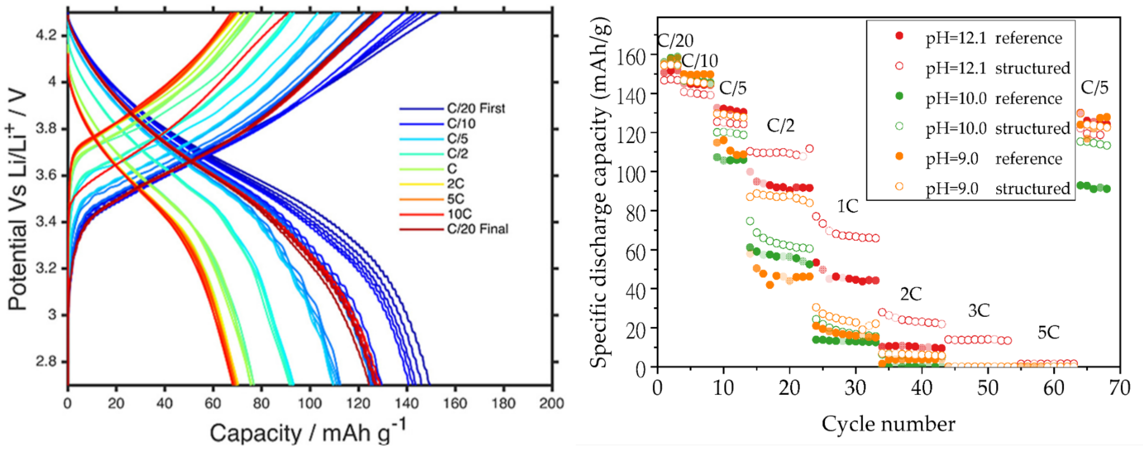

(a) **(b)**

Figure 2.7: Shows two ways of presenting the results of galvanostatic cycling: a) Charge-discharge curve of a battery with a NMC cathode, with C-rates from C/20 to 1 C[32]. b) Rate-performance plot of an NMC cathode, which shows how the capacity fades with increasing C-rates[4].

Galvanostatic cycling measures how much charge the electrode is able to store and deliver at varying currents, which is labeled the charge and discharge capacity of the battery, respectively. Such measurements are often presented in charge-discharge profiles, where the potential is plotted vs. the capacity per mass of active material, the specific capacity. It can also be presented in plots where the specific capacity is plotted against the cycle number, to illustrate how the capacity depends on the C-rates. Examples of the two can be seen in Figure 2.7.

2.4.3 Electrochemical Impedance Spectroscopy

EIS is a technique which measures the impedance in an electrochemical system by applying a chosen potential at a range of frequencies, while recording the resulting current. Voltages from 1 to 10 mV are applied with frequencies ranging from the millihertz scale to several hundred kilohertz. EIS can be used to investigate three main processes at these frequencies, the ohmic loss is measurened in the kilohertz range, activation polarization in the hertz range and mass concentration polarization is measured in the millihertz range. A schematic impedance spectrum of a battery, called a Nyquist diagram (plot), can be seen in Figure 2.8a[33].

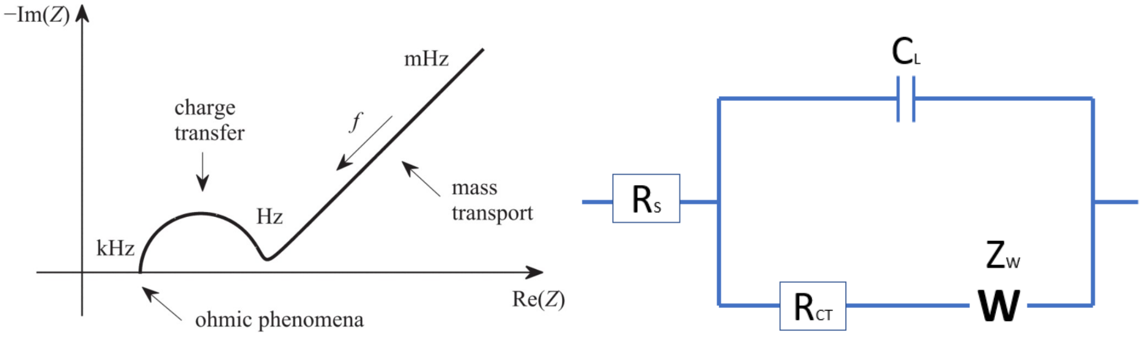

(a) **(b)**

Figure 2.8: Nyquist diagram with its corresponding equivalent circuit. a) Overview of the electrochemical processes which are dominating at the different frequency ranges. b) Equivalent circuit for the Nyquist diagram in (a)[33].

By applying an AC voltage at different frequencies and measuring the resulting current response, EIS can be used to find the impedance of the electrochemical processes taking place within the system. The impedance measurements yields Nyquist diagrams that are paired with an equivalent circuit to correlate each electrochemical process with a contribution to the voltage drop in the cell. One standard equivalent circuit, which fits the Nyquist diagram shown in Figure 2.8a, can be seen in Figure 2.8b. This circuit contains the ohmic resistance (R_S), the charge transfer resistance, (R_{CT}), a double-layer capacitance of charge transfer (C_L) and a Warburg element (Z_w)[31]. Most electrochemical cells does however require more complicated equivalent circuits, as the processes taking place and the geometry of the electrodes are deviating from the theoretical assumptions. More resistances might be needed if there are more than one semi-circle, and there might not be an apparent Warburg element, indicating the absence of a purely diffusion controlled process in the frequency range used. In addition, the double-layer capacitance is often changed to a constant phase element (CPE, indicated by Q in an equivalent circuit), if the semi-circles appear more like the arc of a circle. The CPE originates in a distribution of the current density along the surface of the electrode as a result of an inhomogeneous surface, which porous electrodes have[34]. Thus, an alternative equivalent circuit can be seen in Figure 2.9, where contributions from both cathode and anode are taken into account, as in addition to the ohmic resistance (here R_1), there are two CPEs (Q2 and Q3) and two other resistances

(R2 and R3).

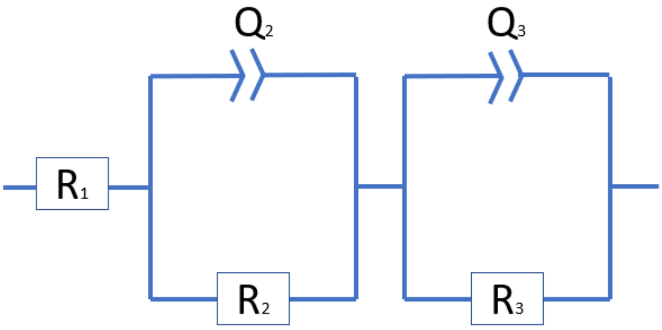

Figure 2.9: An equivalent circuit which models the behavior of a realistic cathode and anode, with constant phase elements (Q) and resistances (R)[35].

2.4.4 Potential Step Chronoamperometry

PSCA is an electrochemical characterization technique used to study thermodynamic and transport properties of materials used in electrochemical processes. In PSCA a single potential step is applied to an electrochemical system and the current response is used to determine the diffusion coefficient of solutes in a host material. This technique is quite similar to the potentiostatic intermittent titration technique (PITT), with the only difference being that PITT uses several potential steps to examine diffusion behavior in a range of voltages, whereas PSCA investigates diffusion in a certain voltage area of the system. The voltage step is most often held until the measured current has fallen below some threshold, corresponding to a low C-rate. It has seen particular use in the characterization of diffusion of Li-ions in graphite electrodes and transition-metal oxide electrodes[36, 37].

The theory behind PSCA is the same as for PITT, and it has several assumptions about the electrochemical system the technique is conducted on. These need to be met for the measurements to be valid for the process being investigated. Thus, for use in LiBs, the experiment has to be designed to comply with the assumptions of the theory behind the technique:

- There is only one diffusing species in the system, and its diffusion coefficient is constant in the applied voltage range
- Diffusion only occurs over the thinnest dimension of a dense electrode
- There is no interfacial reaction resistance between the electrode and the electrolyte
- There are no kinetics related to phase transformations

To meet these assumptions, the use of small steps in voltage ensures diffusion in a single phase region and a constant diffusion coefficient. Using dense and thin electrodes avoids diffusion from occurring in several directions, thus satisfying the second assumption. Finally, a voltage-range where no phase transformations occur needs to be used to meet the final assumptions. PSCA can be used to find the *time constant*, τ, of a system. The time constant corresponds to the required time for 63.2 %

of the total charge to be passed for a system which is subjected to a potential step. It is found by measuring the current resulting from such a potential step and finding the time needed for the current to be reduced to 36.8 % of its initial value. The time constant is a measure of the diffusion coefficient in the system, their correlation is given in Equation 2.7. Here l is the diffusion length of the species and D is the diffusion coefficient[37].

$$\tau = \frac{l^2}{D} \tag{2.7}$$

2.5 Modelling diffusion behavior

Within the electrodes of a battery, Li-ions diffuse through the porous structure and into the NMC particles, so that the electrochemical reactions described in subsection 2.1.1 can take place. Parts of this process can be modelled by diffusion in a plane sheet and could be used to investigate changes in diffusion behavior as a result of structuring cathodes. The two sheets are in a LiB represented by the intersection between the NMC film and the current collector, and the intersection between the film and the separator. The concentration (C) of the charged species, here Li-ions, can thus be described by Equation 2.8[38].

$$\begin{aligned} C = C_1 + (C_2 - C_1)\frac{x}{l} + \frac{2}{\pi}\sum_{n=1}^{\inf} \frac{C_2 cos(n\pi) - C_1}{n} sin\left(\frac{n\pi x}{l}\right) exp\left(\frac{-Dn^2\pi^2 t}{l^2}\right) \\ + \frac{2}{l}\sum_{n=1}^{\inf} sin\left(\frac{n\pi x}{l}\right) exp\left(\frac{-D\pi^2 n^2 t}{l^2}\right)\int_0^l f(x) sin\left(\frac{n\pi x}{l}\right)dx \end{aligned} \tag{2.8}$$

Here, C_1 and C_2 are the surface concentrations of the two sheets, and are assumed to be constants that are equal to another in a fully soaked electrode, thus $C_1 = C_2$. Furthermore, f(x) is the concentration profile of the charged species between the sheets at $t = 0$, which usually is assumed to be zero or some constant. With $f(x) = 0$, $C_1 = C_2$ and normalizing the charge-concentration profile Equation 2.8 becomes:

$$\frac{C}{C_1} = 1 + \frac{2}{\pi}\sum_{n=1}^{\inf} \frac{cos(n\pi) - 1}{n} sin\left(\frac{n\pi x}{l}\right) exp\left(\frac{-Dn^2\pi^2 t}{l^2}\right) \tag{2.9}$$

Equation 2.9 can then be used to find how the charge-profile changes with time, by integrating over the thickness of the cathode, l.

$$Q(t) = \int_0^l \frac{C(x,t)}{C_1}dx = l + \frac{2l}{\pi^2}\sum_{n=1}^{\inf} \frac{cos(n\pi) - 1}{n^2}(1 - cos(n\pi)) exp\left(\frac{-Dn^2\pi^2 t}{l^2}\right) \tag{2.10}$$

If Equation 2.10 is fitted with an experimental charge vs. time curve, an effective diffusion coefficient, D_{eff}, of the system can be found. By comparing the effective diffusion coefficient with tabulated values for ions in the battery, the species and process which limits the ionic transport can be identified. The diffusion coefficients of a typical Li-containing salt and its ions are listed in Table 2.2.

Table 2.2: Diffusion coefficients of the Li-containing salt $LiPF_6$ and its ions, in the liquid electrolyte (D_{liq}) and in the solid NMC particles (D_{SS})[39–41].

Species	Li^+	PF_6^-	$LiPF_6$
D_{liq} [m^2/s]	$2.46 \cdot 10^{-10}$	$3.84 \cdot 10^{-10}$	$1.48 \cdot 10^{-10}$
D_{SS} [m^2/s]	$4 \cdot 10^{-15}$	-	-

The effective diffusion coefficient and the experimental time constant can be used to calculate the diffusion length of the charged species, by using Equation 2.11. Finding the diffusion length can then be used to further identify the limiting transport process in the electrochemical system.

$$l = \sqrt{D_{\text{eff}} \tau} \tag{2.11}$$

Chapter 3

Experimental Work

The chapter contains an overview of the chemicals, apparatuses and procedures used in the experimental work. Manufacturing of cathodes and battery cells will be the focus, with characterization and testing of these.

3.1 Chemicals and apparatus

The four precursors used to make the NMC cathodes are lithium-nickel-manganese-cobalt-oxide (NMC111), with equal amounts of the three transition metals (Ni, Mn and Co), carbon black (CB), lignin and distilled water. These species are listed in Table 3.1 with information regarding their function, state and manufacturer.

Table 3.1: The four precursors used to make the cathode slurry.

Material	NMC111	CB	Kraft Lignin	Distilled water
State	Powder	Powder	Powder	Liquid
Function	Active material	Conductive additive	Binder	Solvent
Manufacturer	Targray	Imerys	Sigma Aldrich	-

The apparatuses needed in the experimental procedure, from making cathodes to assembling coin-cells, are listed in Table 3.2 with the steps they are used in.

Table 3.2: The apparatuses used in the manufacturing of NMC cathodes and coin-cell assembly.

Name	Function
Mettler AE 260 DeltaRange	Analytical balance
Thinkymixer ARE-250 CE	Mixing of precursors
Mini Tape Casting Coater MSK-AFA-HC100	Casting of slurry
Heraeus VT 5042 EK Vacuum Oven	Drying of cathodes
Mbraun LABMASTER Pro SP	Assembling of cells
TMAX-Pneumatic1	Coin cell crimping machine

3.2 Battery production

The battery production route can be divided into two main sections, the cathode manufacturing and the cell assembly, which again can be divided into several substeps, as seen in Figure 3.1.

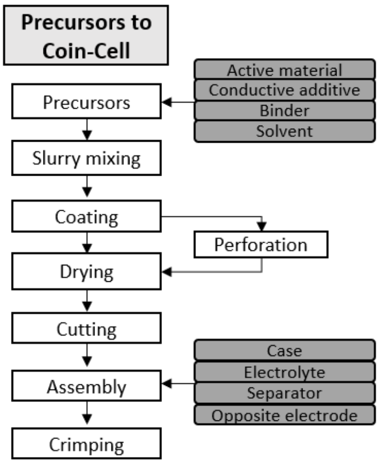

Figure 3.1: Schematic of the different steps in the production of a lithium-ion coin cell, from precursors to finished cell.

3.2.1 Cathode manufacturing

The cathode manufacturing started with making a 1:10 wt% solution of lignin and distilled water (containing 5 % ethanol) by mixing with a magnet stirrer over night at 50 °C. The ethanol evaporates over night. CB was mixed with the lignin solution in a 30 minute mixing program, which was separated into three 10 minute steps with speeds of 1500, 2000 and 1500 rpm. Additional water was added to get the wanted dry-to-wet ratio, typically 1 to 1.2. Subsequently, the NMC was added and the same mixing program was used to make the slurry. A 90:5:5 weight ratio was used for the NMC, CB and lignin, respectively. The slurry is then tape-casted onto a 16 μm thick aluminium foil coated with a 2 μm thick carbon coating. A doctor blade with an adjustable gap was used to get the intended film thickness. The film was dried for 30 minutes at 50 °C, during which it was perforated with a structuring tool. It was subsequently dried at 60 °C over night in vacuum. To create individual cathodes with 15 mm diameters, the film is cut into circular disks, then the thickness and weight of each is measured to calculate the amount of active material, electrode loading and average porosity. All cathodes were finally dried at 120 °C for 4 hours in vacuum to remove all moisture before being moved to a Glovebox for assembly into coin-cells.

3.2.2 Perforation

The structuring was done during drying of the cathode film, as the solvent evaporates from the slurry. Either the ceramic blades or the silica wafer were used as the structuring tool and placed manually into the slurry after 90-120 seconds, depending on the doctor blade thickness, and pressed down for 5 minutes until it had fully dried.

Structuring tools

One of the structuring tools used was a set of 200 μm thick ceramic blades, and can be seen in Figure 3.2. The tool consists of 100 ceramic knives which were mounted together. The tool yields indents of variable with, depending on the depth of the structure, with 200 μm spacing between each.

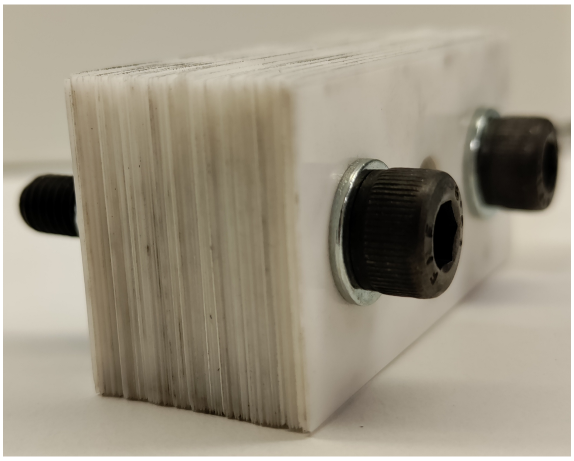

Figure 3.2: Ceramic blades used to create line structures with 200 μm spacing in cathodes.

The other structuring tool was a silica wafer with four different structures. Silica was selectively removed from the wafer with the ICP-RIE (inductively coupled plasma reactive ion etching) technique to create the structures, where a 250 nm chromium mask was used to protect the structures. Two of these structures were line structures with different spacing between the indentations. The large lines (LL) had 200 μm spacing and the small lines (SL) had 100 μm spacing, both with an indentation width of 30 μm. The other two were pillars which created wells in the cathodes, these had a spacing between the pillars of 150 μm, but different pillar size. The small pillars (SP) had a 30 μm radius and the large pillars (LP) had a 50 μm radius. All the structures had a depth of 100 μm and can be seen in Figure 3.3.

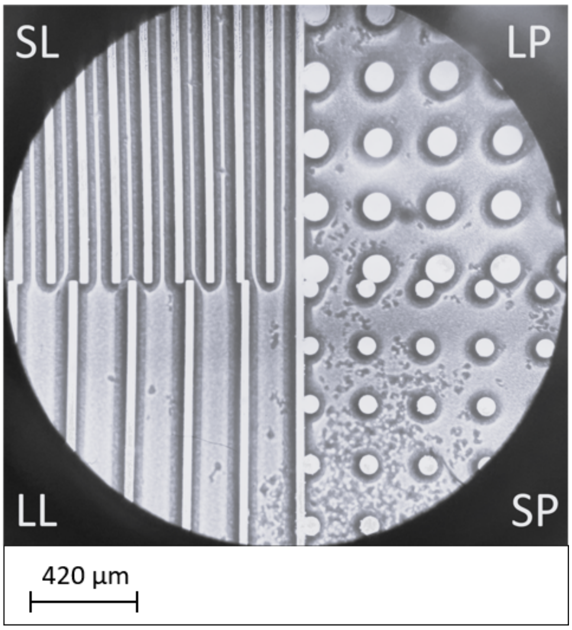

Figure 3.3: Silica wafer used to create four different structures in cathodes.

3.2.3 Cell assembly

The coin cells were assembled in a Glovebox with controlled Ar atmosphere containing up to 1.0 ppm water and oxygen gas. The parts used in the assembly process are described in Table 3.3.

Table 3.3: The parts of the battery pack.

Name	Type	Material	Measurements (diam. x height)
Coin cell can	CR2032	Stainless steel (SUS216L)	20mm x 3.2mm
Coin cell cap	Cr2032	Stainless steel (SUS216L)	19.3mm x 3.2mm
Separator	Celgard 2320	PP/PE/PP	17mm x 20μm
Spacer	CR2032	Stainless steel (SUS216L)	16mm x 0.30mm
Wave spring	CR2032	Stainless steel (SUS216L)	15.4mm x 1.2mm

The ordering of the parts in the coin-cell can be seen in Figure 3.4. Firstly, the cathode was placed into the coin cell cap (positive case) with its active material facing up. Electrolyte (1 M $LiPF_6$ in EC/DMC/DEC = 1:1:1) is deposited on the cathode with a pipette, 20 μL before and 20 μL after the separator is placed onto the cathode, while ensuring that the separator completely covers the cathode. Brushed pre-cut lithium metal (anode) was then placed onto the separator, aligned with the cathode to avoid any of the active material being inactive. The lithium metal was brushed to remove any oxide layer, which could impede the performance of the cell by increasing its resistance. Then, the spacer was placed onto the anode with a wave spring directly on top. Finally, the coin-cell was sealed by the cap (negative case) and crimped at 120 psi in the crimping machine. The spring and spacer were used to avoid damaging the electrodes, as they relieve and distribute the pressure evenly during crimping. The coin cells rested for 1 week before electrochemical cycling to ensure that the electrolyte

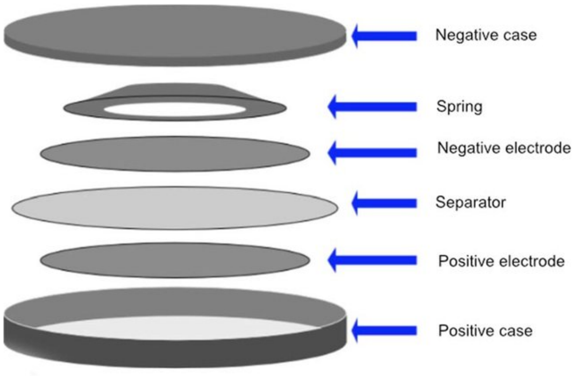

Figure 3.4: Schematic illustration of the ordering and configuration of the CR2032 coin cell[42].

had wetted the cathode completely.

3.3 Characterization Techniques

3.3.1 Scanning Electron Microscopy

SEM was used to characterize the cathodes structurally directly after manufacturing and after finished electrochemical testing. This was done to investigate the initial structures, to see how they changed when exposed to the crimping pressure and the electrochemical reactions that take place during cycling. The dimensions of the cathodes and the structures were measured from the SEM images. A Zeiss Ultra 55 apparatus was used for imaging, with an Everhart-Thornley secondary electron detector. Working distances between 10 and 20 mm were used together with an accelerating voltage of 10 kV for all samples.

EDS was used to chemically analyze the cathodes before and after cycling, to investigate if it changed chemically during testing. The analysis was done in SEM with a Bruker XFlash EDS detector at a working distance of approximately 10 mm and an accelerating voltage of 15 kV. Additionally, Bruker software was used to analyze the energy spectrum and identify the elements.

3.3.2 Galvanostatic cycling

The coin-cells were tested electrochemically through galvanostatic cycling, where they are charged from 3.0 V to 4.3 V and discharged down to 3.0 V, at varying C-rates. Since the anode is Li-metal, all measured potentials are relative to Li/Li^+. Cycling was done with a computer controlled Lanhe CT2001A potentiostat at 25 °C. Three different programs were used to test the batteries, these are presented in Table 3.4. The programs are combined into a full cycling program, where *Form* is run first, then *Soak* and lastly *Rate*. Form contains the three first formation cycles at 0.1 C (16 mAh/g) and ensures an effective SEI formation. Soak has a final cycle at 0.1 C and then 15 at 0.2 C to investigate the wetting of the cathode. Rate tests how the cell performs at normal to high C-rates and checks if the cell was harmed during the high rate-testing by concluding with 5 cycles at 0.1 C. For C-rates up to 0.5 C, the cells were charged and discharged at the same currents, but for C-rates above this, all were charged at 0.5 C, while the discharge rate was increased.

Table 3.4: The three programs the cells were subsequently cycled through, Formation (Form), Soaking (Soak) and Rate-testing (Rate), ending at a total of 54 cycles. EIS measurements was measured after each program.

Program name	0.1C	0.2C	0.5C	1C	2C	2.5C	3C	5C	Cycles
Form	3	-	-	-	-	-	-	-	3
Soak	1	15	-	-	-	-	-	-	16
Rate	5	-	5	5	5	5	5	5	35

3.3.3 Electrochemical Impedance Spectroscopy

EIS was done with a Biologic VMP3 instrument. The cells were charged to 3.6 V at 0.1 C and held at this voltage until the current was lower than 0.01 C (1.6 mAh/g) and a quasi equilibrium state is reached. The frequency range used was from 500 kHz to 10 mHz with a sinus amplitude of 10 mV. EIS was done after each of the three galvanostatic cycling programs shown in Table 3.4.

3.3.4 Potential Step Chronoamperometry

PSCA was done with a Biologic BCS-805 device at a voltage of 3.0 V with a 50 mV potential step. The step was held for 60 seconds. The technique was used to measure the current response of the potential step on cells that had finished cycling. The experimental data was fitted with the diffusion model described in section 2.5 by using the Levenberg-Marquardt method. The effective diffusion coefficient and theoretical time constant of the system were found from the model.

Chapter 4

Results and Discussion

This chapter revolves around the results of the experimental work and will be discussed in the following order:

- Structural analysis of structured lignin binder cathodes
- Chemical analysis of lignin binder cathodes
- Electrochemical analysis of lignin binder cathodes
- Performance comparison of lignin and PVDF cathodes

4.1 Structural analysis of structured lignin binder cathodes

Lignin has in previous works [23–25] been shown to work well as a binder in LFP cathodes, comparably to the unsustainable state-of-the-art alternatives like PVDF. To further investigate the performance of lignin based cathodes, NMC is used as active material and several structures have been used to perforate the cathode surface with the goal to enhance its properties, such as rate performance and wettability. Two structuring tools were used to make five different structures in the cathodes, an overview of these can be seen in Table 4.1. Structured cathodes have been analysed in pristine (uncycled) condition and post mortem, after 54 charge-discharge cycles with C-rates described in Table 3.4.

Table 4.1: The different structures which were made in the cathodes with the expected dimensions from the structuring tool.

Name	Abbreviation	Structure type	Indentation [μm]	Spacing [μm]
Blade perforated	perf	Line	≈ 10	200
Small Lines	SL	Line	20	100
Large Lines	LL	Line	20	200
Small Pillars	SP	Hole	60	150
Large Pillars	LP	Hole	100	150

The measured dimensions of the structured cathodes before and after cycling are summarized in Table 4.2. The average of the dimensions are found from measurements of at least two cathodes with each structure, where some of the SEM images used can be seen in Appendix A Figure A.1-A.5. Here it is shown that the size of the structures varies from the dimensions listed in Table 4.1, due to imperfect structuring during manufacturing. The structures change from pristine cathodes (N) to post mortem (PM) analyzed ones, but not to a significant degree. The width of the structures increase for all cathodes, except large pillars (LP), which likely is due to parts of the material at the edges of the structures being weakened by the structuring and becoming dislodged during cycling, due to stresses induced by the electrochemical reactions. The spacing between the structures should decrease if the width of the structures grow during testing, but this is only seen for the blade perforated and small line (SL) structures. This indicates that the variations in dimensions could be due to local variations in the measured cathodes, as the structuring technique is imperfect. It should also be mentioned that the structures could have been damaged during the opening of the cells, as the performance of the cathodes during testing does not indicate significant deterioration during use. This will be further discussed in section 4.3.

Table 4.2: Measured dimensions of the structured cathodes in pristine condition (N) and post mortem (PM).

Name	Perf	SL	LL	SP	LP
Width (N) [μm]	16.7 ± 7.4	39.8 ± 3.9	48.2 ± 3.2	43.2 ± 1.5	56.3 ± 0.7
Spacing (N) [μm]	195.3 ± 11.7	81.0 ± 3.1	168.7 ± 2.3	142.6 ± 9.4	124.9 ± 2.5
Depth (N) [%]	48 ± 8	30.4 ± 7.2	32.5 ± 4.7	38.9 ± 2.2	49.9 ± 3.9
Width (PM) [μm]	34.3 ± 11.2	49.4 ± 13.0	61.8 ± 5.1	45.5 ± 4.4	54.3 ± 2.1
Spacing (PM) [μm]	187.4 ± 2.5	100.0 ± 11.5	196.8 ± 8.2	126.7 ± 11.9	155.5 ± 4.8

4.1.1 Perforated with ceramic blades

The ceramic blades, shown in Figure 3.2, creates line structures in the cathode surface and can for a pristine cathode be seen in Figure 4.1. The tool structures the cathode with an uneven spacing, as some of the knives have not made contact with the electrode during the structuring step of the manufacturing. The size of the perforations have been found to be 16.7 ± 7.4 μm and the size of the spacing between them 195.3 ± 11.7 μm, when only considering the ones where the knives have structured the cathode. The variations in perforation size and spacing is due to each ceramic knife not being of the exact same thickness and not all being aligned perfectly.

Another aspect of the perforations is the depth of the indentations. The Cross-sections of two perforated cathodes can be seen in Figure 4.2. The perforations were found to get through 48 ± 8 % of the cathode thickness, yielding an increased density of material beneath this area with lower porosity than the bulk. Some of the excess material could also have been displaced to the sides, increasing the density of small regions in between the perforations.

The variable quality of the perforation structures shown in Figure 4.1 could yield cathodes with varying performances, as a structures of higher quality in a thick electrode could outperform a poorly structured and thin electrode. If the spacing-to-thickness

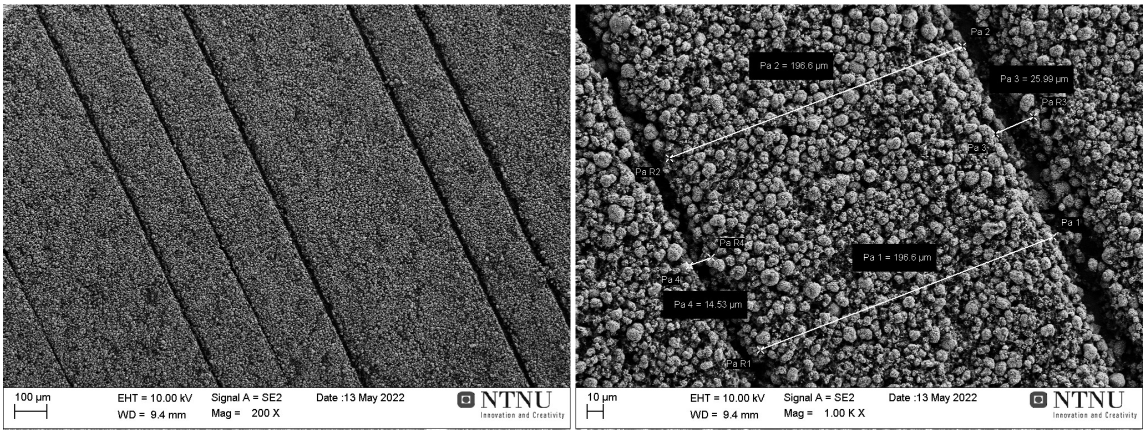

(a) **(b)**

Figure 4.1: Two cathodes perforated with the ceramic blades. a) Overview of several indentations made. b) Measurements of two indentations and the channel between them.

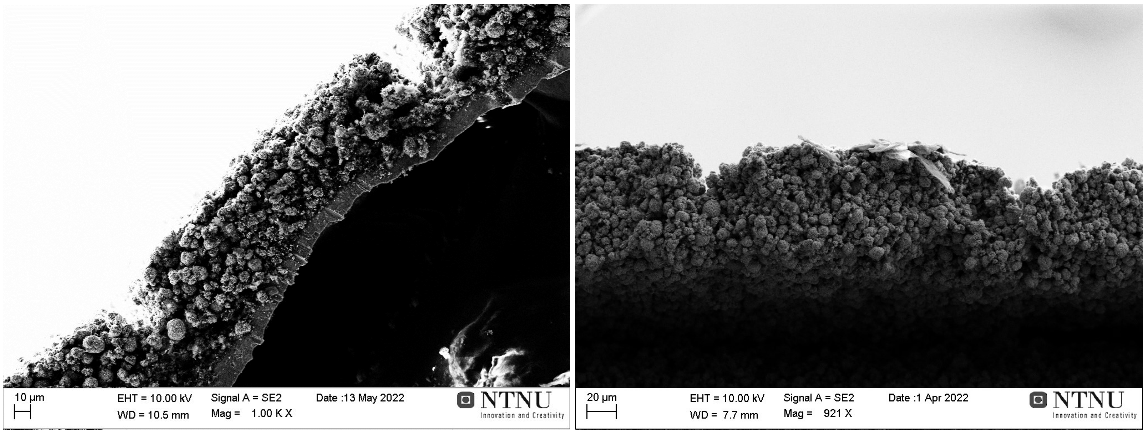

(a) **(b)**

Figure 4.2: Shows the cross-section of two perforated cathodes. a) 60 μm thick cathode with $\approx$ 30 μm indentations. b) 75 μm thick cathode with $\approx$ 35 μm indentations.

ratio is too low, the structures will not have a significant effect on the overall electrolyte/electrode surface area, thus hardly improving the ion transport in the electrode, as explained in subsection 2.3.2. In addition, the depth of the indent decides how much better the electrolyte wets the electrode, but an indent of $\approx$ 50 % of the total cathode thickness should increase the surface roughness and porosity sufficiently to increase the wettability, as found in previous work[19].

Post mortem analysis

Investigating cathodes post mortem showed that some had gone through microstructural changes. Figure 4.3a shows one cathode where the structures have endured being exposed to crimping pressure and electrochemical testing, which was found for the majority of analysed cells. This is however not the case for all cathodes, as can be seen in Figure 4.3b, where the material from the cathode has been dislodged and left in the indentations. This could affect the cyclability of the cathodes, as lose material will not be active, and reduce the available capacity of the battery cell. For cathodes with structures that was able to withstand testing, the size of the perforations was measured to 34.3 ± 11.2 μm with a spacing of 187.4 ± 2.5 μm between the indentations. Hence, the overall spacing between the indentations have been reduced (percentage reduction), while the size of the indentations have increased (percentage increase), indicating an overall deterioration of the structures during cycling.

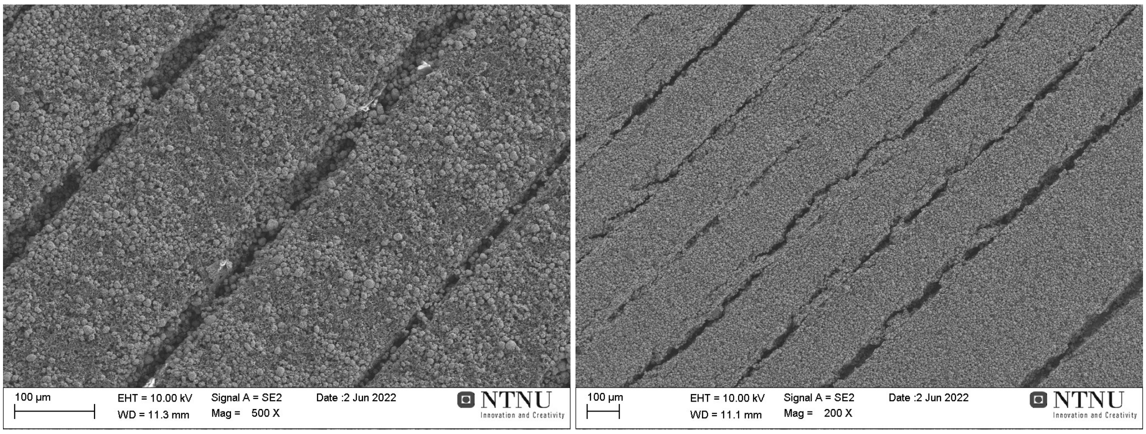

(a) **(b)**

Figure 4.3: Post mortem analysis of blade perforated (perf) cathodes after 54 cycles. a) Surface view of structures that have not changed by cycling. b) Surface view of damaged structures

4.1.2 Small line structures

The small line structures (SL) are similarly to the perforated cathodes structured with lines, with the main difference being half the spacing between the lines and a slightly wider indentation, as listed in Table 4.1. A structured cathode can be seen in Figure 4.4 at two different magnifications, where the average spacing between the indentations was found to be 81.0 ± 3.1 μm with an indentation size of 39.8 ± 3.9 μm. Figure 4.4a shows a successful structuring of a cathode with parallel lines of width close to the expected value. Some agglomerations/pile-ups of NMC particles can be seen in some of the indentations, which most likely is due to a displacement of excess active material when the silica wafer was removed from the cathode. The right side of Figure 4.4b does show some imperfections in the structure, where the electrode between two indentations have been damaged, seemingly by the structuring tool.

Examination of the cross-sections of SL structured cathodes showed that structures reach 30.4 ± 7.2 % into the cathodes, shown in Figure 4.5. This structuring method thus creates finer structures compared to the perforations of the ceramic blade, but the structures are less deep. As discussed previously, the ionic transport would have

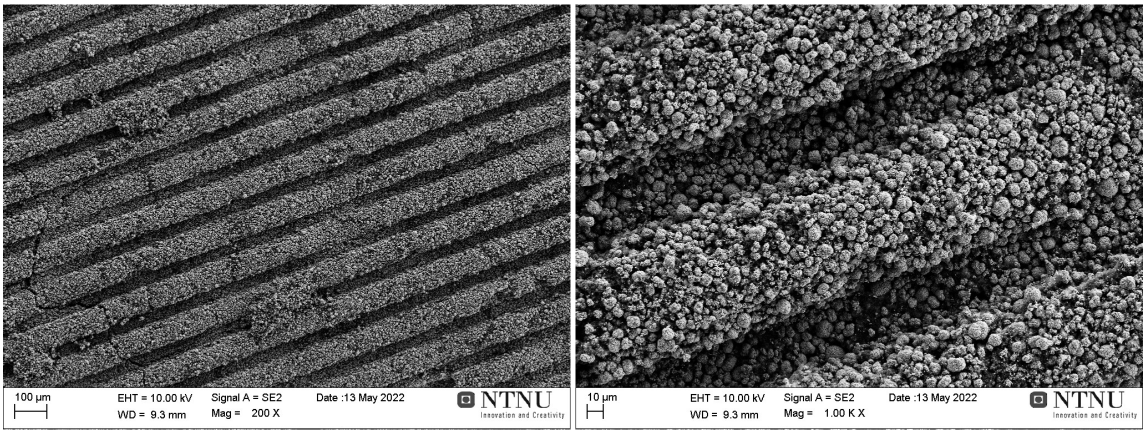

(a) **(b)**

Figure 4.4: Small line (SL) structure in a pristine, uncycled cathode. a) At 200 magnification and b) at 1k magnification.

been improved more by deeper structures, but it should still aid the wetting of the electrode and allow for the electrolyte to fill more pores. The limited depth is most likely due to a form of restructuring after the wafer is removed, as the structuring tool is able to reach 100 μm into the cathode.

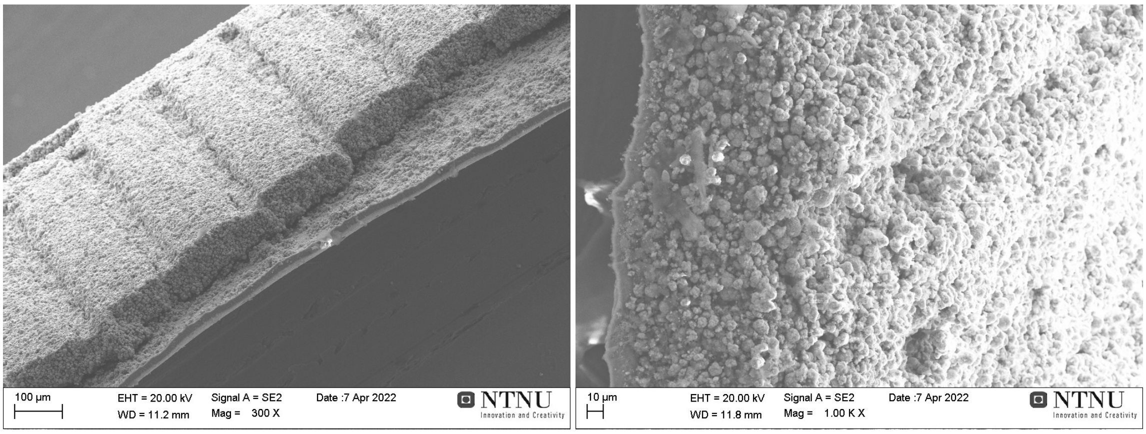

(a) **(b)**

Figure 4.5: Cross-section of two cathodes with small line (SL) structures, the depth of the indentations was found to be one third of the total thickness.

Post mortem analysis

Figure 4.6 shows that the SL structures have been able to withstand the crimping pressure of the crimping machine and the electrochemical testing. The spacing between the structures was found to be 100 ± 11.5 μm, and the width of the indentations 49.4 ± 13.0 μm. The spacing found for the cathodes from the tested cells are larger than for the pristine cathodes, and highlights the variation in quality of the produced structures, as the structuring tool is placed into the electrode slurry by hand. The width of the indentations have generally increased during cycling, and has a large variation, showing that some of the material has come lose from the electrode, similarly to the perforated sample.

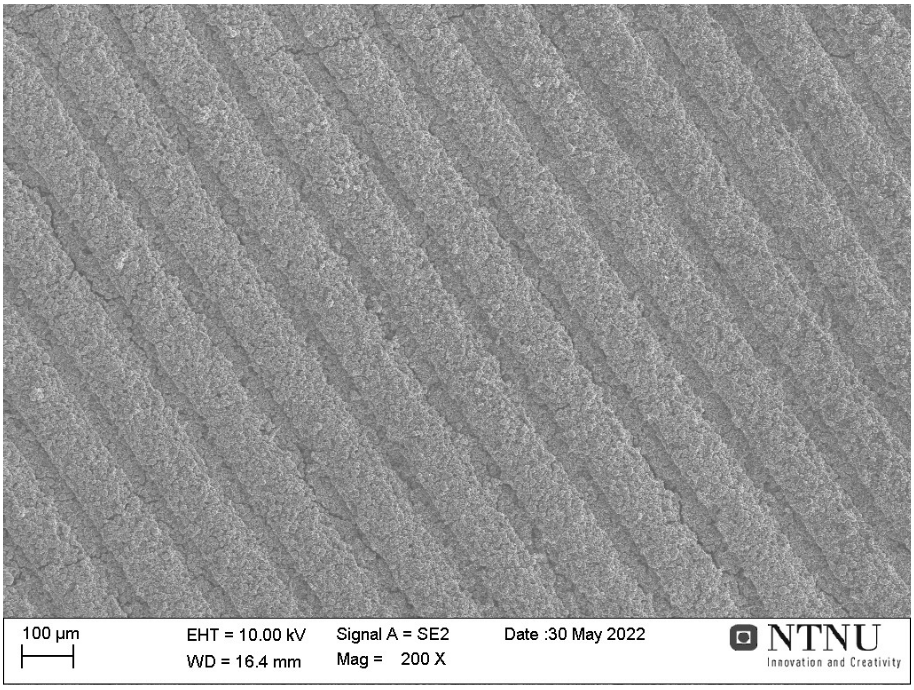

Figure 4.6: Post mortem analysis of a cathode with small line (SL) structures after 54 cycles.

4.1.3 Large line structures

The LL structure also creates lines in the surface of the cathode, with an expected 200 μm spacing. Pristine cathodes with LL can be seen in Figure 4.7, where 4.7a shows a top-side view of high quality structures with a structuring width of 48.2 ± 3.2 μm and a spacing between them of 168.7 ± 2.3 μm. Thus, the structures do not have the same geometry as the structuring tool, which likely is due to the tool not being held still during perforation. If the tool is moved slightly, the width of the indentations increases and the spacing between is reduced as more material is pushed down and to the sides. In addition, some excess material can be seen in some of the lines, where material have been displaced during removal of the silica wafer. Figure 4.7b shows the cross-section of a cathode, where an indentation depth can be found to be 32.5 ± 4.7 % of the total cathode thickness. This is similar to the cathodes structured with SL, indicating a maximal perforation depth of this tool. The structuring does however in great extent appear to be successful.

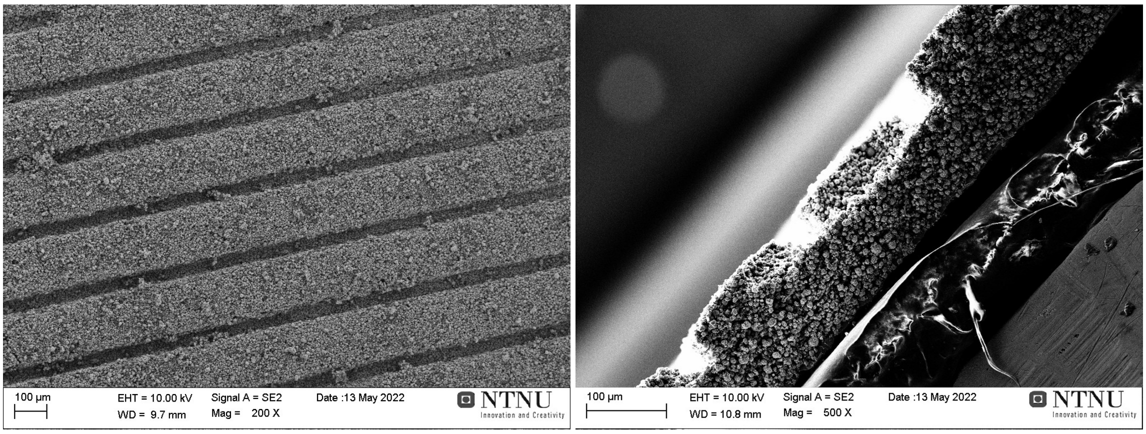

(a) **(b)**

Figure 4.7: Two pristine cathodes with LL structures. a) Surface view and b) Cross-section.

Post mortem analysis

Post-mortem analysis of LL structured cathodes showed the same result as the SL structures, where no significant change has been made to the geometry, since the indentation width was found to be 61.8 ± 5.3 μm and the spacing 196.8 ± 8.2 μm. Figure 4.8 shows one cathode where the structures have remained rigid, with agglomerations of particles in some of the lines, but also shows a form of impurity at the bottom of the lines which has been left from the silica wafer. It was found to be chromium (Cr) in EDS (see section 4.2), which was used as a mask when making the structures in the wafer. These Cr lines are only found for the first few batches of cathodes structured with the wafer, but it could affect the overall performance of the coin-cell, as it hinders direct contact with electrolyte and the cathode material underneath.

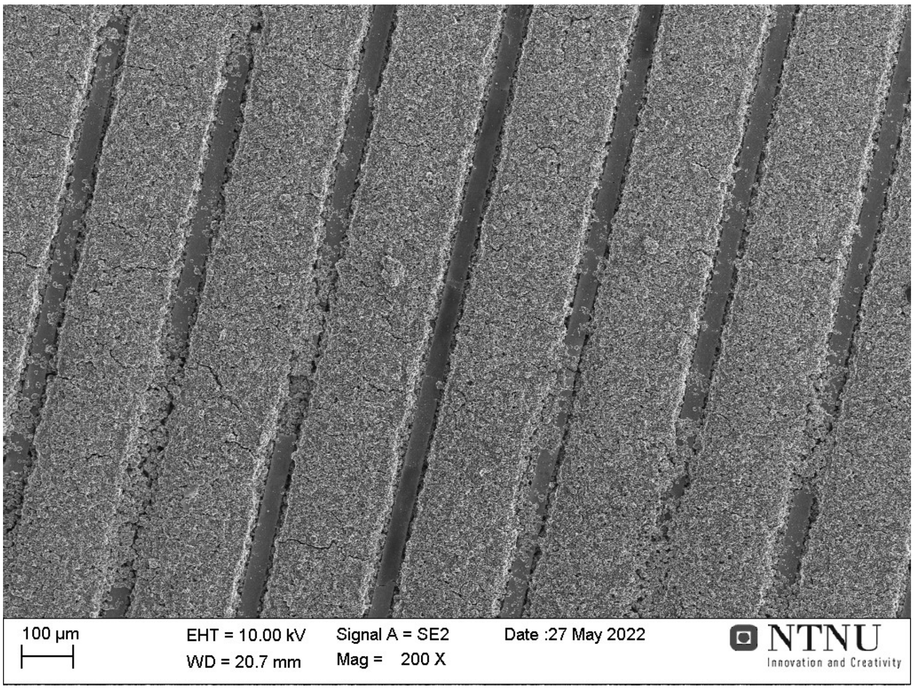

Figure 4.8: Post mortem analysis of large line (LL) structured cathodes after 54 cycles. The structures seem unharmed, but the figure shows chromium impurities in the indentations.

4.1.4 Small pillar structures

The cathodes structured with small pillars will have a hole structure with circular indentations of 30 μm radius and a spacing of 150 μm between each. Figure 4.9a shows four of the hole structures in a pristine cathode. The average radius was found to be 43.2 ± 1.5 μm with a spacing of 142.6 ± 9.4 μm, which is relatively close to the expected values, but does indicate that the structuring have not been ideal. This can be confirmed by Figure 4.9a, as there are cracks forming close to the SPs and one of the holes is much larger than the others, where material has come loose from the sides. The overall quality of the structures does however appear good, as can be seen in Figure 4.9b, where several evenly spaced holes can be observed, with a depth of 38.9 ± 2.2 % of the total cathode thickness.

Post mortem analysis

After cycling the structures does not appear to change in a significant degree, as seen in Figure 4.10, but some deterioration has occurred. The hole radius has increased to 45.5 ± 4.4 μm and the spacing between decreased to 126.7 ± 11.9 μm. The overall variation in sizes has also increased, indicating that some structures are less tough than others, likely due to the structuring technique, where there are variations from batch-to-batch. This could affect the performance of the cathodes, where the ones with less tough structures will suffer from a larger degree of degradation than cathodes that were structured better.

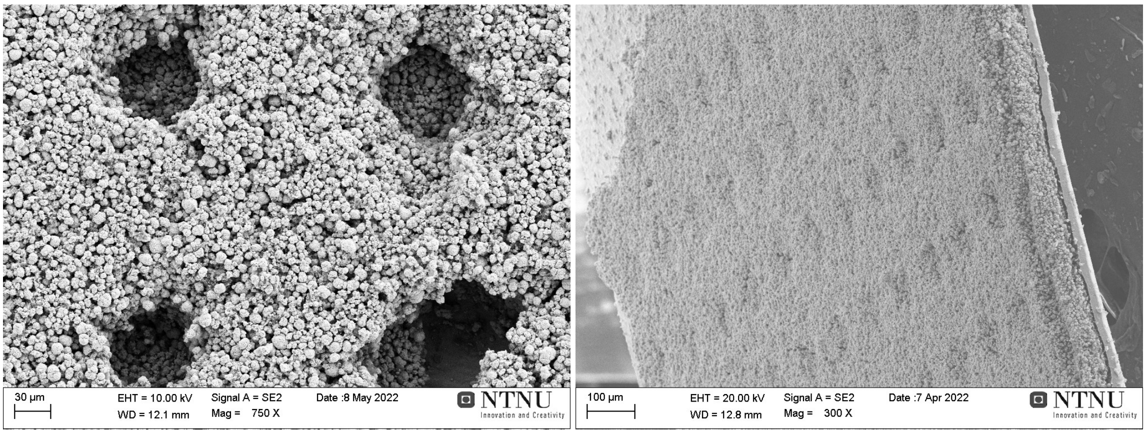

(a) **(b)**

Figure 4.9: Shows pristine cathodes with small pillar (SP) structures from a) Surface and b) Cross-sectional view.

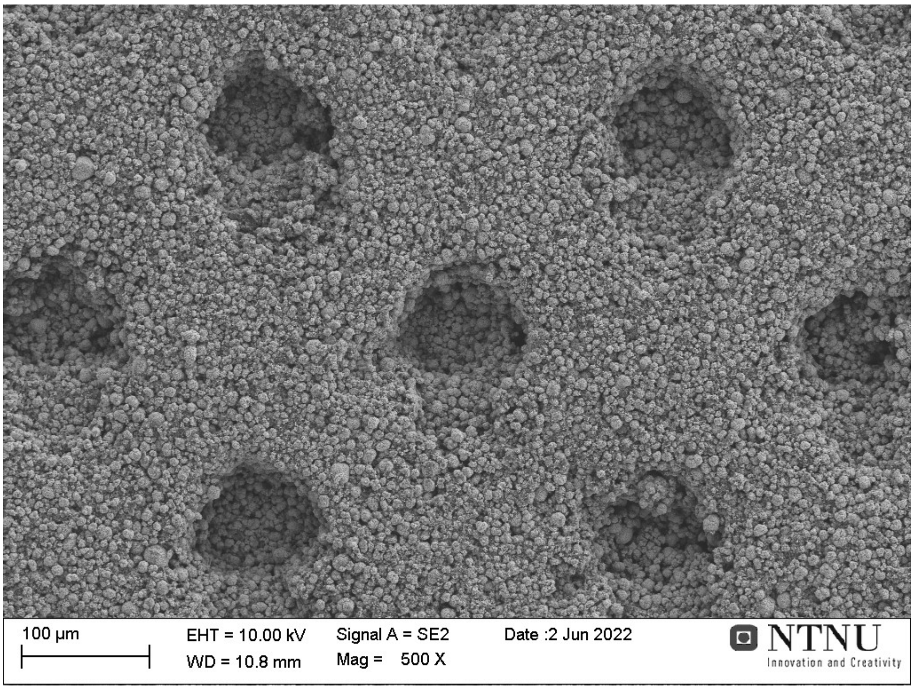

Figure 4.10: Post mortem analysis of a cathode with small pillars (SP) after 54 cycles.

4.1.5 Large pillar structures

LP structured cathodes can be seen in Figure 4.11, where Figure 4.11a shows one of the holes created by the wafer and Figure 4.11b shows the cross-section of a cathode. The radius of the holes was found to be 56.3 ± 0.7 μm with a spacing of 124.9 ± 2.5 μm, and depth 49.9 ± 3.9 % of the total thickness. Thus the dimensions are relatively similar to the structuring tool, listed in Table 4.1, with the main difference being the spacing being smaller, indicating a non-ideal perforation, where some extra material has been displaced in the LPs. The LP have the highest indentation depth of all the structures, yielding cathodes with areas with the highest density, which could yield a reduced electrochemical performance.

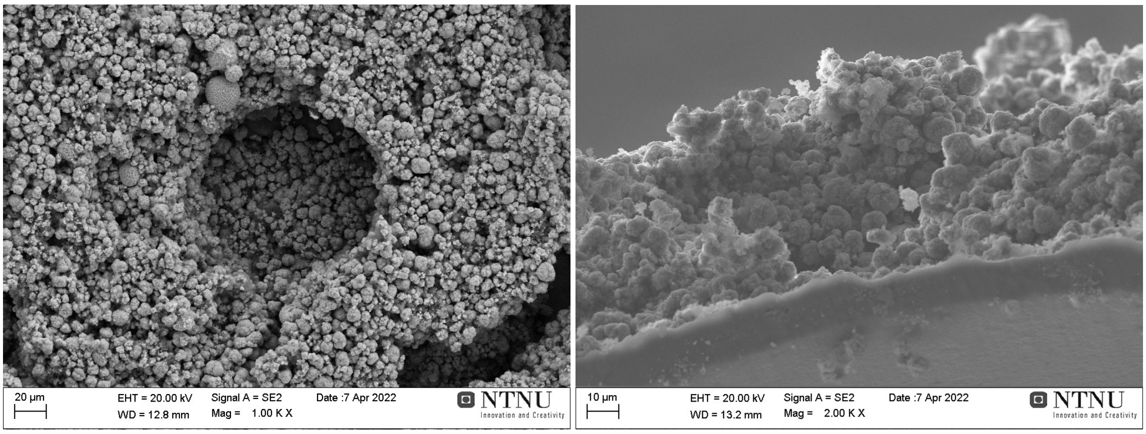

(a) **(b)**

Figure 4.11: Shows two pristine cathodes structured with large pillars (LP). a) Surface view and (b) Cross-section view.

Post mortem analysis

The post mortem analysis of LP structured cathodes showed that inconsistent structuring could be the main cause of a coin-cell failing during testing. Figure 4.12 shows a cathode that has been structured twice, where the structuring tool has shifted during perforation and made a new set of holes in the structure. The radius of the LPs was found to be 54.3 ± 2.1 μm and the spacing 155.5 ± 4.8 μm. Pristine cathodes had a spacing over 25 μm smaller than the cycled ones, highlighting the variation in structuring quality within a structuring type.

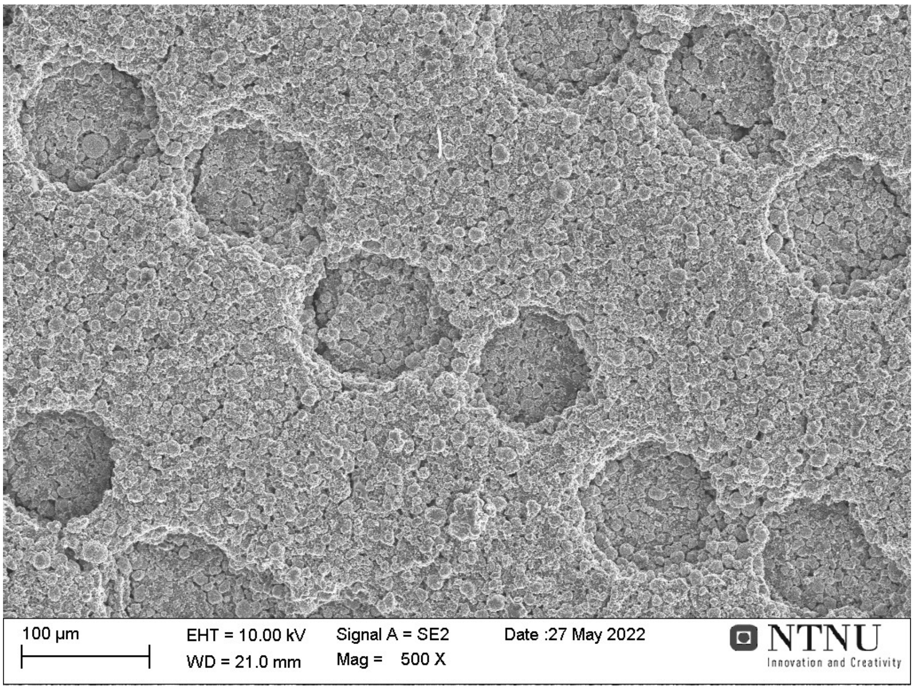

Figure 4.12: Post mortem analysis of a large pillar (LP) structured cathode, showing twice the amount of structures as wanted.

4.2 Chemical analysis of lignin binder cathodes

The chemical analysis is used to search for changes in the electrode material as a result of the electrochemical testing, by comparing pristine with post mortem cathodes. CEI formation on the NMC particles and transition metal leaching are two of the processes investigated in this section by the use of EDS mapping data. The chemical composition of the unstructured pristine and post mortem cathodes are listed in Table 4.3 and the compositions of the structured post mortem cathodes can be found in Table 4.4. The tables also contain the ratios between Ni, Mn and Co, which is used to investigate transition metal leaching.

4.2.1 Transition metal leaching

From Table 4.3 the Ni/Co- and Mn/Co-ratio can be found to be 0.86 ± 0.029 and 0.75 ± 0.025, respectively, indicating transition metal (TM) leaching during the aqueous manufacturing of cathode slurry. As the cathode material used is NMC111, the ratios should stoichiometrically be unity. Since this is not seen, some of the transition metals have reacted with the water during slurry mixing, resulting in a lowered initial capacity of the cathode, as less active material is present. The leached metals could result in battery degradation over time, if it is deposited on the anode and yields further SEI growth. The ratios are however much higher compared to other sources that have investigated TM leaching as a result of NMC being exposed to water. A relative change of less than one weight percent is expected for Ni, Co and Mn when exposed to water less than 6 hours[43, 44]. The low weight percentages of the transition metals listed in 4.3 could also, in part, be a result of inaccuracies in the quantitative EDS measurement, since the electrode material is complex and contains many different elements. To confirm transition metal leaching, a more accurate chemical analysis technique should have been used, e.g. inductively coupled plasma mass spectrometry (ICP-MS).

Table 4.3: Composition of two unstructured cathodes, pristine and post mortem. Shows the Co, Ni, Mn and P content.

Name	Pristine unstructured	Post mortem unstructured
Co [wt%]	30.81 ± 0.73	28.00 ± 0.63
Ni [wt%]	26.50 ± 0.65	24.11 ± 0.56
Mn [wt%]	23.09 ± 0.54	21.00 ± 0.47
P [wt%]	0	2.25 ± 0.09
Ni/Co [-]	0.86 ± 0.029	0.86 ± 0.028
Mn/Co [-]	0.75 ± 0.025	0.75 ± 0.024

There is no indication of TM leaching during cycling, as the ratio between Ni/Mn and Co is within the standard variation for all cathodes post mortem, as can be seen in Table 4.3 and 4.4. This could be a result of the relative change being too small for EDS to detect, and a more accurate technique (ICP-MS) being necessary to observe transition metal leaching. The measured results does however indicate that the water from the cathode slurry is fully removed during drying, as no further degradation takes place after the initial change in composition. It also shows that the lignin does not have a negative effect on the overall stability of the cathode during use, with the regard to the active material.

Table 4.4: Chemical analysis post mortem of the structured cathodes, showing the composition of Co, Ni, Mn and P.

Name	perf	SL	LL	SP	LP
Co [wt%]	26.79 ± 0.61	29.52 ± 0.67	23.29 ± 0.56	28.76 ± 0.66	26.62 ± 0.64
Ni [wt%]	22.56 ± 0.53	25.36 ± 0.59	19.60 ± 0.49	24.42 ± 0.58	22.85 ± 0.57
Mn [wt%]	20.94 ± 0.47	22.22 ± 0.50	18.26 ± 0.43	22.07 ± 0.50	20.68 ± 0.49
P [wt%]	2.07 ± 0.08	1.93 ± 0.08	3.13 ± 0.12	1.98 ± 0.08	2.40 ± 0.10
Ni/Co [-]	0.84 ± 0.027	0.86 ± 0.028	0.84 ± 0.029	0.85 ± 0.028	0.86 ± 0.030
Mn/Co [-]	0.78 ± 0.025	0.75 ± 0.024	0.78 ± 0.026	0.77 ± 0.025	0.78 ± 0.026

4.2.2 Cathode electrolyte interphase formation

The change in phosphorus (P) content from the pristine condition to post mortem shown in Table 4.3 and 4.4 reveals that a cathode electrolyte interphase (CEI) have formed during electrochemical testing. The pristine cathode has 0 wt% P, as none of the precursors contain this element, thus the change must come from irreversible reactions between the active material and the electrolyte. The electrolyte consists of the P containing salt $LiPF_6$, and the CEI can therefore be discovered by observing a change in P content. The electrolyte degradation results in capacity fade during cycling and will result in lower specific capacity for the battery after the cycling program described in subsection 3.3.2.

4.2.3 Contamination from structuring

The contamination seen in Figure 4.7a was further investigated using EDS, and was found to be chromium (Cr). This can be seen in the EDS scans shown in Figure 4.13. The LL structured cathode shown in Figure 4.13a has Cr within the areas that have been pressed in by the silica wafer, and the LP structured cathode in Figure 4.13b have two holes with Cr. This contamination is a result of the mask used to make the structures in the silica wafer, as the lines and pillars are laced with Cr to avoid it being removed by etching. The LP structured cathode in Figure 4.13b was made in the batch after the LL cathode in 4.13a, indicating that the Cr quickly was removed and few cathodes were contaminated, as seen in the other SEM images in section 4.1.

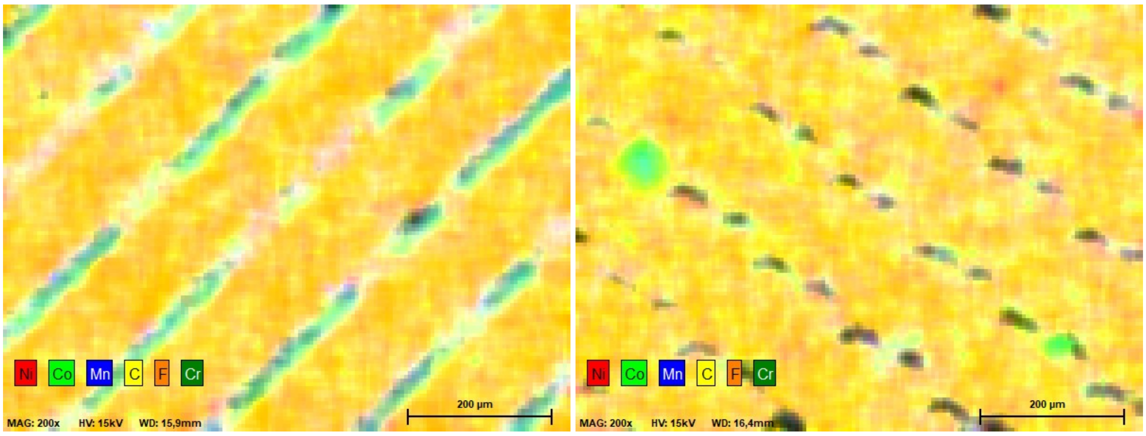

(a) **(b)**

Figure 4.13: Post mortem EDS mapping of two cathodes, a) with LL structures and b) with LP structures.

4.3 Electrochemical analysis of cathodes with lignin binder

The electrochemical analysis is split into three separate techniques which have been used to characterize different properties of the cathodes, both unstructured and structured. These are galvanostatic cycling, used to investigate the performance of the cathodes at varying C-rates, electrochemical impedance spectroscopy, used to see how the impedance of the cathodes change during cycling, and potential step chronoamperometry, used to examine the transport properties of the cathodes. The cathodes used are divided into four groups based on their thickness, these are listed in Table 4.5.

Table 4.5: Explanations of the four thicknesses the cathodes have been grouped into.

Abbreviation	Meaning	Thickness [μm]
LT	Low thickness	≈ 50
MT	Medium thickness	≈ 100
HT	High thickness	≈ 150
UT	Ultra thickness	≈ 200

An overview of the cathodes presented in this section, with corresponding thickness, porosity and initial specific capacity (initial speCap) are shown in Table 4.6. Only the best functioning cathodes will be presented, to show how optimal structuring and manufacturing have affected the performance of lignin based cathodes. Every group listed in Table 4.5 are not represented for every structure, due to difficulty controlling the thickness of the cathodes without calendaring them, and only well-working cathodes being used. In addition, the number of cathodes for each structure varies, showing that some of the structures are more reproducible and easier to get of high quality than others. SL was the easiest to make and has the highest number of well working cathodes, particularly SL-MT with 5. Following SL, the other line structured cathodes, LL and Perf, were the second and third easiest to make of high quality. SP and LP resulted in the fewest well-working cathodes, thus indicating that the hole structures are more difficult to make accurately.

Table 4.6: Overview of the tested cathodes, with the number of cathodes in each group, and the ranges in thickness, porosity and intial specific capacity.

Structure	Name	#	Thickness [μm]	Porosity [%]	Inital speCap [mAh/g]
Unstructured	Un-LT	2	31-56	42.6-46.7	124.8-130.5
	Un-MT	1	78	29.5	140.4
	Un-HT	3	151-158	44.3-55.0	148.0-154.7
	Un-UT	2	181-209	51.7-57.2	156.7-157.9
Blade perforated	perf-LT	3	62-71	23.6-51.6	126.5-140.8
	perf-MT	2	85-100	39.2-49.7	138.9-151.7
	perf-HT	2	147-157	57.1-68.4	152.5-153.4
Small lines	SL-LT	1	68	47.1	139.6
	SL-MT	5	100-115	35.9-51.1	128.9-141.7
	SL-HT	3	160-165	34.1-41.6	152.3-157.3
	SL-UT	2	177-226	38.6-40.7	149.2-155.3
Large lines	LL-T	2	60-72	28.0-42.4	133.9-136.7
	LL-MT	2	103-103	36.7-45.5	139.3-142.0
	LL-HT	2	123-163	53.4-59.8	129.6-134.5
	LL-UT	2	197-210	33.2-36.2	157.0-157.5
Small pillars	SP-MT	2	98-117	45.4-50.6	136.9-152.1
	SP-HT	2	136-142	46.2-57.5	138.1-143.7
	SP-UT	2	181-202	36.6-41.0	152.5-157.3
Large pillars	LP-MT	2	99-104	37.5-40.5	131.7-135.7
	LP-HT	1	146	30.3	149.8
	LP-UT	1	210	41.0	157.1

4.3.1 Cycling performance

The galvanostatic cycling shows that cathodes with lignin binder behaves as expected, with a clear correlation between the specific capacity achieved at higher C-rates, the thickness of the cathode and its porosity. Figure 4.14 shows the potential plotted vs. specific capacity of discharge for two cathodes cycled with the program listed in Table 3.4, where both have specific capacities relatively close to the theoretical value of NMC (160 mAh/g) at 0.1 C. Figure 4.14a shows excellent cycling abilities, where the lines only shift slightly to the left as the C-rate increases, with a specific capacity of over 90 mAh/g at 5 C. This cathode has a thickness of 28 μm and porosity of 44.4 %. The cycling plot shown in Figure 4.14b shows a worse performance, where the specific capacity decreases significantly as the C-rate increases from 1 C, visualized as the red line. This is due to the cathode having a thickness of 100 μm and porosity of 41.3 %. Hence, the properties of the lignin cathode is determined by the thickness and porosity of the cathode, as explained in section 2.2.

The potential vs. specific capacity plots shown in Figure 4.14 highlights an important property of a well functioning cathode, that the initial capacity is recovered after a rate-test when the current is reduced to 0.1 C again. If the capacity is reduced after being cycled at high C-rates, it indicates overall degradation of the battery cell, which could be due to irreversible loss of active material due to cracking or parasitic reactions, like the growth of SEI and CEI[45]. When the initial capacity is recovered, it indicates a cathode with mechanical and chemical stability, which the lignin based cathode appears to be from Figure 4.14.

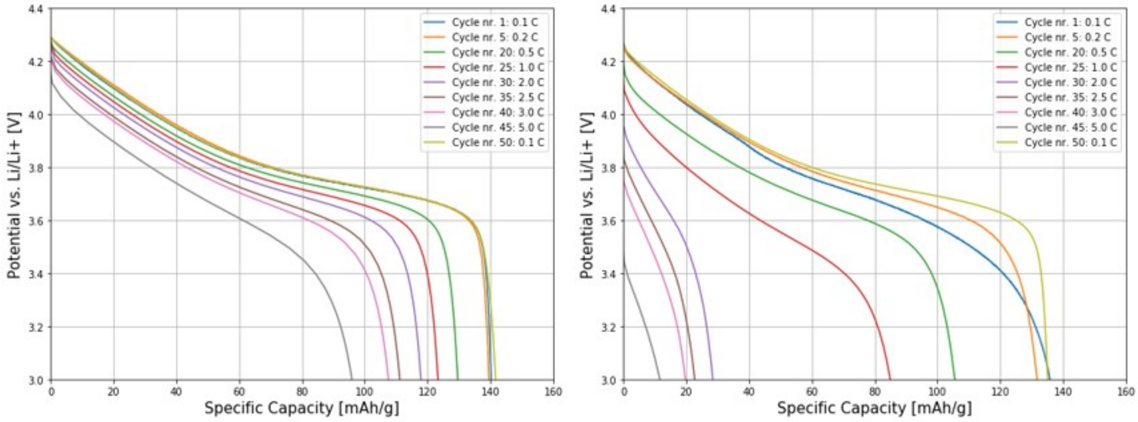

(a) **(b)**

Figure 4.14: Potential vs. specific capacity plot for two cathodes with thickness and porosity: a) 28 μm and 44.4 %, b) 100 μm and 41.3 %.

4.3.2 Rate performance

To highlight how the thickness, porosity and structures influence the rate performance of the cathodes, the specific capacity of discharge is plotted versus the cycle number. By using the last cycle at 0.1 C as a reference for all the following cycles, the rate capability can also be plotted versus the cycle number, to get the relative change in capacity for each C-rate. For all the following rate performance plots, the three first formation cycles at 0.1 C are not shown, and the fourth cycle is used as a reference due to the cathodes having the most similar performance for this cycle (140-150 mAh/g). The three first cycles vary up to 20 mAh/g due to the formation of the SEI layer, so it is excluded in the rate plots.

The lignin cathodes have similar behavior during cycling as the standard PVDF based NMC cathode shown in Figure 2.7b, where an increase in current results in reduced rate capability. Additionally, the rate capability is highly influenced by the thickness and porosity. This can be seen for four unstructured cathodes of varying thickness and porosity in Figure 4.15. The thin unstructured cathode (Un-LT2) can be seen to have excellent rate performance, with high rate capabilities for all currents, and above 50 % capacity retention at 5 C. The thicker cathodes has much lower rate capability, but only the thickest cathode, Un-UT1, reaches 0 % at 5 C, which is higher compared to other lignin-based cathodes[4]. Un-UT1 does however not recover its capacity after the cycles at high C, indicating that some degradation has taken place. This could be structural degradation due to the stresses induced by the high currents used, a chemical degradation where loose active material reacts with the electrolyte, or a combination of both[46]. The low coulombic efficiency does show that a form of chemical degradation takes place, as a large part of the energy supplied during charge is lost to irreversible processes. The performance of Un-HT2 is better than that of Un-MT1 at all C-rates, even though it has double its thickness, which is due to the very low porosity of Un-MT1 of 29.5 %.

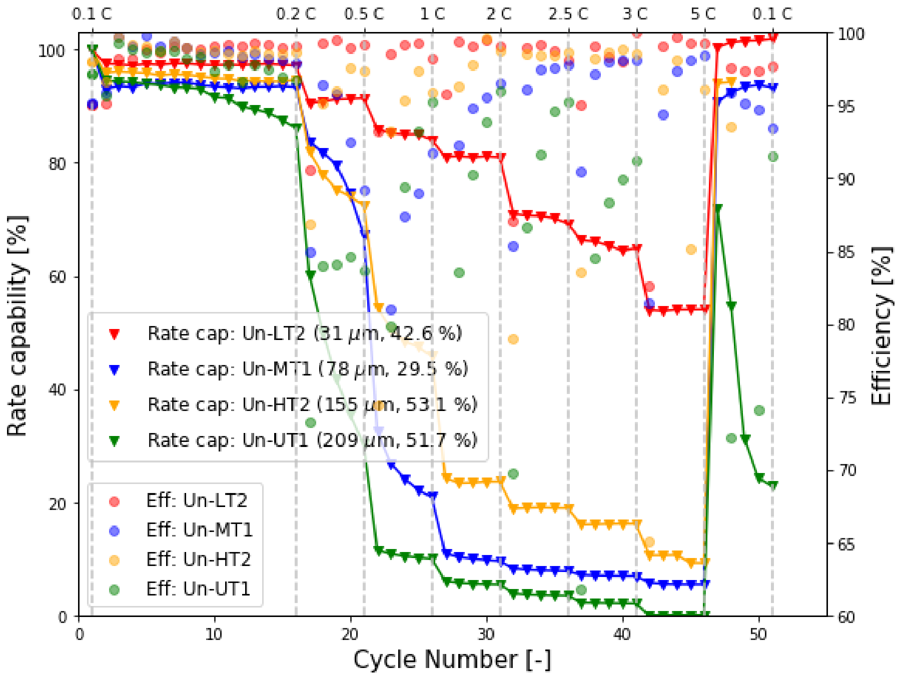

Figure 4.15: Rate performance of four unstructured cathodes, Un-LT2, Un-MT1, Un-HT2 and Un-UT1, which thicknesses of 31, 78, 155 and 209 μm, respectively.

Line structures

All three types of line structures have the expected response to increased C-rates, where the capacity drops step-wise with increasing current. The rate plots of perf, SL and LL can be seen in Figure 4.16, where perf has cathodes represented of low thickness, medium thickness and high thickness, and SL and LL additionally has ultra thickness. Common for SL and LL is that the ultra thick SL-UT2 and LL-UT2 both fail to recover after the rate test, as for Un-UT1 shown in Figure 4.15. This indicates that thicknesses close to 200 μm results in an unstable structure, which is susceptible to degradation at high C-rates.

The rate performance of the medium (Perf-MT2) and high thickness (Perf-HT2) cathodes are very similar, as seen in Figure 4.16a, even though there is a 57 μm difference in thickness between the two, which could be the result of the structures. Perf-HT2 does have a 18.7 % higher porosity than Perf-MT2, but their similar performance does indicate that the structures have an effect on the rate performance for the thickest cathode. The theoretical limitation of the relation between the structure spacing and cathode thickness described in subsection 2.3.2 could be the reason for the structures not having an effect for Perf-MT2 and Perf-LT1. With a spacing of 200 μm between the perforations, the minimum cathode thickness where the structures have maximal effect is 100 μm, which is the thickness of Perf-MT2. Hence, the effect in increased rate capability can be seen for the 157 μm thick Perf-HT2 cathode.

Figure 4.16b does not show a clear effect of the line structures, even though the line spacing of 100 μm implies that the ionic transport should be improved for cathodes thicker than 50 μm. SL-LT1 shows a rate capability of ≈ 80 % up to 2 C, before it

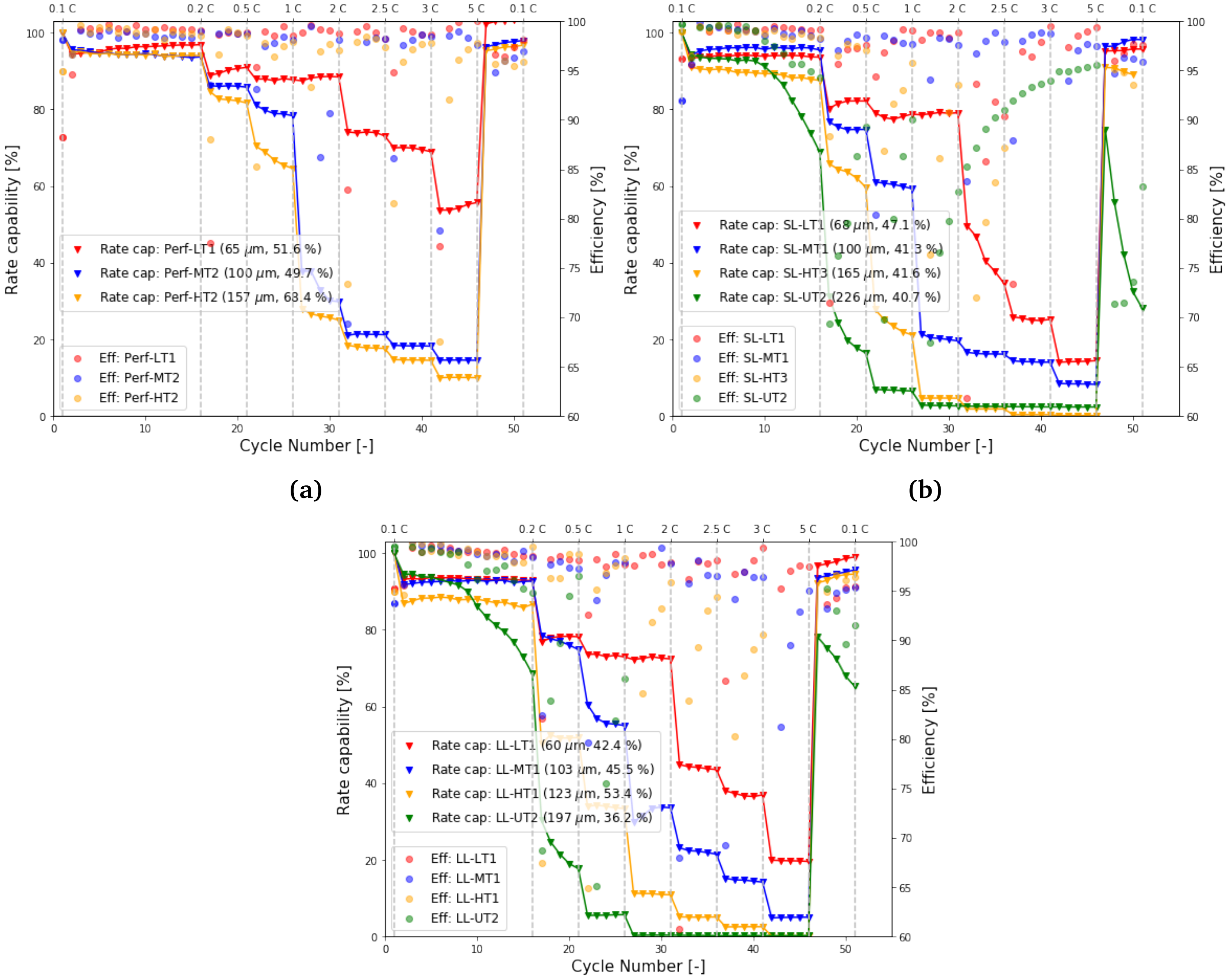

(a) **(b)**

(c)

Figure 4.16: Rate performance of the line structured cathodes, each with 3-4 different thicknesses. a) Blade perforated (Perf), b) Small lines (SL) and c) Large lines (LL).

drops to ≈ 40 %. The significant drop in rate capability is moved to lower C-rates as the thickness increases. For the medium thickness cathode, SL-MT1, it decreases from 60 % at 1 C to ≈ 20 % at 2 C and for the ultra thick SL-UT2 the deterioration starts during the 15 cycles at 0.2 C, where it goes from having 90 % rate capability for the first few cycles, to below 30 % at 0.5 C. This behaviour shows that a ≈ 50 μm increase in thickness shifts the deterioration of rate capability to a lower C-rate, hence the thick electrodes does not appear to have a significant improvement in rate capability by the small lines. This could be due to a too large amount of the electrode material being compressed during the structuring, where too high a percentage of the cathode material is of low porosity for the cathode to perform well at high currents. In addition, the post mortem analysis indicated a degradation of the structures, as the width of the indentations grew during cycling, which could explain why the rate capability is not enhanced.

The rate-plot of the LL structured cathodes shows similar behaviour to the SL cathodes, which can be seen in Figure 4.16c. The step-wise reduction in rate capability with increased thickness is expected here as well, but the rapid decrease at a particular C-rate is not as severe for the LL cathodes. For LL-LT1 the decrease form 2 C to 2.5 C is less than 30 %, and the same is seen for LL-MT1 and LL-HT1. The cathodes generally have less severe reductions in rate capability with increased C-rate, which could indicate that the LL structures are having a positive effect on the ionic transport. As less material is compressed during structuring, the large lines could results in a better compromise between enhanced ionic transport in the bulk material and reduction of porosity in the pressed material, compared to the SL cathodes.

Hole structures

The hole structured cathodes also show the expected behaviour where the rate capability is decreased with increasing cathode thickness, but for the LP cathodes the structures appear to have had a detrimental effect on the cathode, as seen in Figure 4.17. SP and LP are much more dissimilar than the line structured cathodes, where SP has the step-wise drop in rate capability when the C-rate increases. The performance of SP is generally quite good, with a relatively low decrease in rate capability from the medium thickness cathode to those of higher thickness, as can be seen in Figure 4.17a. The rate capability of the SP cathode with high thickness, SP-HT2, is however lower than for comparable cathodes with SL and LL, where SP-HT2 has a rate capability of $\approx$ 20 % at 1 C, whereas LL-HT1 and SL-HT3 has 30 % and 25 %, respectively. For LP, on the other hand, LP-MT2, LP-HT1 and LP-UT1 all have severe reductions in rate capability from 0.2 C to 0.5 C, and they also have less than 20 % rate capability at 1 C, which is seen in Figure 4.17b. In addition, neither LP-HT1 or LP-UT1 recover their rate capability after 5 C, and it continuously decreases during the last cycles at 0.1 C, indicating that the structure is unstable and degradation has occurred in the battery cells. This can also be seen by the low coulombic efficiency of these cathodes, particularly for LP-UT1 with efficiencies below 75 % at 0.1 C. The reason for the poor performance of the LP structured cathodes could be poor structuring, as discussed in subsection 4.1.5.

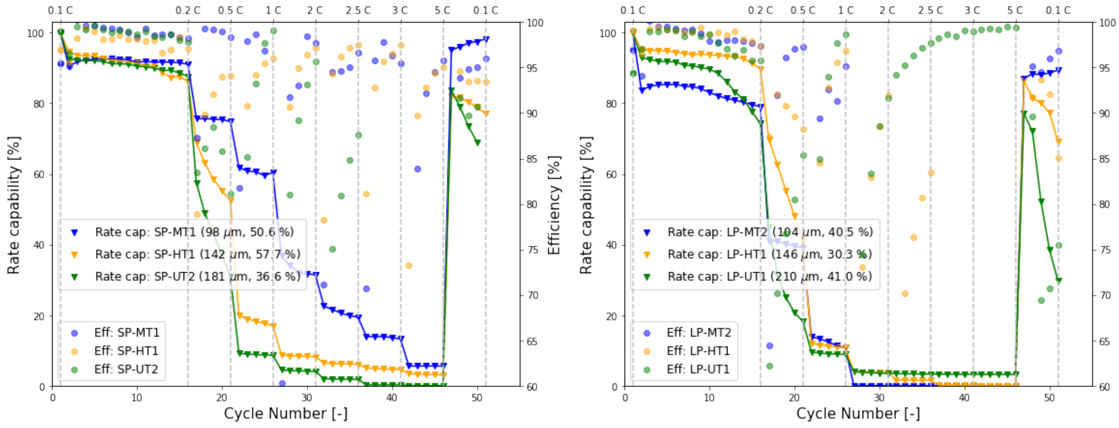

(a) **(b)**

Figure 4.17: Rate performance of the hole structured cathodes with thicknesses from 100 to 200 μm. a) Small pillar (SP) and b) Large pillar LP.

4.3.3 Comparison of the rate performance of the structures

To compare the different structures with each other and the unstructured reference, the average of the rate performance plots of the medium thickness cathodes listed in Table 4.6 have been plotted with standard deviations, and shown in Figure 4.18-4.20.

First of all, the structured cathodes perform better than the unstructured cathodes (Un-MT) at all C-rates, except LP-MT, which indicates that the structuring has had a positive effect on the rate capability of the lignin based cathodes. The low porosity of Un-MT could impede its rate capability compared to the structured cathodes, but its relatively low thickness should partially balance its overall performance. Un-MT has a specific capacity of ≈ 15 mAh/g at 2 C which is reduced to below 10 mAh/g at 5 C. Perf-MT, SL-MT, LL-MT and SP-MT have capacities in the same range at 5 C, of 18, 15, 5 and 7 mAh/g, respectively. This indicates that the ionic transport is not improved substantially for the highest currents, or that another process is rate limiting at this C-rate. A significant difference is however seen for C-rates between 0.2 and 3 C.

Perf-MT has the best rate performance of all the cathodes, as can be seen in Figure 4.18b. It has the highest specific capacity for all the measured C-rates, with close to 120 mAh/g at 1 C, which is over 20 mAh/g better than the second best cathode, which is SL-MT. It also has 40 mAh/g capacity at 2.5 C, which is 15 mAh/g higher than the others. Perf-MT has the lowest decline in capacity for each C-rate, indicating that the spacing, indentation depth and width of this structure results in the best performing cathode, at thicknesses around 100 μm. This could be a result of it having the least intrusive structuring technique, with the smallest and deepest indentations. Some of the performance could be a result of it having a slightly lower thickness than the other structured cathodes, but its porosity is about average.

SL-MT has the second highest specific capacity at 5 C, but performs worse than Perf-MT, LL-MT and SP-MT at the C-rates up to 5 C. It has a significant drop from 1 C to 2 C where it appears to almost reach a minimum rate capability, as it only drops ≈ 20 mAh/g up to 5 C. This could be a result of the SL structures having the smallest

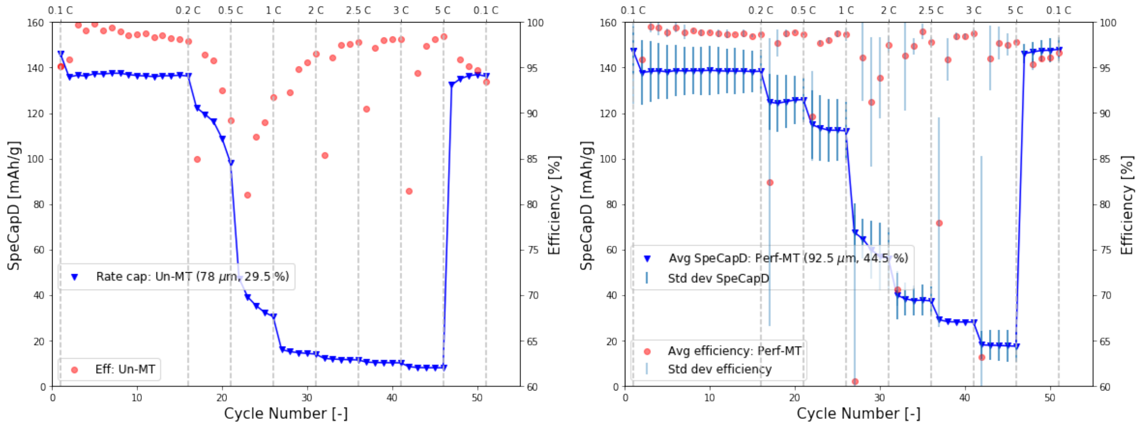

(a) **(b)**

Figure 4.18: Average rate performance of the medium thickness a) unstructured (Un) and b) blade perforated (Perf) cathodes.

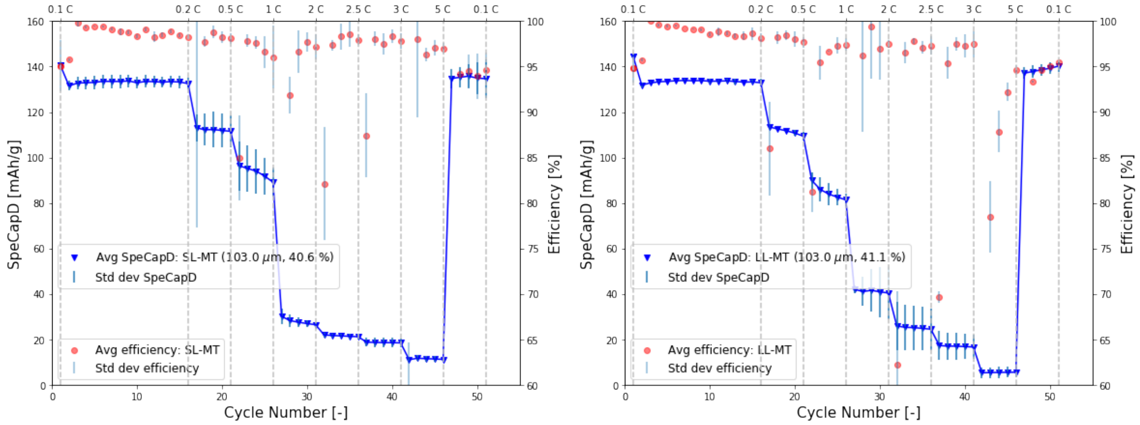

(a) **(b)**

Figure 4.19: Average rate performance of the medium thickness a) small lines (SL) and b) large lines (LL) cathodes.

indentation depth, as listed in Table 4.2, which improves the ionic transport to some extent, but it does not appear to improve the transport adequately to make a difference at the highest C-rates[19].

The LL and SP structure have very similar specific capacities at the tested C-rates, as both follow the stair-like decrease of capacity for each increase in current, while ending below 10 mAh/g at 5 C. This can be seen in Figure 4.19b and 4.20a. Both have improved performance compared to Un-MT in Figure 4.18a, thus the structures appear to improve the ionic transport in the cathode, but not as well as the blade perforations. This could be due to the indentation width of these structures being significantly larger than that of Perf-MT, while having a lower indentation depth. Hence, it appears that a deep and slim indentation improves the ionic transport the most, since the minimal amount of material is compressed, while introducing a deep macro-pore which increases the wetting and ionic transport of the cathode.

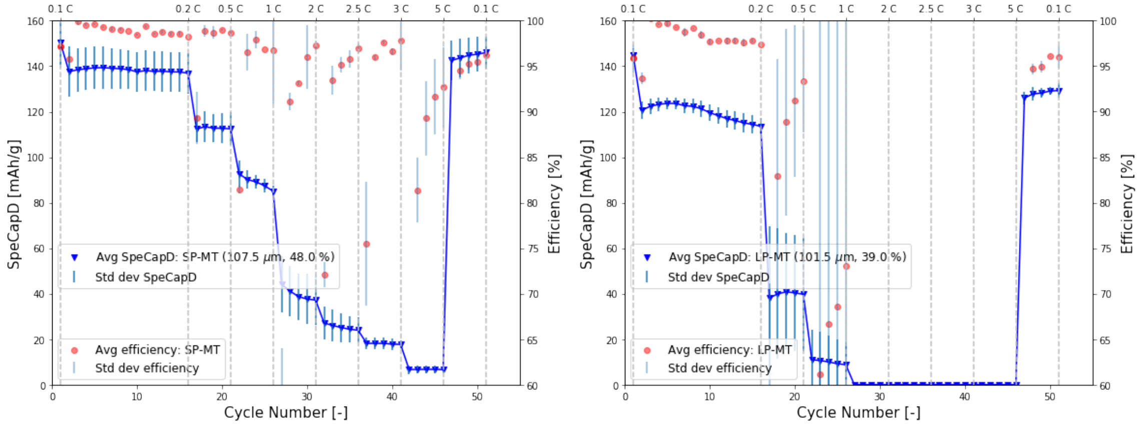

(a) **(b)**

Figure 4.20: Average rate performance of the medium thickness a) small pillar (SP) and b) large pillar (LP) cathodes.

The large pillar structure does appear to be detrimental for the rate capability of the cathode, as the specific capacity of LP-MT is low from 0.5 C (40 mAh/g) and zero for all C-rates higher than 2 C, as can be seen from both Figure 4.17b and 4.20b. This could partially be explained by poor structuring, but since several cathodes all have the same poor performance, it indicates that there is a problem with the structure itself. It is probable that the large pillars reduce the porosity of the material under the indentations to such a degree that the ionic transport is impaired by the structuring. The structure has an indentation depth of almost 50 %, shown in Table 4.2, which yields an area underneath with half of the initial porosity. Additionally, LP has the largest indentations with diameters of 108.6 ± 4.2 μm, resulting in large compressed areas with low porosity and poor ionic transport, detrimental to the rate performance of the cathode.

4.3.4 EIS analysis

The impedance measurements does not indicate high resistances in battery cells with lignin cathodes, which would impede the performance of the cell, which is in agreement with the rate performance discussed previously. All Nyquist diagrams are fitted to the equivalence circuit shown in Figure 2.9 to find the values of the resistance and capacitance elements. Figure 4.21 shows the Nyquist diagram of two unstructured cathodes of low and high thickness, Un-LT and Un-HT, with the fitting values listed in Table 4.7. The first semicircle represents the anode, while the second, larger, semicircle represents the cathode. R1 is the ohmic resistance of the cell and is closely related to the separator and electrolyte. R2 and C2 are correlated to the SEI layer of the anode, while R3 and C3 represents the charge-transfer of the cathode[47, 48]. This can be confirmed by the capacitance values of the cathodes, listed in Table 4.7, where C2 has a value on the scale of 10^{-6} F, which is similar to that of Li_2CO_3 surface films on Li metal electrodes, one typical species in a SEI layer. C3 is larger than C2, indicating that it represents charge transfer on the cathode, as the porous cathode has a much higher surface area than the anode[49]. The resistances of Un-LT and Un-HT are generally quite low, showing that the increase in thickness of the cathode does not have a detrimental effect on the impedance in the cell, but the thicker cathode does have higher values for ohmic and SEI layer resistance. Since the same amount of electrolyte is added to all the coin-cells and the same separator is used, R1 should be similar, but as Un-HT is almost three times as thick as Un-LT, and has more active material, there is less electrolyte per NMC particle. This results in a higher ohmic resistance, but could also be due to consumption of electrolyte during cycling. The significantly higher value of R2 does indicate that electrolyte has been consumed, as the electrolyte appears to have degraded and reacted with active material and yielded an increased SEI layer thickness. R3 is similar for the two cathodes, indicating that an increase in thickness does not effect the charge transfer and does not result in an increased CEI formation[49, 50].

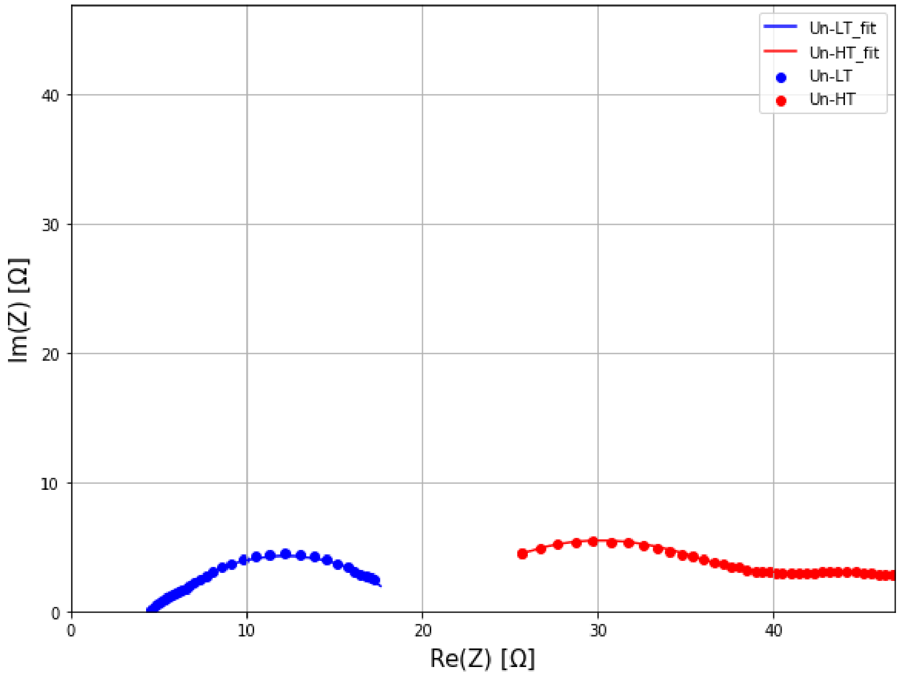

Figure 4.21: Nyquist diagram of two unstructured cathodes of low (Un-LT) and high (Un-HT) thickness, with experimental values and curves fitted to the equivalent circuit seen in Figure 2.9.

Figure 4.22 illustrates how the cathode impedance changes during cycling, for a LL structured high thickness cathode, LL-HT, with the fitted parameters listed in Table 4.8. Generally, all the resistances are low, which indicates a stable cathode with limited degradation during cycling. The ohmic resistance (R1) is a function of the degree of wetting of the cathode, thus, the 15 cycles at 0.2 C (Soak) reduces the ohmic resistance, as the electrolyte is introduced further into the cathode during this cycling program[51]. R1 is increased after Rate, either indicating that some of the electrolyte could have been consumed, or that the separator degrades. From Form to Soak to Rate the SEI resistance (R2) increases step-wise, likely due to the layer growing during

Table 4.7: Fitting parameters from the equivalent circuit seen in Figure 2.9 for two unstructured cathodes of low (Un-LT) and high (Un-HT) thickness.

Parameter	Un-LT	Un-HT
R1 [Ω]	4.69	20.84
R2 [Ω]	0.83	22.05
R3 [Ω]	13.46	12.71
C2 [10^{-6}F]	5.24	0.061
C3 [10^{-6}F]	16.95	19.16

cycling. The charge transfer resistance (R3) decreases as more of the active material comes in contact with electrolyte, as with R1. It does however increase after rate, which could be due to several forms of degradation of the cathode. From the EDS results, it was found that a CEI layer is formed on the NMC particles during cycling, and the layer could be the reason for an increase in charge transfer resistance[52].

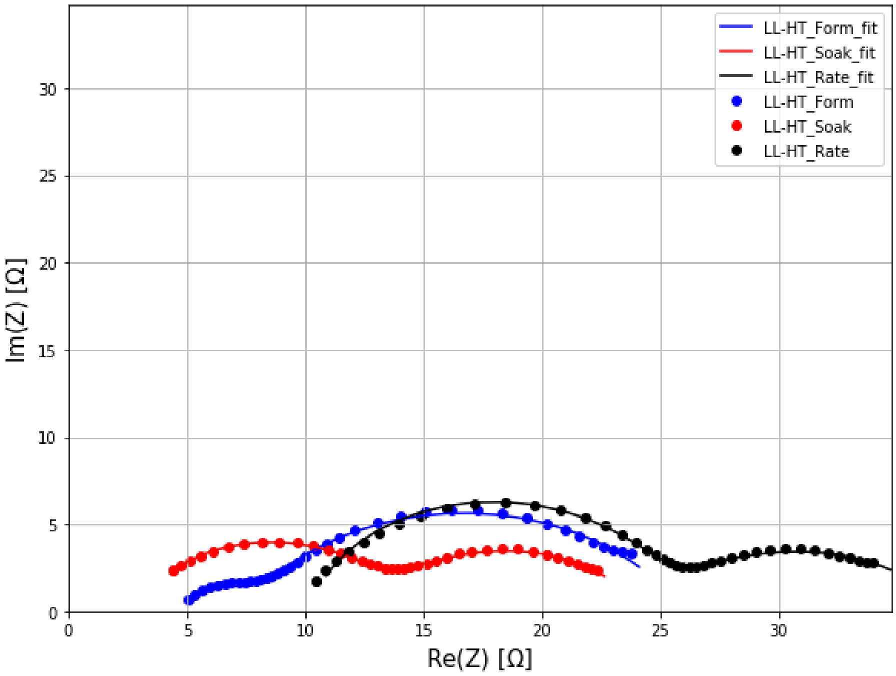

Figure 4.22: Nyquist diagram of a high thickness large line cathode (LL-HT), with experimental values and curves fitted to the equivalent circuit seen in Figure 2.9 after each cycling program, Formation (Form), Soaking (Soak) and Rate-testing (Rate).

Table 4.8: Fitting parameters of the Nyquist diagram of LL-HT, seen in Figure 4.22, after each cycling program.

Parameter	Form	Soak	Rate
R1 [Ω]	5.09	2.90	10.12
R2 [Ω]	2.45	11.08	14.73
R3 [Ω]	18.42	10.37	12.48
C2 [10^{-6}F]	0.432	30.43	0.194
C3 [10^{-6}F]	8.76	0.158	65.09

Effect of structuring

The effect the structures has on the impedance of the battery cell is investigated by comparing the Nyquist diagram of five cathodes with similar thicknesses. The impedance measurements for Perf-HT, SL-MT and LL-HT can be seen in Figure 4.23a and the measurements for SP-HT and LP-UT are shown in Figure 4.23b. Their resulting fitting parameters are listed in Table 4.9.

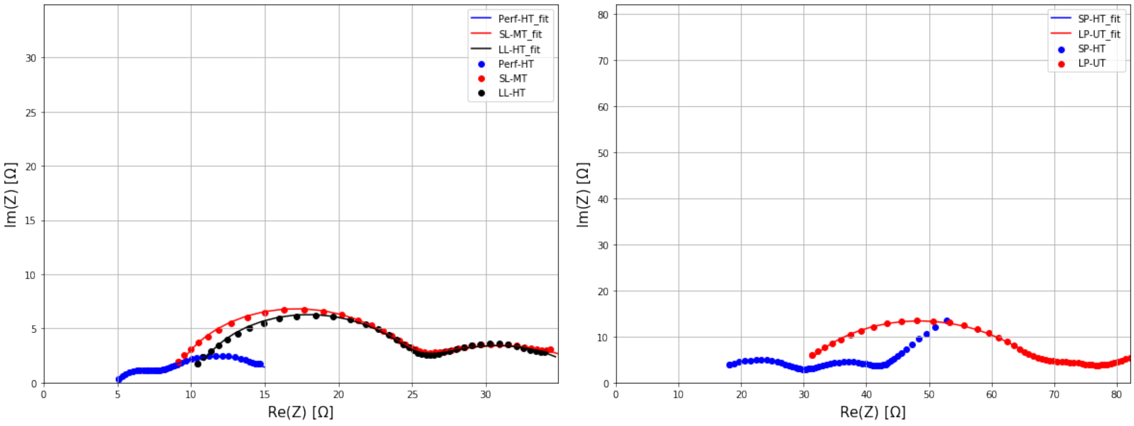

(a) **(b)**

Figure 4.23: Nyquist diagram and the fitted curves of five structured cathodes with medium thickness after rate testing. a) Perf, SL and LL, b) SP and LP.

Generally, the structured cathodes appear to have resistances that are in between the values found for the unstructured cathodes with low and high thickness. For the line structured cathodes, SL-MT and LL-HT are very similar for all the resistance values, even though they have a difference in thickness of 63 μm. Both have lower ohmic resistances than Un-HT, indicating that the structures have improved the wetting properties of the cathodes. The SEI layer resistance is also lower than that of Un-HT, but higher than Un-LT, indicating that the structures have made a difference regarding the SEI growth. This suggests that the structures do not deteriorate the stability of the cathode for medium and high thicknesses, as the SEI layer appears to be thicker for the unstructured cathode. The charge transfer resistances are also similar to the unstructured cathodes, which shows that the structures have not affected the structural strength of the cathodes, as a decomposition of the cathode during rate testing would yield increased charge transfer resistance[46]. Perf-HT stands out from the other two line structures, as R1, R2 and R3 have lower values, closer to Un-LT. The ohmic resistance was found to be 5.23 Ω for Perf-HT, which is very close to 4.69 Ω of Un-LT. This shows that the wetting of the two electrodes are very similar, even though there is a difference of 103 μm in thickness, indicating that the perforations have had a positive effect on wetting. In addition, the SEI layer resistance is over 7 times smaller than that of the other structured cathodes, showing that not much degradation in the form of SEI growth is occurring in the cathode during rate testing. Finally, the charge transfer resistance is very low at a value of 9.23 Ω, which is lower than that of Un-LT. This indicates a chemically and structurally stable cathode with the indented structures[51].

Table 4.9: Fitting parameters from the equivalent circuit seen in Figure 2.9 for five structured cathodes with varying thicknesses.

Parameter	Perf-HT	SL-MT	LL-HT	SP-HT	LP-UT
R1 [Ω]	5.23	8.69	10.12	14.91	28.06
R2 [Ω]	1.98	15.42	14.73	14.33	38.93
R3 [Ω]	9.23	14.52	12.48	16.85	15.19
C2 [10^{-6}F]	0.636	0.184	0.194	0.071	0.081
C3 [10^{-6}F]	26.49	62.44	65.09	30.78	57.95

SP-HT and LP-UT are the structures that deviate the most from the unstructured reference and the line structures, as shown in Figure 4.23b, with LP-UT having the highest ohmic and SEI layer resistances. The small pillar structured cathode, SP-HT, has an ohmic resistance of 14.91 Ω, which is almost 50 % higher than the highest value of the line structured cathodes. It indicates that either the structure impairs the wetting of the cathode or that more of the electrolyte has been consumed during cycling[51]. The SEI layer resistance is however similar to that of SL-MT and LL-HT, thus, the SEI layer has not grown more in SP-HT, and the wetting properties are worse for this type of structure. As mentioned, LP-UT has the highest ohmic resistance, 28.06 Ω, of all the tested cathodes, which partially is due to its high thickness of 210 μm, hence there is less electrolyte available per NMC particle. The SEI layer resistance is however also very high at 38.93 Ω, nearly three times as large as SL-MT, with the second highest value. This indicates an increased degradation of the battery, where electrolyte is consumed when reacting with the active material. The high resistance reveals the formation of a thick SEI layer and could indicate that the large pillars have a detrimental effect on the stability of the cathode. LP-UT has a charge transfer resistance similar to the other structured cathodes, indicating that there is no significant change in the electron-transfer reaction as a result of the structure[46]. From the EDS measurement, the CEI formation appears independent of structuring technique, hence the charge transfer should be unaffected.

The EIS measurements agree well with the results from the galvanostatic cycling, where the blade perforated cathodes performed the best and the cathodes with large pillar structures were the poorest. Perf-HT showed the lowest ohmic, SEI layer and charge transfer resistance, comparable to that of Un-LT, thus resulting in the best rate performance. SL-MT, LL-HT and SP-HT have similar resistance values, which SP-HT having a higher ohmic resistance, yielding similar rate performances of the small line and large line structured cathodes, while being slightly better than that of SP-HT. Finally, the poor rate performance of the LP cathodes seen in the rate plots were further explored with EIS, where its high ohmic and SEI layer resistance show that the cathode is unstable and degrades during electrochemical testing.

4.3.5 Diffusion behaviour

To investigate the diffusion characteristics of the cathodes, potential step chronoamperometry (PSCA) was used together with the model for diffusion in plane sheets, as described in section 2.5. The experimental charge vs. time curve found from PSCA was fitted with Equation 2.10 by using the Levenberg–Marquardt algorithm with sum of least squares. The fitting was done to find an effective diffusion coefficient (D_{eff}) of the system and a theoretical time constant. The theoretical time constant is used to verify the model, to see if it has the same charge vs. time response as a real cathode. Lastly, the effective diffusion coefficient and experimental time constant can be used to find the diffusion length of ions in the cathode structure, with Equation 2.11, and to see if it changes with structuring.

Since the PSCA is measured on NMC/Li-metal half cells, the current response could be a result of either the NMC cathode or the Li-metal anode. To ensure that the measured current is a result of cathodic processes, the current vs. time plot of NMC/Li-metal coin cell was compared to a NMC/NMC and a Li-/Li-metal cell. The three plots can be seen in Figure 4.24, where the behaviour of the NMC/Li-metal cell and NMC/NMC cell are nearly identical, in Figure 4.24a and 4.24b, respectively. Their experimental time constants where found to be ≈ 0.1 s. The Li/Li-cell has a time constant of over 60 seconds, and the current response drops very slowly compared to the NMC/Li-metal cell, as seen in Figure 4.24c, showing that PSCA measures the current responses in the cathode.

The model appears to be working as intended, as the charge vs. time plots are similar and the experimental and theoretical time constants found for the different cathodes generally are very similar in value, this can be seen in Figure 4.25 for unstructured cathodes. Figure 4.25a shows the experimental and modelled charge vs. time curves of an unstructured cathode with 149 μm thickness and 62.4 % porosity, where the modelled behaviour seems to fit the experimental values well. This is seen for all the unstructured cathodes tested, which is shown in Figure 4.25b. The largest deviation in experimental and theoretical time constants is seen for the cathode with 78 μm thickness, which most likely is due to it having a very low porosity of 29.5 %, whereas the others have between 40 and 65 %.

PSCA measurements and fitting of the charge vs. time curve to the diffusion model for the structured cathodes yields higher experimental and theoretical time constants than the unstructured ones. Figure 4.26a and 4.26b shows the time constants of the blade perforated, SL, LL and SP structured cathodes, here categorised based on their porosity, where Figure 4.26a has above and 4.26b below 45 %. Both figures show

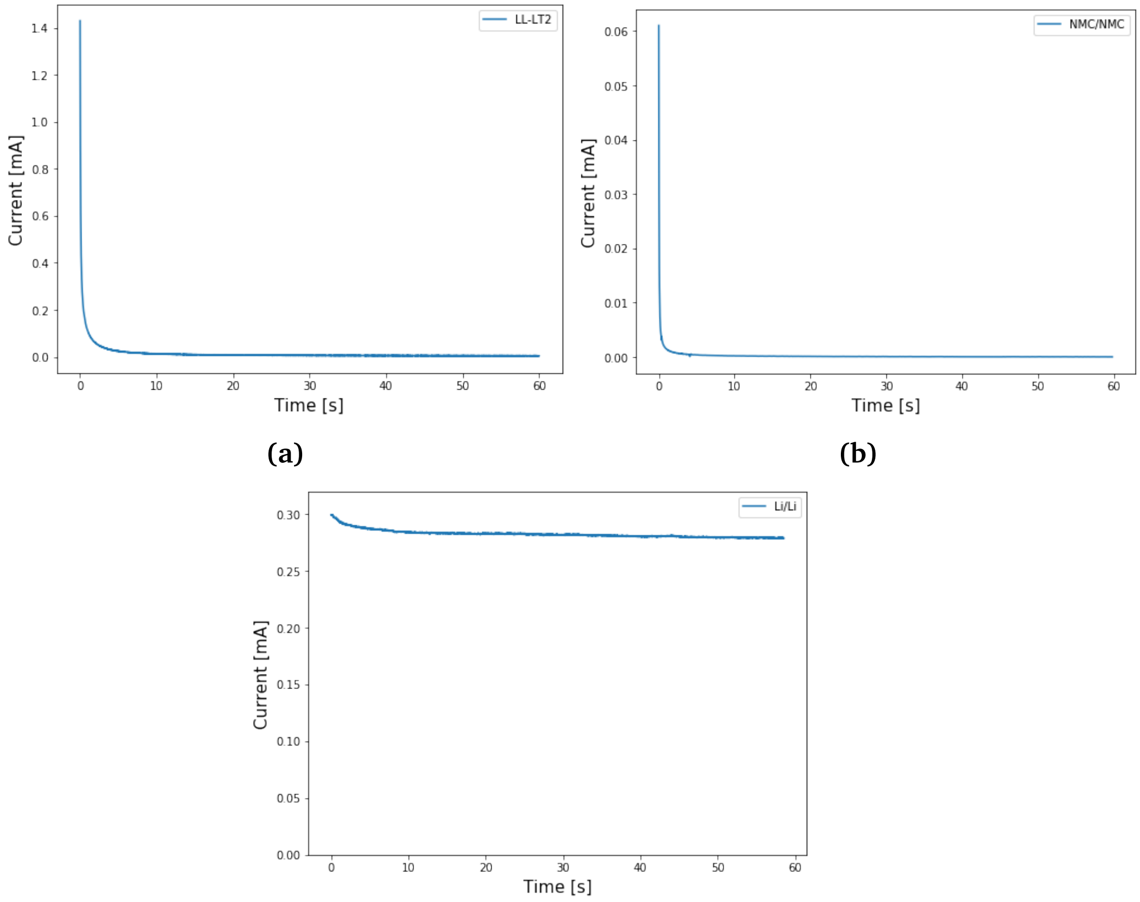

(a) **(b)**

(c)

Figure 4.24: Current vs. time graphs from potential step chronoamperometry measurements. Shows the current response of a) NMC/Li-metal coin cell (LL-LT1), b) NMC/NMC coin cell and c) Li-metal/Li-metal coin cell.

that the structured cathodes generally have higher time constants, independent of thickness. Since the time constant has increased for the structured cathodes, it seems that the technique is not able to detect the enhancement in performance observed for the structured cathodes, discussed in subsection 4.3.3.

By using the effective diffusion coefficient found from the model and calculating the diffusion lengths for the cathodes, it is found that the diffusion measured likely takes place within the diffusion layer at the surface of the NMC particles. The effective diffusion coefficients found for Un-MT, Perf-MT, SL-MT, LL-MT and SP-MT by fitting of the PSCA data to the diffusion model are listed in Table 4.10. The experimental time constants found for the cells are also listed in 4.10 with the diffusion length, which was found using Equation 2.11. The diffusion coefficients range from 1.34 to $3.73{\cdot}10^{-9}$ m^2/s, which is similar to the values of $LiPF_6$ and its ions, listed in Table 2.2, which are in the range of 1.48 to $3.84{\cdot}10^{-10}$ m^2/s. Indicating that the measurement is a result of diffusion in the electrolyte, as the solid state diffusion coefficient is $4{\cdot}10^{-15}$ m^2/s. The diffusion length is calculated to be between 10.1 and 33.9 μm, which is one tenth

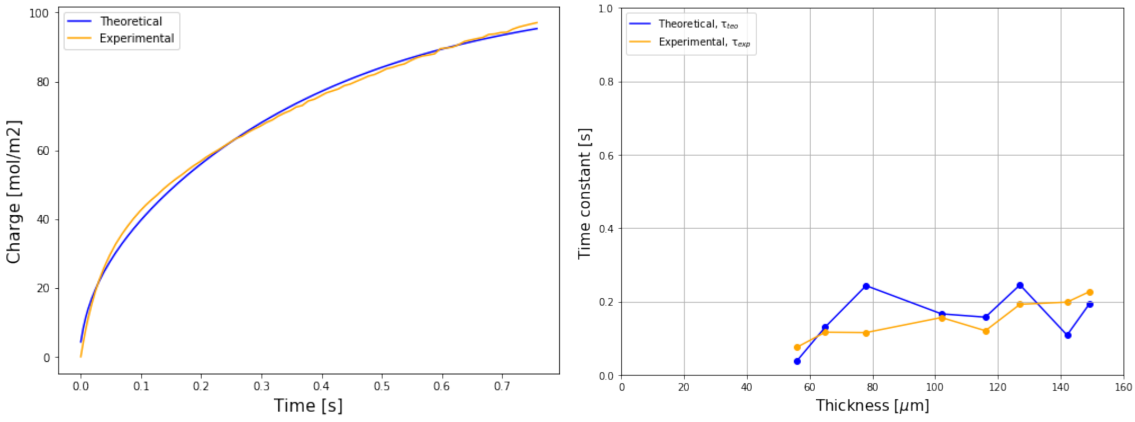

(a) **(b)**

Figure 4.25: a) Shows the theoretical and experimental charge vs. time curve resulting from the diffusion model of and a PSCA measurement of an unstructured cathode. b) Shows a time constant vs. thickness plot of unstructured cathodes.

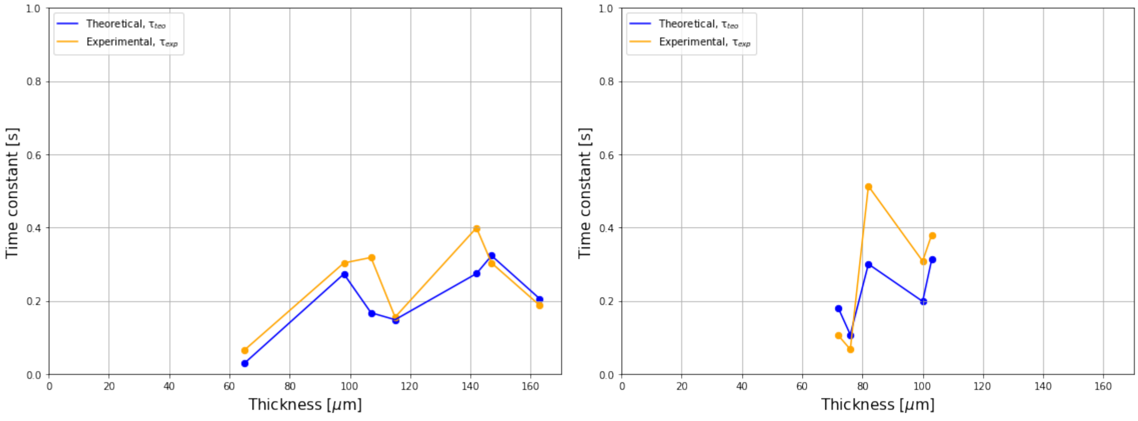

(a) **(b)**

Figure 4.26: Shows the experimental and theoretical time constants of blade Perf, SL, LL and SP structured cathodes with corresponding thicknesses, divided into two categories based on porosity. a) Over 45 % and b) Below 45 % porosity.

to one third of the thickness of the electrode, hence the diffusion through the cathode does not appear to be measured. The diffusion layer thickness of spherical particles with radius of above 1 μm can be found to be in the range of 10 to 30 μm, with a diffusion coefficient of $\approx 10^{-9}$ m^2/s[53]. Thus, PSCA can be used to measure the diffusion of particles through the diffusion layer of the NMC particles. The structuring of the cathodes does not change the diffusion layer of the particles, as it only introduces macro-pores and does not change the particle morphology. Therefore, it is not able to quantify a change in ionic transport as a result of introducing structures to the cathode structure.

Table 4.10: The experimentally determined time constant (τ_{exp}), modelled effective diffusion coefficient (D_{eff}) and calculated diffusion length (l) of cathodes with medium thickness.

Cathode	τ_{exp} [s]	D_{eff} [10^{-9}m^2/s]	l [μm]
Un-MT	0.115	1.62	13.6
Perf-MT	0.076	1.34	10.1
SL-MT	0.308	3.73	33.9
LL-MT	0.380	1.50	23.9
SP-MT	0.303	2.08	25.1

4.4 Comparison between cathodes with polyvinylidene fluoride and lignin binder

To interpret the overall quality of the cathodes with lignin binder that have been manufactured with water as solvent, their performance needs to be compared to cathodes of similar thickness with polyvinylidene fluoride (PVDF). The blade perforated lignin cathodes were found to be the best performing and will be compared to PVDF cathodes with line structures with 490 μm spacing and 18.5 μm indentation width, called very large lines (VLL). These cathodes have titanium (Ti) as current collector and were only rate-tested up to 2.5 C, instead of 5 C, as the lignin cathodes were, but their rate performance can still be compared up to this current. Three thickness ranges will be compared, low, medium and high thickness, and the PVDF cathodes used are listed in Table 4.11.

Table 4.11: Overview of the cathodes with PVDF, with the number of cathodes in each group and the range in thickness, porosity and initial specific capacity.

Structure	Name	#	Thickness [μm]	Porosity [%]	Initial speCap [mAh/g]
VLL	VLL-LT	3	48-61	38.7-54.81	137.8-147.1
	VLL-MT	3	90-100	37.2-68.3	144.8-146.8
	VLL-HT	3	140-151	35.0-42.2	150.8-160.8

The low thickness cathodes with PVDF and lignin binder perform comparably, as can be seen in Figure 4.27. At low currents (0.1-0.2 C) the cathodes are very similar, but as the C-rate increases, the specific capacity of Perf-LT decreases faster than that of VLL-LT. The largest difference is found at 2.5 C, where Perf-LT has a capacity of about 80 mAh/g and VLL-LT has a capacity of close to 120 mAh/g. The discrepancy can partially be explained by VLL-LT having a 10 % higher porosity and slightly lower thickness, which gives it a better rate performance. The efficiency of Perf-LT is generally lower than that of VLL-LT, while the deviation is only of ≈3 %, it could show that more energy is lost to irreversible processes and general degradation in the lignin cathode, compared to the ones with PVDF.

Medium thickness cathodes, Perf-MT and VLL-MT, show significant deviations in rate capability, with values of ≈ 40 mAh/g and ≈ 110 mAh/g at 2.5 C, respectively. The rate performance plots shown in Figure 4.28 displays that the rate capability of VLL-MT is much better from currents as low as 0.5 C, compared to Perf-MT. The lignin cathodes have a substantial drop in capacity from 1 to 2 C, from 115 to 60 mAh/g, which is not seen for the ones with PVDF. As for the low thickness cathodes, there is a slight deviation in coulombic efficiency, where VLL-MT has close to 100 % at every C-rate and Perf-MT has an average of about 96 % above 0.5 C. The deviation is not large, but could be a part of the reason that the PVDF cathodes perform better than the lignin cathodes. It could indicate that there is larger degree of degradation during testing for cathodes with lignin binder, which impairs their performance.

For the highest thickness cathodes, the rate capability of lignin and PVDF are much more similar, with Perf-HT and VLL-HT both having a capacity of 20 mAh/g at 2.5 C, as

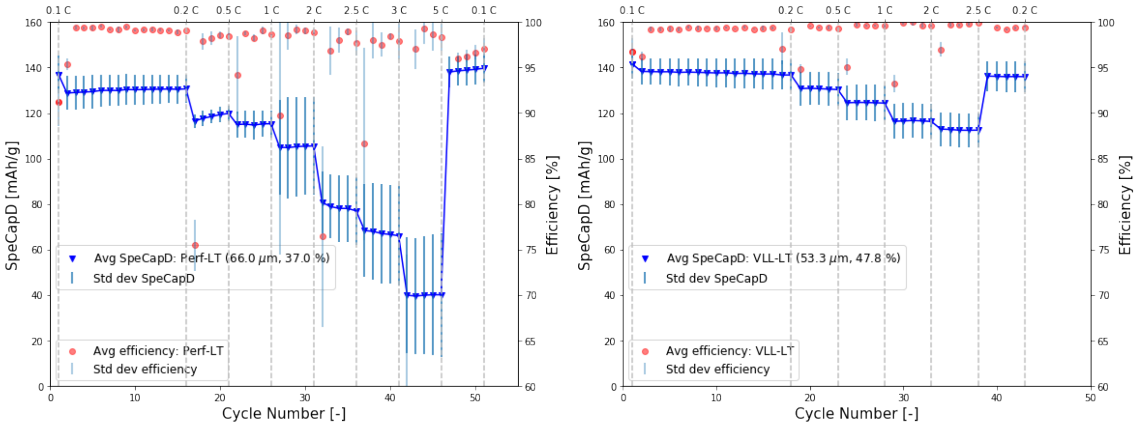

(a) **(b)**

Figure 4.27: Average rate performance plots of low thickness line structured cathodes with a) lignin (Perf-LT) and b) PVDF binder (VLL-LT).

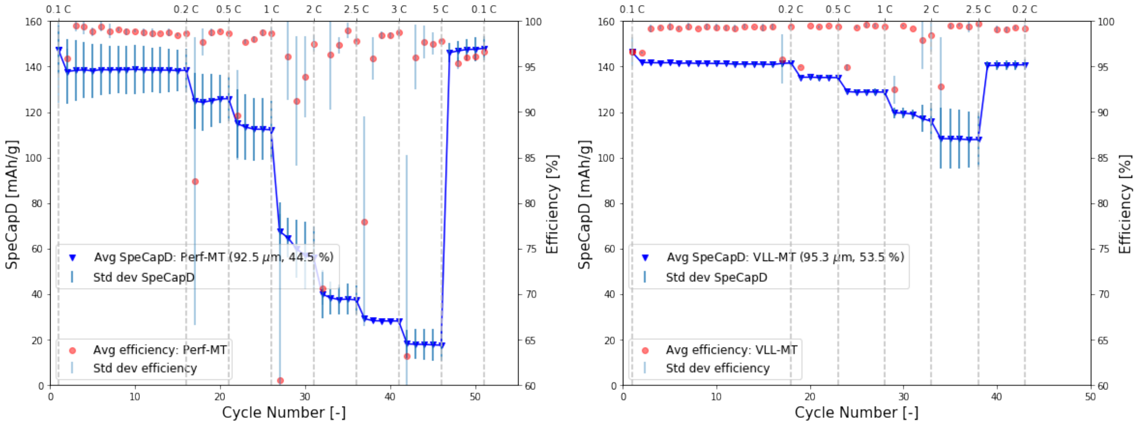

(a) **(b)**

Figure 4.28: Average rate performance plots of medium thickness line structured cathodes with a) lignin (Perf-MT) and b) PVDF (VLL-MT) binder.

seen in Figure 4.29. At thicknesses close to 150 μm, the effect of having smaller spacing between the structures could be the reason for the lignin cathodes performing equally to the PVDF at the highest currents. From 0.5 to 2 C, VLL-HT has much higher average capacity than Perf-HT and the lignin based cathode has large standard deviations. This comes as a result of the rate performance of the cathodes that are taken the average of, deviate significantly. As a result it is difficult to conclude with which binder is the best for high thickness cathodes, but they seem to perform similarly. It does however seem like both types of cathodes have a form of degradation at this thickness, since neither fully recover after rate-testing. Perf-HT experiences twice as high C-rates as VLL-HT, but has a higher capacity, which could be due to VLL-HT having 20 % lower porosity, but could indicate some instability in the PVDF cathode.

To summarize the comparison of cathodes with lignin and PVDF binder, the cathodes with PVDF have better or equal rate performance for all thicknesses. The reasons

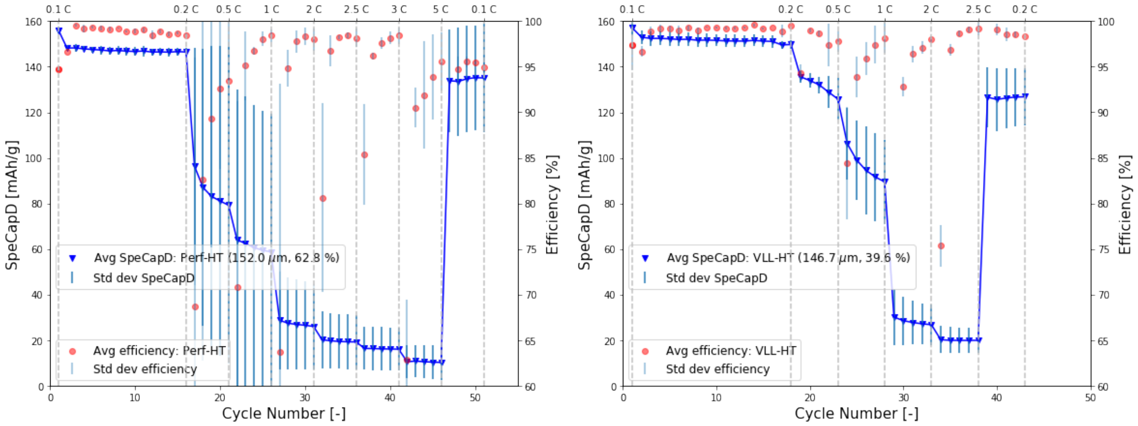

(a) **(b)**

Figure 4.29: Average rate performance plots of high thickness line structured cathodes with a) lignin (Perf-HT) and b) PVDF binder (VLL-HT).

for the PVDF cathodes performing better than the lignin ones would need further investigation to be able to conclude with any certainty, but there are some probable causes. The different current collectors (CC) used (Ti and carbon coated Al) could have an influence on the bonding strength of the cathode material to the CC, where a stronger bond causes less degradation as the cathode is more structurally stable. In addition, the higher strength of the Ti CC used for PVDF could make it more resistant to being damaged by the structuring process, whereas the Al foil could be harmed by the ceramic blades, decreasing the adhesion between cathode material and CC. PVDF is the state-of-the-art binder used in commercial cells and has excellent properties for use in NMC cathodes, like wetting and bonding strength, which could be the decisive factor to why the cathodes perform better, even though lignin is a promising and more sustainable option[3, 4].

Chapter 5

Conclusion

Lignin was tested as a binder in cathodes with NMC111 as active material to examine its influence on the performance of the cathode in a LiB. Cathodes with thicknesses over 200 μm were manufactured with an aqueous based process. Cathodes with low thickness showed adequate rate capability ($\approx$ 60 % at 5 C), which decreased quickly with increasing thickness. Only cathodes over 200 μm had 0 % rate capability at 5 C and showed degradation during cycling. EIS revealed a strong correlation between thickness and impedance, where the ohmic and SEI layer resistances were found to increase 4 and 26 times, respectively, with a 100 μm increase in thickness.

Mechanical structuring of the lignin based cathodes was performed to improve the rate capability through improving wetting and ionic transport. Two structuring tools were tested with three line structures (Perf, SL and LL) of varying indentation width, depth and spacing, and two hole structures (SP and LP), with equal spacing and different indentation width. The structures were investigated using SEM in pristine condition and post mortem, where some degradation was observed, but the structures were mainly intact. All structures, except LP (large pillars), were shown to improve the rate capability and wetting of cathodes with thicknesses close to 100 μm. EIS found that both ohmic and SEI layer resistance were lower for the structured cathodes, and that the charge transfer resistance was unchanged. The Perf line structure resulted in the best performing cathodes with a capacity of over 40 mAh/g at 2.5 C, 20 mAh/g at 5 C and the lowest measured resistances of a cathode with $\approx$ 100 μm thickness. This structure had the deepest and smallest indentation, with the second largest spacing (48 ±8 % of total thickness, 34.3 ±11.3 μm and 187.4 ±2.5 μm, respectively), resulting in the best compromise between compression of cathode material and improved ionic transport.

To further investigate the performance of cathodes with lignin binder, the Perf line structure was compared with PVDF cathodes structured with a line structure with twice as large spacing. The cathodes with PVDF were found to perform equally or better than the lignin cathodes at thicknesses from 50 to 150 μm. The most similar performance was found for the cathodes with $\approx$ 150 μm thickness, where both lignin and PVDF cathodes had a specific capacity of $\approx$ 20 mAh/g at 2.5 C. Therefore, it appears that the PVDF binder results in cathodes with better rate performance at lower thicknesses than lignin, independent of structuring. At high thicknesses, however, appropriate structuring can make up for differences due to binder. Therefore, it was concluded that lignin based cathodes are promising for the use in LiBs, with the use of pore engineering in the form of structuring.

A model for diffusion of ions between plane sheets was paired with PSCA to investigate the effect the structures had on diffusion in cathodes. Experimental data from potential step measurements were used to find the effective diffusion coefficient and a theoretical time constant of the system by using the Levenberg-Marquardt method. The model predicted theoretical time constants close in value to experimental time constants, and was confirmed to model diffusion within the cathode. The effective diffusion coefficients of unstructured and structured cathodes were found to generally be of similar value, which contradicted the results found during galvanostatic cycling. By calculating the diffusion length of the ions and comparing the values found for the effective diffusion coefficients with tabulated values, it was found that PSCA measures transport of ions within the diffuse layer at the NMC particle surface. Thus, it was concluded that PSCA can not be used to investigate a change in diffusion paths for a porous electrode.

Chapter 6

Further Work

Imperfect structuring of a cathode could to a large extent impair its properties and result in a worse performing cathode than an unstructured one. To be able to fully investigate the potential of the structures used in this report, the structuring should be automated to remove the human element. Identical pressure, timing and placement of the structuring tool from batch-to-batch would remove all variations that have been a consequence of structure quality. This would make it possible to investigate the full effect of a structuring technique.

The mechanical and chemical stability of the structured cathodes should be investigated further, by using longer cycling programs. Even though the structures have been able to endure crimping and rate-testing, the indentations could grow over time, resulting in dislodged active material, filled indentations, increased impedance and capacity fade. If structured cathodes are to be implemented in a large scale, the degradation mechanisms that occur both during high C-rate cycling and longer use, needs to be investigated.

Ionic transport is to a large extent determined by the porosity for an unstructured cathode, but its influence on structured cathodes should be investigated. Determining how the porosity influences the effect of the structures would give valuable information regarding the optimal structuring parameters needed to acquire the needed cathode properties for a given application.

Further work should also aim to find a technique to quantify the effect structuring has on the ionic transport and the diffusion paths in the cathode, e.g. by measuring the change in ionic conductivity due to structuring. By directly analyzing the effect each structure has on diffusion, at a given thickness and porosity, the properties of the cathode could be engineered to any application. It would also be able to determine if subtractive and non-subtractive structuring techniques result in the same improved ionic transport, or if material needs to be removed to observe a significant improvement.

Bibliography

[1] M. V. Reddy, A. Mauger, C. M. Julien, A. Paolella and K. Zaghib, 'Brief history of early lithium-battery development,' *Materials*, vol. 13, no. 8, 2020. DOI: 10.3390/ma13081884.

[2] J. B. Dunn, L. Gaines, J. C. Kelly, C. James and K. G. Gallagher, 'The significance of li-ion batteries in electric vehicle life-cycle energy and emissions and recyclings role in its reduction,' *Energy Environmental Science*, vol. 8, no. 1, pp. 158–168, 2015. DOI: 10.1039/c4ee03029j.

[3] H. Lu, A. Cornell, F. Alvarado, M. Behm, S. Leijonmarck, J. Li, P. Tomani and G. Lindbergh, 'Lignin as a binder material for eco-friendly li-ion batteries,' *Materials*, vol. 9, no. 3, 2016. DOI: 10.3390/ma9030127.

[4] P. Zhu, J. Han and W. Pfleging, 'Characterization and laser structuring of aqueous processed li(ni0.6mn0.2co0.2)o2 thick-film cathodes for lithium-ion batteries,' *Nanomaterials*, vol. 11, no. 7, 2021. DOI: 10.3390/nano11071840.

[5] J. Habedank, M. Zäh and A. Kwade, *Laser Structuring of Graphite Anodes for Functionally Enhanced Lithium-Ion Batteries*. Universitätsbibliothek der TU München, 2021.

[6] P. Zhu, D. Gastol, J. Marshall, R. Sommerville, V. Goodship and E. Kendrick, 'A review of current collectors for lithium-ion batteries,' *Journal of Power Sources*, vol. 485, p. 229 321, 2021. DOI: 10.1016/j.jpowsour.2020.229321.

[7] N. Nitta, F. Wu, J. T. Lee and G. Yushin, 'Li-ion battery materials: Present and future,' *Materials Today*, vol. 18, no. 5, pp. 252–264, 2015. DOI: 10.1016/j.mattod.2014.10.040.

[8] O. S. Burheim, *Engineering Energy Storage*. London: Elsevier, 2017, pp. 112–113.

[9] H. Zhang, C. Li, G. G. Eshetu, S. Laruelle, S. Grugeon, K. Zaghib, C. Julien, A. Mauger, D. Guyomard, T. Rojo, N. Gisbert-Trejo, S. Passerini, X. Huang, Z. Zhou, P. Johansson and M. Forsyth, 'From solid-solution electrodes and the rocking-chair concept to today's batteries,' *Angewandte Chemie International Edition*, vol. 59, no. 2, pp. 534–538, 2020. DOI: 10.1002/anie.201913923.

[10] A. Manthiram, 'A reflection on lithium-ion battery cathode chemistry,' *Nature Communications*, vol. 11, no. 1, 2020. DOI: 10.1038/s41467-020-15355-0.

[11] J. Vetter, P. Novák, M. Wagner, C. Veit, K.-C. Möller, J. Besenhard, M. Winter, M. Wohlfahrt-Mehrens, C. Vogler and A. Hammouche, 'Ageing mechanisms in lithium-ion batteries,' *Journal of Power Sources*, vol. 147, no. 1, pp. 269–281, 2005. DOI: `10.1016/j.jpowsour.2005.01.006`.

[12] C. Julien, A. Mauger, A. K. Vijh and K. Zaghib, *Lithium batteries: science and technology*. Springer International Publishing Schwitzerland, 2016.

[13] M. Park, X. Zhang, M. Chung, G. B. Less and A. M. Sastry, 'A review of conduction phenomena in li-ion batteries,' *Journal of Power Sources*, vol. 195, no. 24, pp. 7904–7929, 2010. DOI: `10.1016/j.jpowsour.2010.06.060`.

[14] P. Shafiei Sabet, A. J. Warnecke, F. Meier, H. Witzenhausen, E. Martinez-Laserna and D. U. Sauer, 'Non-invasive yet separate investigation of anode/cathode degradation of lithium-ion batteries (nickel–cobalt–manganese vs. graphite) due to accelerated aging,' *Journal of Power Sources*, vol. 449, p. 227 369, 2020. DOI: `10.1016/j.jpowsour.2019.227369`.

[15] J. A. Gilbert, I. A. Shkrob and D. P. Abraham, 'Transition metal dissolution, ion migration, electrocatalytic reduction and capacity loss in lithium-ion full cells,' *Journal of The Electrochemical Society*, vol. 164, no. 2, A389–A399, 2017. DOI: `10.1149/2.1111702jes`.

[16] K. Amine, Z. Chen, Z. Zhang, J. Liu, W. Lu, Y. Qin, J. Lu, L. Curtis and Y.-K. Sun, 'Mechanism of capacity fade of mcmb/li1.1[ni1/3mn1/3co1/3]0.9o2 cell at elevated temperature and additives to improve its cycle life,' *Journal of Materials Chemistry*, vol. 21, no. 44, p. 17 754, 2011. DOI: `10.1039/c1jm11584g`.

[17] J. Park, H. Song, I. Jang, J. Lee, J. Um, S.-g. Bae, J. Kim, S. Jeong and H.-J. Kim, 'Three-dimensionalization via control of laser-structuring parameters for high energy and high power lithium-ion battery under various operating conditions,' *Journal of Energy Chemistry*, vol. 64, pp. 93–102, 2022. DOI: `10.1016/j.jechem.2021.04.011`.

[18] M. Ebner and V. Wood, 'Tool for Tortuosity Estimation in Lithium Ion Battery Porous Electrodes,' en, *Journal of The Electrochemical Society*, vol. 162, no. 2, A3064, Dec. 2014. DOI: `10.1149/2.0111502jes`.

[19] J. Park, H. Song, I. Jang, J. Lee, J. Um, S.-G. Bae, J. Kim, S. Jeong and H.-J. Kim, 'Three-dimensionalization via control of laser-structuring parameters for high energy and high power lithium-ion battery under various operating conditions,' *Journal of Energy Chemistry*, vol. 64, pp. 93–102, 2022. DOI: `10.1016/j.jechem.2021.04.011`.

[20] V. P. Nemani, S. J. Harris and K. C. Smith, 'Design of bi-tortuous, anisotropic graphite anodes for fast ion-transport in li-ion batteries,' *Journal of The Electrochemical Society*, vol. 162, no. 8, 2015. DOI: `10.1149/2.0151508jes`.

[21] W. B. Hawley and J. Li, 'Electrode manufacturing for lithium-ion batteries—analysis of current and next generation processing,' *Journal of Energy Storage*, vol. 25, p. 100 862, 2019. DOI: `10.1016/j.est.2019.100862`.

[22] J. Li, J. Fleetwood, W. B. Hawley and W. Kays, 'From materials to cell: State-of-the-art and prospective technologies for lithium-ion battery electrode processing,' *Chemical Reviews*, vol. 122, no. 1, pp. 903–956, 2022, PMID: 34705441. DOI: `10.1021/acs.chemrev.1c00565`.

[23] S. N. Bryntesen, A. H. Strømman, I. Tolstorebrov, P. R. Shearing, J. J. Lamb and O. Stokke Burheim, 'Opportunities for the state-of-the-art production of lib electrodes—a review,' *Energies*, vol. 14, no. 5, 2021. DOI: `10.3390/en14051406`.

[24] T. C. Nirmale, B. B. Kale and A. J. Varma, 'A review on cellulose and lignin based binders and electrodes: Small steps towards a sustainable lithium ion battery,' *International Journal of Biological Macromolecules*, vol. 103, pp. 1032–1043, 2017. DOI: `10.1016/j.ijbiomac.2017.05.155`.

[25] V. Ponnuchamy and E. S. Esakkimuthu, 'Density functional theory study of lignin, carboxymethylcellulose and unsustainable binders with graphene for electrodes in lithium-ion batteries,' *Applied Surface Science*, vol. 573, p. 151 461, 2022. DOI: `10.1016/j.apsusc.2021.151461`.

[26] C.-J. Bae, C. K. Erdonmez, J. W. Halloran and Y.-M. Chiang, 'Design of battery electrodes with dual-scale porosity to minimize tortuosity and maximize performance,' *Advanced Materials*, vol. 25, no. 9, pp. 1254–1258, 2013. DOI: `10.1002/adma.201204055`.

[27] B.-S. Lee, Z. Wu, V. Petrova, X. Xing, H.-D. Lim, H. Liu and P. Liu, 'Analysis of rate-limiting factors in thick electrodes for electric vehicle applications,' *Journal of The Electrochemical Society*, vol. 165, no. 3, A525–A533, 2018. DOI: `10.1149/2.0571803jes`.

[28] W. Pfleging, 'A review of laser electrode processing for development and manufacturing of lithium-ion batteries,' *Nanophotonics*, vol. 7, no. 3, pp. 549–573, 2018. DOI: `10.1515/nanoph-2017-0044`.

[29] *Electron microscopy: Scanning electron microscopy: Thermo fisher scientific - us*. [Online]. Available: `https://www.thermofisher.com/no/en/home/materials-science/learning-center/applications/sem-electrons.html` (visited on 12/02/2022).

[30] J. Hjelen, *Scanning elektron-mikroskopi*. SINTEF, 1989.

[31] E. Talaie, P. Bonnick, X. Sun, Q. Pang, X. Liang and L. F. Nazar, 'Methods and protocols for electrochemical energy storage materials research,' *Chemistry of Materials*, vol. 29, no. 1, pp. 90–105, 2017. DOI: `10.1021/acs.chemmater.6b02726`.

[32] 'Combinatorial performance mapping of near-nmc111 li-ion cathodes,' *Journal of Materiomics*, vol. 8, no. 2, pp. 437–445, 2022. DOI: `10.1016/j.jmat.2021.07.003`.

[33] R. Ferrero, C. Wu, A. Carboni, S. Toscani, M. De Angelis, H. George-Williams, E. Patelli and P. A. Pegoraro, 'Low-cost battery monitoring by converter-based electrochemical impedance spectroscopy,' in *2017 IEEE International Workshop on Applied Measurements for Power Systems (AMPS)*, 2017, pp. 1–6. DOI: `10.1109/AMPS.2017.8078334`.

[34] G. Brug, A. van den Eeden, M. Sluyters-Rehbach and J. Sluyters, 'The analysis of electrode impedances complicated by the presence of a constant phase element,' *Journal of Electroanalytical Chemistry and Interfacial Electrochemistry*, vol. 176, no. 1, pp. 275–295, 1984. DOI: `10.1016/S0022-0728(84)80324-1`.

[35] V. J. Ovejas and A. Cuadras, 'Impedance characterization of an lco-nmc/graphite cell: Ohmic conduction, sei transport and charge-transfer phenomenon,' *Batteries*, vol. 4, no. 3, 2018. DOI: `10.3390/batteries4030043`.

[36] J. Li, X. Xiao, F. Yang, M. W. Verbrugge and Y.-T. Cheng, 'Potentiostatic intermittent titration technique for electrodes governed by diffusion and interfacial reaction,' *The Journal of Physical Chemistry C*, vol. 116, no. 1, pp. 1472–1478, 2012. DOI: `10.1021/jp207919q`.

[37] *Determination of the diffusion coefficient of an inserted species in a host electrode with eis, pitt and gitt techniques*, Jun. 2021. [Online]. Available: `https://biologic.net/wp-content/uploads/2021/06/an70_eis_gitt_pitt_4.pdf` (visited on 21/04/2022).

[38] J. Crank and E. Crank, *The Mathematics of Diffusion*, ser. Oxford science publications. Clarendon Press, 1979, pp. 47–53, ISBN: 9780198534112.

[39] P. Porion, Y. R. Dougassa, C. Tessier, L. El Ouatani, J. Jacquemin and M. Anouti, 'Comparative study on transport properties for lifap and lipf6 in alkyl-carbonates as electrolytes through conductivity, viscosity and nmr self-diffusion measurements,' *Electrochimica Acta*, vol. 114, pp. 95–104, 2013. DOI: `10.1016/j.electacta.2013.10.015`.

[40] S. G. Stewart and J. Newman, 'The use of UV/vis absorption to measure diffusion coefficients in LiPF[sub 6] electrolytic solutions,' *Journal of The Electrochemical Society*, vol. 155, no. 1, F13, 2008. DOI: `10.1149/1.2801378`.

[41] S. E. J. O'Kane, W. Ai, G. Madabattula, D. Alonso-Alvarez, R. Timms, V. Sulzer, J. S. Edge, B. Wu, G. J. Offer and M. Marinescu, 'Lithium-ion battery degradation: How to model it,' *Phys. Chem. Chem. Phys.*, vol. 24, pp. 7909–7922, 13 2022. DOI: `10.1039/D2CP00417H`.

[42] W. Kao-ian, R. Pornprasertsuk, P. Thamyongkit, T. Maiyalagan and S. Kheawhom, 'Rechargeable zinc-ion battery based on choline chloride-urea deep eutectic solvent,' *Journal of The Electrochemical Society*, vol. 166, no. 6, A1063–A1069, 2019. DOI: `10.1149/2.0641906jes`.

[43] L. Azhari, X. Zhou, B. Sousa, Z. Yang, G. Gao and Y. Wang, 'Effects of extended aqueous processing on structure, chemistry, and performance of polycrystalline linixmnycozo2 cathode powders,' *ACS Applied Materials & Interfaces*, vol. 12, no. 52, pp. 57 963–57 974, 2020, PMID: 33332088. DOI: `10.1021/acsami.0c20105`.

[44] M. Bichon, D. Sotta, N. Dupré, E. De Vito, A. Boulineau, W. Porcher and B. Lestriez, 'Study of immersion of lini0.5mn0.3co0.2o2 material in water for aqueous processing of positive electrode for li-ion batteries,' *ACS Applied Materials & Interfaces*, vol. 11, no. 20, pp. 18 331–18 341, 2019. DOI: `10.1021/acsami.9b00999`.

[45] T. Li, X.-Z. Yuan, L. Zhang, D. Song, K. Shi and C. Bock, 'Degradation mechanisms and mitigation strategies of nickel-rich nmc-based lithium-ion batteries,' *Electrochemical Energy Reviews*, vol. 3, no. 1, pp. 43–80, 2019. DOI: `10.1007/s41918-019-00053-3`.

[46] J. S. Edge, S. O'Kane, R. Prosser, N. D. Kirkaldy, A. N. Patel, A. Hales, A. Ghosh, W. Ai, J. Chen, J. Yang, S. Li, M.-C. Pang, L. Bravo Diaz, A. Tomaszewska, M. W. Marzook, K. N. Radhakrishnan, H. Wang, Y. Patel, B. Wu and G. J. Offer, 'Lithium ion battery degradation: What you need to know,' *Phys. Chem. Chem. Phys.*, vol. 23, pp. 8200–8221, 14 2021. DOI: `10.1039/D1CP00359C`.

[47] J. Huang, Z. Li, J. Zhang, S. Song, Z. Lou and N. Wu, 'An analytical three-scale impedance model for porous electrode with agglomerates in lithium-ion batteries,' *Journal of The Electrochemical Society*, vol. 162, no. 4, A585–A595, 2015. DOI: `10.1149/2.0241504jes`.

[48] P. Shafiei Sabet and D. U. Sauer, 'Separation of predominant processes in electrochemical impedance spectra of lithium-ion batteries with nickel-manganese-cobalt cathodes,' *Journal of Power Sources*, vol. 425, pp. 121–129, 2019. DOI: `10.1016/j.jpowsour.2019.03.068`.

[49] M. D. Levi, G. Salitra, B. Markovsky, H. Teller, D. Aurbach, U. Heider and L. Heider, 'Solid-state electrochemical kinetics of li-ion intercalation into li1x coo2: Simultaneous application of electroanalytical techniques sscv, pitt, and eis,' *Journal of The Electrochemical Society*, vol. 146, no. 4, pp. 1279–1289, 1999. DOI: `10.1149/1.1391759`.

[50] H. Kang, C. Lim, T. Li, Y. Fu, B. Yan, N. Houston, V. De Andrade, F. De Carlo and L. Zhu, 'Geometric and electrochemical characteristics of lini1/3mn1/3co1/3o2 electrode with different calendering conditions,' *Electrochimica Acta*, vol. 232, pp. 431–438, 2017. DOI: `10.1016/j.electacta.2017.02.151`.

[51] K. Sahni, M. Ashuri, Q. He, R. Sahore, I. D. Bloom, Y. Liu, J. A. Kaduk and L. L. Shaw, 'H3po4 treatment to enhance the electrochemical properties of li(ni1/3mn1/3co1/3)o2 and li(ni0.5mn0.3co0.2)o2 cathodes,' *Electrochimica Acta*, vol. 301, pp. 8–22, 2019. DOI: `10.1016/j.electacta.2019.01.153`.

[52] R.-C. Lee, J. Franklin, C. Tian, D. Nordlund, M. Doeff and R. Kostecki, 'The origin of impedance rise in ni-rich positive electrodes for lithium-ion batteries,' *Journal of Power Sources*, vol. 498, p. 229 885, 2021. DOI: `10.1016/j.jpowsour.2021.229885`.

[53] C. H. Hamann, A. Hamnett and W. Vielstich, in *Electrochemistry*. Wiley-VCH, 2007, pp. 187–204.

Appendix A

Appendices

A.1 SEM structuring dimensions

Figure A.1-A.4 shows SEM images of the surface and cross-section of cathodes used to find the width, depth and spacing of the different structures.

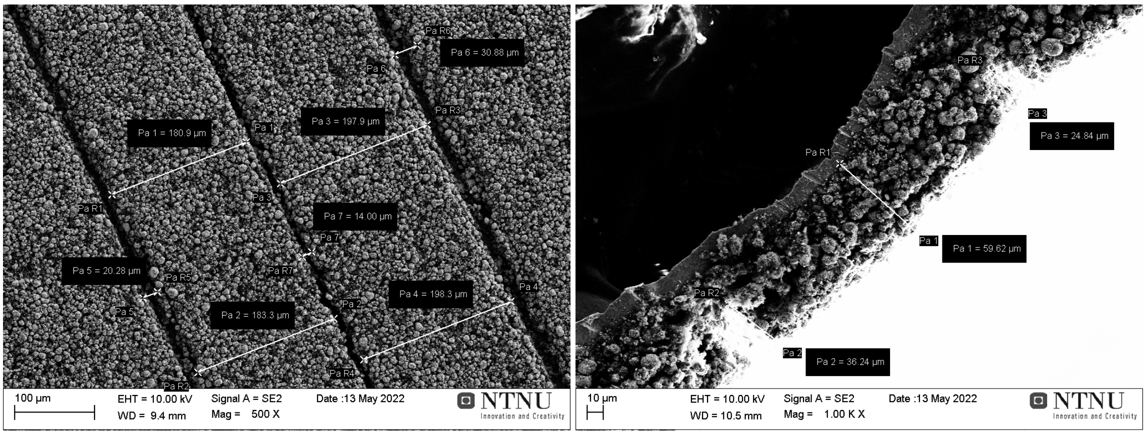

(a) **(b)**

Figure A.1: Measurements of the dimensions for two of the blade perforated (Perf) cathodes. a) Surface view and b) Cross-section.

Figure A.5a shows the cross-section of a large pillar indentation in a well structured cathode. Figure A.5b shows how damaged the cathode film could be as a result of poor structuring.

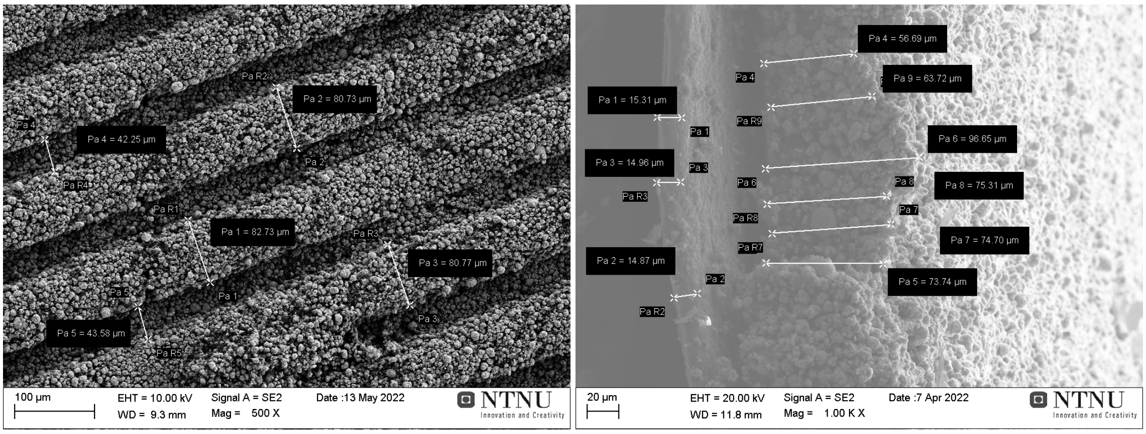

(a) **(b)**

Figure A.2: Measurements of the dimensions for two of the small line (SL) cathodes. a) Surface view and b) Cross-section.

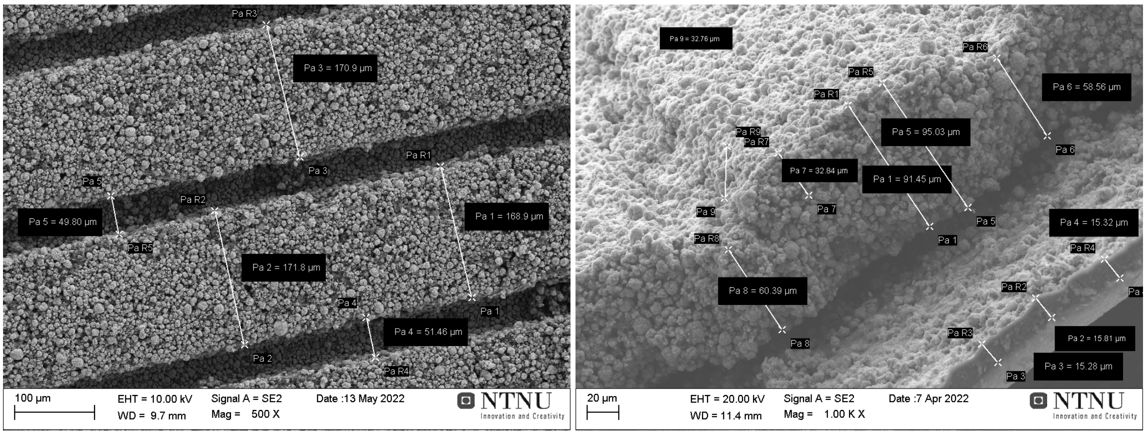

(a) **(b)**

Figure A.3: Measurements of the dimensions for two of the large line (LL) cathodes. a) Surface view and b) Cross-section.

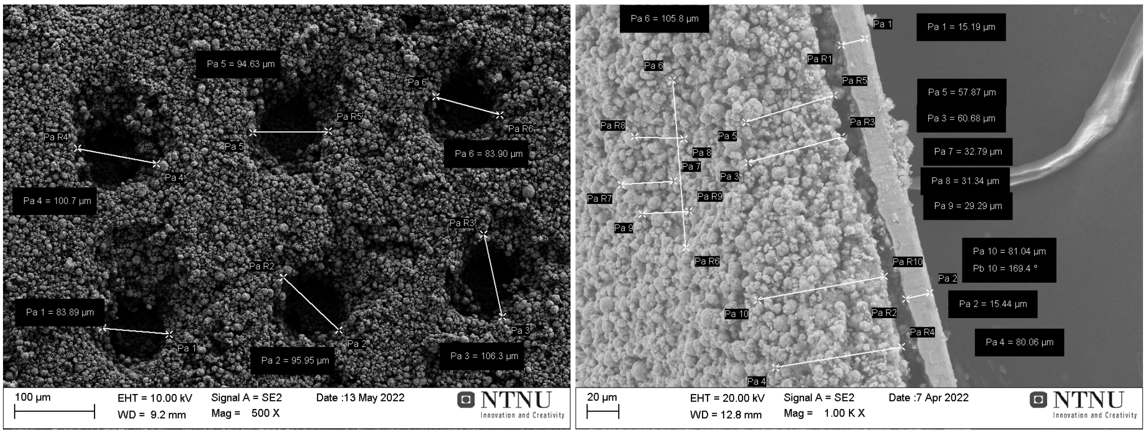

(a) **(b)**

Figure A.4: Measurements of the dimensions of two of the small pillar (SP) cathodes. a) Surface view and b) Cross-section.

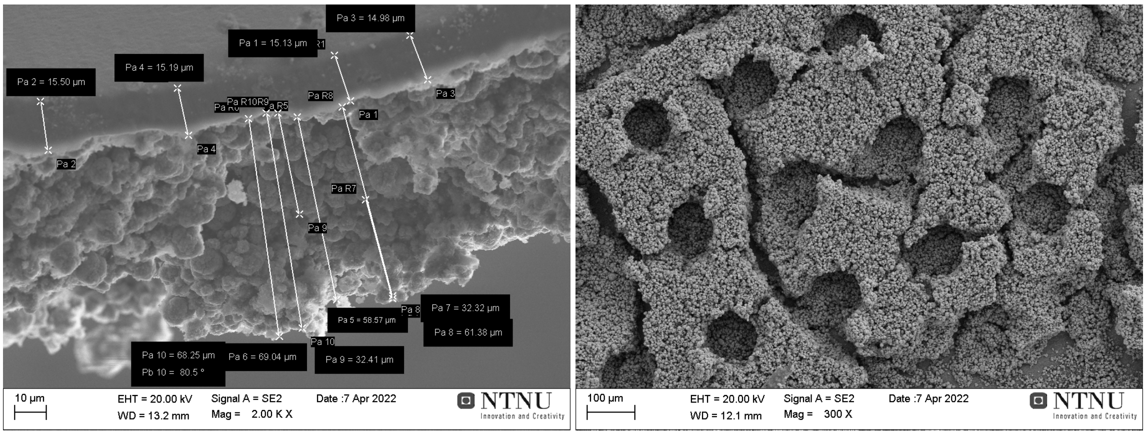

(a) **(b)**

Figure A.5: SEM images of a cathode with large pillar (LP) structures. a) Cross section with measurements of the depth of the structure. b) Example of the effect poor structuring has on the cathode film.

NTNU
Kunnskap for en bedre verden